Master of Science Thesis

On-Site Drafting Aerodynamics of Cyclists using the Ring of Fire

Nikhil Mahalingesh

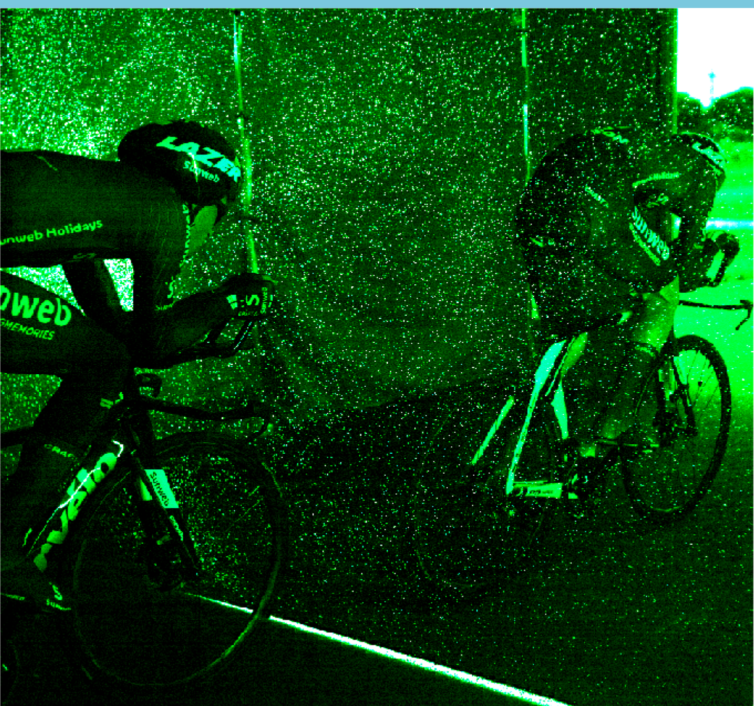

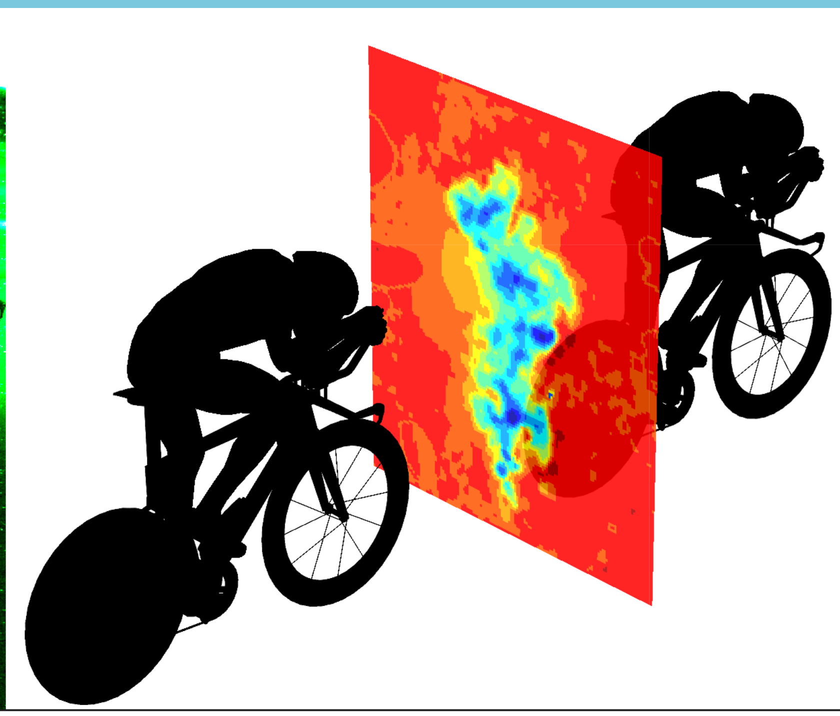

Faculty of Aerospace Engineering

Delft University of Technology

Master of Science Thesis

On-Site Drafting Aerodynamics of Cyclists using the Ring of Fire

by

Nikhil Mahalingesh

to obtain the degree of Master of Science
at the Delft University of Technology,
to be defended publicly on Friday February 28, 2020 at 13:30.

Student number:	4752015	
Project duration:	March 11, 2019 – February 28, 2020	
Thesis committee:	Dr. A. Sciacchitano,	TU Delft, supervisor
	Ir. A.M.C.M.G. Spoelstra,	TU Delft, supervisor
	Dr. ir. B.W. van Oudheusden	TU Delft, Chair
	Prof. dr. ir. W. van de Water	TU Delft, Examiner

An electronic version of this thesis is available at http://repository.tudelft.nl/.

Preface

Around three years ago, I made a choice to pursue master of science outside India. Little did I know then the implications of this choice and looking back now, what a wild journey of adventure and discovery it has been.

This thesis is the culmination of the masters program in the aerodynamics profile at the faculty of aerospace engineering, Delft university of technology. The work carried out over the past one year as part of my master thesis project is summarised here. Working on the Ring of Fire project has been a surreal experience and for that I would to thank my supervisors Dr. Andrea Sciacchitano and Ir. Alexander Spoelstra for giving me this opportunity. You have been wonderful and inspiring mentors for which I am deeply grateful. I would also like to thank Ir. Constantin Jux for his help and support during the experimental campaign and the thought-provoking discussions.

The successful execution of my experimental campaign would not be possible without the help of Dennis Bruikman and Peter Duyndam who provided their expertise on the design and assembly of the experimental setup. Additionally, Frits Donker Duyvis, Henk-Jan Siemer, Nico van Beek, Colette Russo and the rest of the staff at the High Speed Laboratory have played a significant role in the completion of the my thesis for which I would like to express my appreciation.

The past two and half years would not have been a positive experience without the support of my friends. The aerodynamics boys (Kushal, Nikhilesh, Abhinand, Athreya, Sid, Sampath, Santosh, Shubham and Kiran) who were my family away from home. My peers at the basement with whom I had interesting discussions and coffee breaks. My old friends from Bangalore (Prajwal, Noel, Niyam, Sagar, Niranjan and Pushyami) who shared this wonderful journey with me. And to all the friends I could not name personally, I am deeply thankful.

All of this would not have been possible without the unconditional love, support and encouragement of my parents and my brother. I would not have been able to pursue my ambitions and dreams without them, for which I am forever grateful and indebted.

Nikhil Mahalingesh
Delft, February 2020

Abstract

Aerodynamics plays a significant role in the field of cycling as it is the dominant resistive force at racing speeds of 50 km/h. Sporting events involving multiple cyclists leads to aerodynamic interactions between the cyclists and these interactions have been exploited for performance benefits. One such aerodynamic interaction is drafting, where cyclists closely follow each other and experience a reduction in aerodynamic drag. The benefits of drafting are profound with drag reductions as high as 49%. The aerodynamics of drafting have been studied previously using qualitative and quantitative techniques such as wind tunnel test, numerical methods and track testing. However, large discrepancies exist between various studies partly due to the fact that most investigations focus either on flow visualisation or drag measurements, and thus a complete picture is not obtained. The Ring of Fire technique is an innovative flow measurement system that provides both flow field information as well as aerodynamic drag force for full-scale on-site transiting cyclists.

The Ring of Fire technique is used in the current study to investigate the aerodynamics of on-site drafting cyclists in an outdoor environment. The effect of drafting distance and cyclist size on drag reduction are investigated using different configurations of two cyclists in drafting formation. Large-scale time-resolved stereoscopic Particle Image Velocimetry (PIV) is conducted using Helium Filled Soap Bubbles (HFSB) at cycling speeds of 13.3 m/s. Planar pressure fields are reconstructed from velocity data using the 2D pressure Poisson equation (PPE). Modifications and improvements are made to existing data reduction techniques utilised in previous Ring of Fire experiments.

Qualitative examination of ensemble averaged flow fields is performed for the full wake of an individual cyclist and the near wake of the three cyclists are compared as well. Quantitative analyses of drag area, focusing on variation with distance, sensitivity to wind and statistical uncertainty are conducted. Measurements of individual cyclists show that the size of the cyclist is a qualitative indicator of relative aerodynamic performance between cyclists, provided cycling equipment and skill are reasonably common between them. Statistical uncertainty of the individual measurements are improved from previous outdoor Ring of Fire experiments.

Flow fields from drafting obtained in-between the cyclists and behind both the cyclists, which are compared with the wake of individual cyclists and the main mechanism of drag reduction for the trailing cyclist is addressed. Quantitative analyses of drag area of the leading, trailing and the two cyclists as a group are performed, with a particular emphasis on drag reduction of the trailing cyclist and its dependence on longitudinal and lateral drafting distances. Anomalies in the drag data indicate towards a complex interaction between the leader wake, phase difference in crank angles and the wake of the trailing cyclist.

Contents

List of Figures

List of Tables

Nomenclature

Latin Letters

δz	Depth of field
$\dot{m}_i$	Mass flow rate at upstream plane
$\dot{m}_o$	Mass flow rate at downstream plane
$(C_D A)_{\text{ind}}$	Drag area of the individual cyclist
$(C_D A)_{\text{lead}}$	Drag area of the leading cyclist
$(C_D A)_{\text{peloton}}$	Drag area of the peloton
$(C_D A)_{\text{trail}}$	Drag area of the trailing cyclist
$\mathbf{F}(t)$	Instantaneous force vector
$\mathbf{F}_{\text{viscous}}$	Total viscous force
$\mathbf{n}$	Unit normal Vector
$\mathbf{V}$	Velocity vector
$\mathbf{V}_s$	Slip velocity
$\mathbf{x}$	Coordinate vector
$\mathcal{V}$	Control volume
$\mathcal{V}_{cyc}$	Volume of the cyclist
$\bar{\text{x}}$	Average lateral distance
$\bar{\text{z}}$	Average longitudinal distance
$\overline{d}$	Average overall drafting distance
$\overline{w_{\text{cyc}}}$	Average velocity of the two cyclists
$\overline{w}$	Non-dimensional streamwise velocity component
R_{lead}	Drag reduction of the leading cyclist
$\text{R}_{\text{peloton}}$	Drag reduction of the peloton
R_{trail}	Drag reduction of the trailing cyclist
A	Frontal area of the cyclist
a	Acceleration of particle
c	Scaling factor
C_D	Drag coefficient
$C_D A$	Drag area
c_p	Coefficient of pressure

D	Aerodynamic drag force
d_i	Image distance
d_o	Object distance
d_p	Particel diameter
d_τ	Effective size of particle image
d_{diff}	Diffraction diameter of particle
d_{geo}	Geometrical image diameter of particle
E_D	Drive train efficiency
Ei	Exponential integral function
f	Focal length of lens
$f_\#$	Camera f-stop
f_p	Pedalling frequency
f_{acq}	Acquisition frequency
h	Grid spacing
k	Coverage factor
k_f	Reduced pedalling frequency
L_f	Sliding sum-of-correaltion filter length
L_{ref}	Reference length
M	Optical magnification
N	Number of samples
p	Static pressure
P_A	Aerodynamic resistive power
p_∞	Upstream static pressure
p_{wake}	Downstream static pressure
P_{BR}	Bearing resistive power
P_{KE}	Power required to change kinetic energy
P_{PE}	Power required to change potential energy
P_{RR}	Rolling resistive power
P_{total}	Total resistive power
R	Residual in streamwise mass flow rate
r	Radial polar coordinate
r_c	Crank arm length
Re	Reynolds number
S_i	Upstream control surface

S_o	Downstream control surface
t	Time coordinate
U	Statistical uncertainty of the mean
u	Lateral velocity component
U_{conv}	Mean convection velocity
v	Vertical velocity component
V_r	Radial velocity component
V_{cyc}	Relative velocity of the cyclist
V_θ	Azimuthal velocity component
w	Stremwise velocity component
w_∞	Upstream streamwise velocity
w_{cyc}	Velocity of the cyclist
w_{wake}	Downstream streamwise velocity
x	Lateral coordinate
y	Vertical coordinate
z	Streamwise coordinate
dt	Sliding sum-of-correaltion image skip

Greek Letters

α	Half stereo angle
β	Vertical camera angle
Γ	Vortex circulation
Λ	Cut-off velocity
λ	Wavelength of laser light
μ	Dynamic viscosity of the fluid
ν	Kinematic viscosity
ρ	Density of air
ρ_p	Density of particle
σ	Standard deviation
σ_d	Standard deviation in overall drafting distance
$\sigma_{\Delta x}$	Uncertainty of lateral velocity component
$\sigma_{\Delta z}$	Uncertainty of streamwise velocity component
σ_{x}	Standard deviation in lateral distance
σ_{z}	Standard deviation in longitudinal distance
θ	Azimuthal polar coordinate

Abbreviations

BFS	Bubble Fluid Solution
CAD	Computer Aided Design
CFD	Computational Fluid Dynamics
CMOS	Complementary Metal-Oxide Semiconductor
CVV	Coaxial Volumetric Velocimetry
DNS	Direct Numerical Simulations
DP	Dropped Position
DSR	Dynamic Spatial Resolution
DVR	Dynamic Velocity Resolution
FSU	Fluid Supply Unit
HFSB	Helium Filled Soap Bubbles
LES	Large Eddy Simulations
LRNM	Low Reynolds Number Modelling
Nd:YAG	Neodymium-doped Yttrium Aluminium Garnet
Nd:YLF	Neodymium-doped Yttrium Lithium Fluoride
PIV	Particle Image Velocimetry
PPE	Pressure Poisson Equation
PTV	Particle Tracking Velocimetry
RANS	Reynolds Averaged Navier Stokes
RMS	Root Mean Square
TT	Time Trial Position
UP	Upright Position
L - S	Large - Small
S - L	Small - Large
L - M	Large - Medium
M - S	Medium - Small

1

Introduction

Low speed aerodynamics plays an important role in numerous applications such as commercial cars, trucks, motorcycles, etc. where significant improvements in performance and efficiency can be achieved by aerodynamic optimisation. With advancements in technology and flow measurement techniques, there has been a surge of interest on the role of fluid dynamics in competitive sports such as running, swimming, bobsleighing and speed skating. One such field which has garnered a lot of traction both from the industrial and scientific community is cycling aerodynamics. The pursuit of improving the performance of racing bicycles has seen many innovative solutions in the field of competitive cycling. The importance of aerodynamics in this field has become apparent for quite some time now. At racing speeds around 50 km/h, aerodynamic drag accounts to over 90% of the total resistance experienced by cyclists (Martin et al., 1998) and it was found that small improvements in aerodynamics translate to a huge difference in the outcome of a race. Apart from competitive sports, cycling is one of the most convenient and sustainable modes of transport and aerodynamics is fundamental to its improvement and influence. Aerodynamic investigations is thus important to understand the flow field around cyclists and improve their performance.

Since the 1990s, the amount of research and studies conducted on cycling aerodynamics has seen a huge spike. Numerous studies have been carried out involving wind tunnel experiments, numerical simulations and track testing. A large majority of these investigations have focused on performance improvements of an individual cyclist and recent studies have made a giant leap in the understanding of the flow topology of the cyclist (Crouch et al., 2014; Jux, 2017). However, more often than not, competitive cycling sports involve multiple cyclists drafting in the wake of other cyclists. The advantages of drafting was understood quite early on with studies by Kawamura (1953) and Kyle (1979) reporting drag reductions of the order of 50% for a cyclist travelling in the wake of another cyclist. The reduction in drag translates to a reduction in power required to travel at a given speed. This advantage has been exploited by novel and scientific methods in the competitive cycling community. Although the aerodynamics of drafting cyclists has been studied previously, there exists disagreements between various studies on the effect of drafting distance, cyclist size, position and posture. This is partly due to the lack of understanding of the flow topology of drafting cyclists as most investigations focus on drag measurements alone.

There is a potential to better optimise the aerodynamics and performance of drafting cyclists through detailed flow diagnostics. There seems to be disconnect in conventional methods of aerodynamic analyses between quantitative drag determination and flow-field visualisation. The Ring of Fire is a novel quantitative flow measurement technique which aims to bridge this gap through large-scale stereo-Particle Image Velocimetry (PIV) measurements of cyclists on site/track. This technique was developed by Sciacchitano et al. (2015) and provides flow field data of cyclists which is as close to reality as possible. Furthermore, the results from this technique can be used to determine aerodynamic drag by applying the conservation of momentum over the measured control volume.

The current thesis involves using the Ring of Fire technique to investigate the flow field around two cyclists in drafting formation. The aim of the thesis is to quantify and understand the aerodynamic benefits gained by the cyclists in such a formation. Such an understanding can be useful to optimise drafting configurations with respect to aerodynamic drag as well as overall performance. Four configurations of drafting cyclists were investigated namely, Large-Small, Small-Large, Large-Medium and Medium-Small, with three cyclists classified as Small, Medium and Large based on their height. The effect of cyclist size and drafting distance on the drag reduction of the cyclists are investigated.

Cycling aerodynamics is discussed in detail in Chapter 2, beginning with the first principles and ending with drafting aerodynamics. Further, a specific research gap is identified and an objective for the thesis is defined. Theoretical framework relevant to the current thesis is discussed in Chapter 3, touching on topics such as principles of stereoscopic particle image velocimetry, integral momentum analysis and pressure from PIV. The experimental methodology adopted for the thesis is addressed in Chapter 4, discussing the cyclists, on-site setup including tunnel structure, details of the PIV system and procedure of acquisition. Chapter 5 details all the different methodologies used to extract useful information from the experimental data including PIV data processing, wake contouring, conservation of mass and solving the pressure Poisson equation. Results of the experiments are divided into two parts focusing on individual and drafting cyclists respectively. Each of the two results chapter begins with a discussion on flow fields and subsequently quantitative analysis using drag. Chapter 6 starts with a general discussion on the wake of an individual cyclist and moves on to the wake comparison between the three cyclists. Individual drag area of the three cyclists are also addressed, commenting on its variations and possible sources of uncertainty. Results of the drafting cyclists are discussed in Chapter 7 with flow fields measured in-between the cyclists and in the wake of the two cyclists. Further, drag reduction for the leading, trailing and the two cyclists as a group is also addressed. The report concludes with Chapter 8 presenting the key findings and outcome of the experiments. Recommendations for future work on drafting aerodynamics as well as the Ring of Fire measurement technique are presented.

2
Cycling Aerodynamics

This chapter reviews various literature relevant to aerodynamics of cycling with a particular focus of drafting aerodynamics. The chapter begins with the importance of aerodynamics in cycling and a general discussion of bluff bodies. Subsequently, detailed studies of single cyclist aerodynamics are reviewed encompassing both drag and flow topology. This is followed by a section which details both drag and flow field interactions of drafting cyclists. Before concluding the review, the recent development and use of the "Ring of Fire" technique is discussed along with other methods of assessment. Finally, the chapter is concluded with the identification of a research gap and relevance of the current work.

Contents

2.1. Importance of Aerodynamics

To understand the importance of aerodynamics in cycling from a quantitative perspective, it is necessary to look at the mechanics and dynamics of the distribution of cycling power, i.e. if a cyclist produces 300 W of power, how much of that power is required to overcome aerodynamic resistance?

A well established and validated mathematical model for cycling power was given by Martin et al. (1998). The model provides an expression for the total resistance experienced by a cyclist in terms of fundamental and physical components i.e. aerodynamic resistance (P_A), rolling resistance (P_{RR}), bearing resistance (P_{BR}), power required to change kinetic (P_{KE}) and potential energy (P_{PE}) and drive train efficiency (E_D):

$$P_{\text{total}} = \frac{P_A + P_{RR} + P_{BR} + P_{KE} + P_{PE}}{E_D} \tag{2.1}$$

The aerodynamic resistive power can be generalised as the product of total aerodynamic drag force (D) and relative velocity of the cyclist (V_{cyc}):

$$P_A = DV_{\text{cyc}} = \left(C_D \frac{1}{2} \rho V_{\text{cyc}}^2 A\right) V_{\text{cyc}} = C_D \; \frac{1}{2} \; \rho \; V_{\text{cyc}}^3 \; A \tag{2.2}$$

Where C_D is the drag coefficient of the cyclist, ρ is the density of air and A is the frontal area of the cyclist. Depending on the velocity of the cyclist, Martin et al. (1998) reported aerodynamic resistance accounting for 56% to 96% of the total resistive power (Figure 2.1). On a flat road at racing speeds of 50 km/h, Kyle and Burke (1984) found that aerodynamic resistance was 90% of the total resistive power. Thus, it is clear that aerodynamics plays a major role in improving the performance of cyclists. A 10% improvement in aerodynamics results in a reduction of total power requirement by 16 W, while a 10% improvement in rolling resistance only reduces total power requirement by 2.3 W.

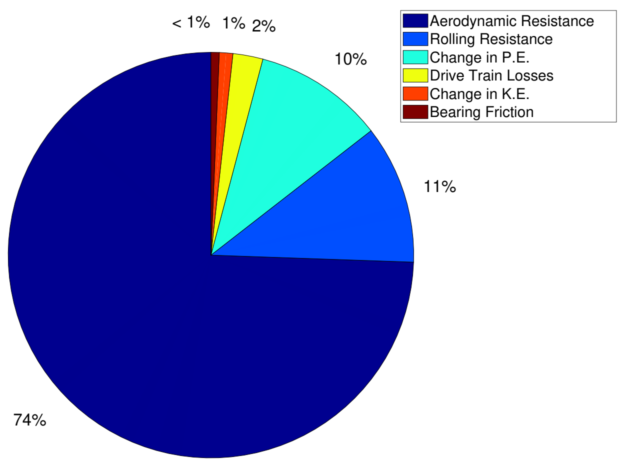

Figure 2.1: Power distribution at 30 km/h (Martin et al., 1998)

It can be observed from the above expression that the aerodynamic resistive power is directly proportional to the third power of the velocity. This means that the contribution of aerodynamics to the total resistive power becomes increasingly dominant at higher velocities. Further, Equation 2.2 shows that the aerodynamic resistive power is also proportional to the drag area of the cyclists ($C_D A$) i.e. the product of drag coefficient and frontal area. Therefore, higher gains can be achieved by reducing drag area instead of just improving drag coefficient or frontal area.

2.2. Bluff Body Aerodynamics

To improve the aerodynamics of cyclists, it is first important to understand the flow characteristics around them. Specific improvements based on the flow characteristics will provide higher gains compared to a general aerodynamic improvement. It is evident that the geometry of cyclists exhibit sharp and sudden changes in curvature (i.e. from the arms, over the shoulders and onto the back). This is in contrast to streamlined bodies such as aerofoils which have a smooth curvature and gradual reduction in width. These abrupt changes in a cyclist geometry result in adverse pressure gradients over the boundary layer causing large regions of the flow to separate. This is a characteristic of bluff body aerodynamics.

The majority of aerodynamic drag for a bluff body is due to pressure drag resulting from low pressure regions in the wake. Also, flow around bluff bodies are usually characterised by large-scale streamwise vortices in the wake, which are one of the sources of the low pressure regions (Tropea and Yarin, 2007). Further, the dynamic motion of the cyclist legs and wheels introduces additional turbulence and mixing in the cyclist wake. Thus, it is clear that the flow around cyclists is unsteady, three-dimensional and turbulent in nature.

Also, to understand the aerodynamics of cyclists, it is important to classify the flow using flow parameters such as Reynolds number and Mach number. However, to determine Reynolds number, a characteristic length of the geometry is required. For flows that are heavily dependent on size and shape of the cyclist, it is difficult to obtain a standard length that can be used universally. Crouch et al. (2014) chose the torso length of the cyclist i.e. the streamwise length from the back of the neck to the lower back. The typical Reynolds number based on a torso length of 600 mm is of the order of 10^5.

Drag of any body is quantified using drag coefficient (C_D) which determines the aerodynamic efficiency of the body. The drag coefficient is dependent on a number of factors including Reynolds number (Re), geometry, orientation, surface roughness and freestream turbulence. Typical drag coefficient values for cyclists lie in the range of 0.6 to 0.8 depending on cyclist position and frontal area (Crouch et al., 2017). However, the determination of drag coefficient requires the frontal area of the cyclist which is rather difficult to determine accurately. Hence, the common convention in the field of cycling is to express aerodynamic efficiency in terms of drag area (C_DA) so that the uncertainty in the evaluation of frontal area is not introduced. Typical drag areas of cyclists are of the range 0.2 m^2 to 0.3 m^2 (Lukes et al., 2005). Drag area of the cyclists is determined using the following formula:

$$C_DA = \frac{D}{\frac{1}{2}\rho V_{\text{cyc}}^2} \tag{2.3}$$

2.3. Single Cyclist Aerodynamics

Research of cycling aerodynamics dates back to as far as the 1950s where Nonweiler (1956, 1958) studied the performance of dropped handlebars in the wind tunnel for a range of speeds. The study found their results to be repeatable within 3% and were able to conclude that drag varies with the square of speed.

Some early research of cycling aerodynamics also involved indirect methods of drag evaluation by measuring oxygen consumption (Pugh, 1974), towing cyclists (Di Prampero et al., 1979) and power requirements (Bassett et al., 1999).

In one of the most detailed studies conducted at the time, Kyle and Burke (1984) researched various methods of improving the racing bicycle with a particular focus on aerodynamics. Wind tunnel tests and coast-down methods were used to evaluate aerodynamic performance. It was found that aerodynamic contribution to total resistance was 90% at racing speeds of above 35 km/h. The largest contributor to the total drag was found to be rider at 65%. Three different positions were studied i.e. upright, dropped and hill-descent and it was found that the hill-descent position had 28% less drag compared to upright and the dropped position had 20% less drag compared to upright (Figure 2.2).

A lot of early research also focused on rider position such as Zdravkovich et al. (1996), Grappe et al. (1997) and Gibertini and Grassi (2008). All of them confirm the finding that the time-trail position is the most optimum due to the parallel alignment of torso and arms with respect to the ground.

Further, detailed studies have tried to improve performance by focusing on aerodynamics of wheels (Godo et al., 2009, 2010; Tew and Sayers, 1999), bicycle frames (Hill, 1993; Kyle, 1991; Zdravkovich, 1992), helmets (Blair and Sidelko, 2009; Chabroux et al., 2008, 2010) and skin suits (Kyle et al., 2004;

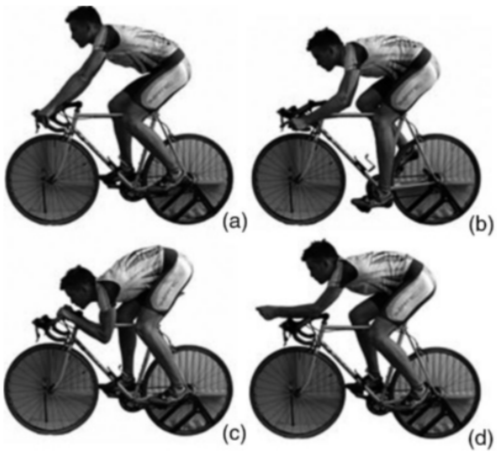

Figure 2.2: Cycling positions: (a) upright; (b) dropped; (c) hill-descent; (d) time-trial (Lukes et al., 2005)

Oggiano et al., 2013). However, it became increasingly clear that the amount of performance gains from these methods were very small compared to the rider position. Moreover, most of the above research did not study the flow structures of the cyclist and hence, was difficult to understand the nature and root cause of the aerodynamic drag. Recently a number of studies have been carried out using experiments and numerical methods in order to study the wake structure of cyclists and understand the mechanics of major flow regimes.

The wake structure for a full-scale static cyclist mannequin in time-trial position has been studied by Crouch et al. (2014). Time-averaged quasi-steady measurements of aerodynamic forces, surface pressures and detailed wake velocity fields were captured for different static leg positions. Velocity fields were measured using a four-hole dynamic pressure probe for a plane of 0.75 m $\times$ 1 m located 0.7 m above the ground. Pressure taps were fixed on the mannequin's back through a fibreglass shell. Further, oil and paint flow visualisation was performed over the torso back of mannequin. The results showed drag variations of the order of 20% over the crank cycle. The authors concluded that these drag variations are primarily due to changes in large-scale flow structures and not due to changes in frontal area.

Streamwise counter-rotating vortices in the wake of the cyclist were reported with two primary flow regimes i.e. the symmetrical flow regime having low drag, where crank arms are close to horizontal and the asymmetrical regime having higher drag, with one of the legs stretched (Figure 2.3). The vortices in the symmetrical regime were observed to originate from the upper and inner thighs, while the vortices in the asymmetrical regime originated from upper hip of the stretched leg and from the rear of the hip of the folded leg.

An experimental and computational analysis of the the same was carried out by Griffith et al. (2014) where qualitative agreement between the two methods were observed, confirming the variation of drag with crank angle. The CFD results under-predicted the experimental results by 15%, which was attributed to simplification of the CFD geometry. The study also emphasised the unsteady behaviour of the wake, specifically the separation of the flow from the cyclist body. The paper discussed the strengthening of the wake vortices when either thigh becomes perpendicular to the flow direction.

Moving on to dynamic pedalling cyclists, follow-up research by Crouch et al. (2016) studied the flow topology for a range of reduced pedalling frequencies. The reduced pedalling frequency, k_f was defined as the ratio between the rotational velocity of the crank to the linear velocity:

$$k_f = \frac{2\pi r_c f_p}{V_{\text{cyc}}} \tag{2.4}$$

Where r_c is the crank arm length, f_p is the pedalling frequency and V_{cyc} is the relative cyclist velocity. Four values of reduced frequencies were tested between 0 (quasi-steady) and 0.115 (elite-level). Wake surveys of 2 m $\times$ 2 m at 0.64 m behind the saddle is captured. The study showed that phase-averaged

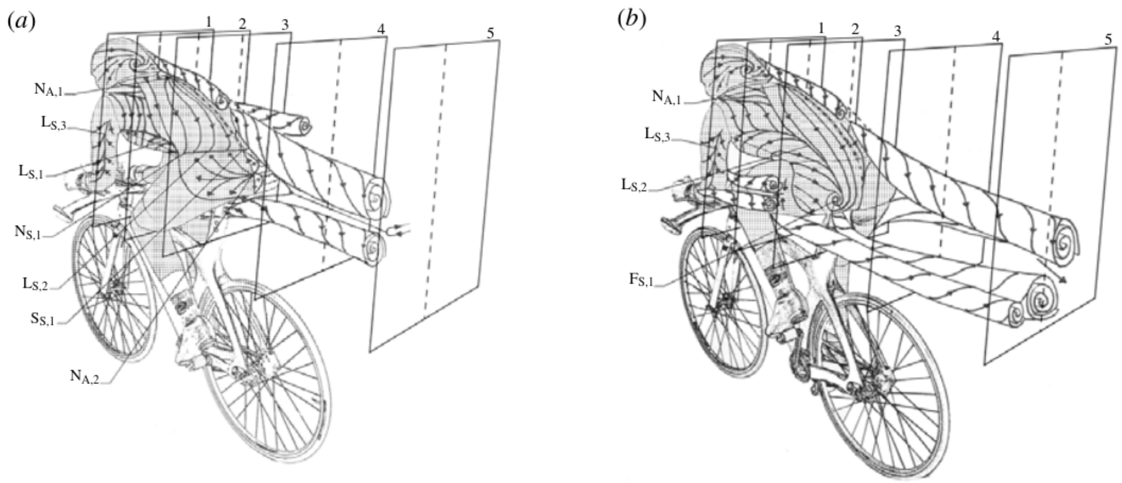

Figure 2.3: Wake vortex visualisation: (a) symmetrical low drag regime; (b) asymmetrical high drag regime (Crouch et al., 2014)

velocity fields are consistent with static cases and show minor variations across pedalling frequencies. A comparison of the phase-averaged drag between a pedalling and quasi-steady mannequin showed that variation of drag over the crank cycle during pedalling is lower compared to quasi-steady measurements (Figure 2.4). Further, the results showed that the adoption of non-uniform pedalling rate or non-circular pedalling stroke may be areas where aerodynamic performance improvements may be achieved.

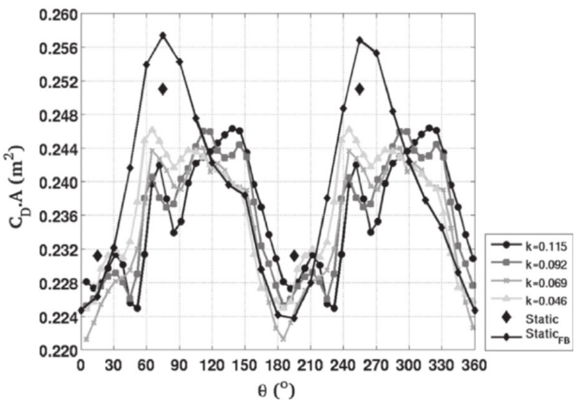

Figure 2.4: Variation of phase-averaged drag area with crank angle (Crouch et al., 2016)

Large-scale tomographic-PIV was applied for the first time on a full-scale static cyclist mannequin by Terra et al. (2016b). A measurement volume of 100 cm × 170 cm × 3 cm was captured using HFSB as flow tracers at 4 m/s and 1 m behind the cyclist saddle. The study found that flow structures agreed well with those described by Crouch et al. (2014). The study applied integral momentum conservation to the control volume to obtain drag and the results agree well with force balance measurements. The study also concluded that the accuracy of the drag measurements could be increased by reconstructing pressure from PIV velocity fields instead of replacing pressure term with the irrotational induced drag term.

Particle Tracking Velocimetry (PTV) was used to study the cyclist wake by Shah (2017). Experiments were conducted with a static mannequin at 14 m/s and 0.8 m behind the saddle, capturing a field of view of 1 m × 1.6 m. The study reported Lagrangian particle tracking to be more accurate than high-speed tomographic-PIV for large-scale measurements of cyclists. The wake structure obtained from this method was found to agree well with literature and drag was obtained using the control volume approach. The drag estimates for different velocities was found to be accurate within 5% of balance measurements.

Jux (2017) used a novel robotic Coaxial Volumetric Velocimetry (CVV) system to capture the flow field around a full-scale static cyclist mannequin. Time averaged flow field on a 2 m^3 domain is obtained for a freestream velocity of 14 m/s. The flow topology agreed well with those established in literature and provided new insights in surface friction, stagnation points, separation and reattachment (Figure 2.5).

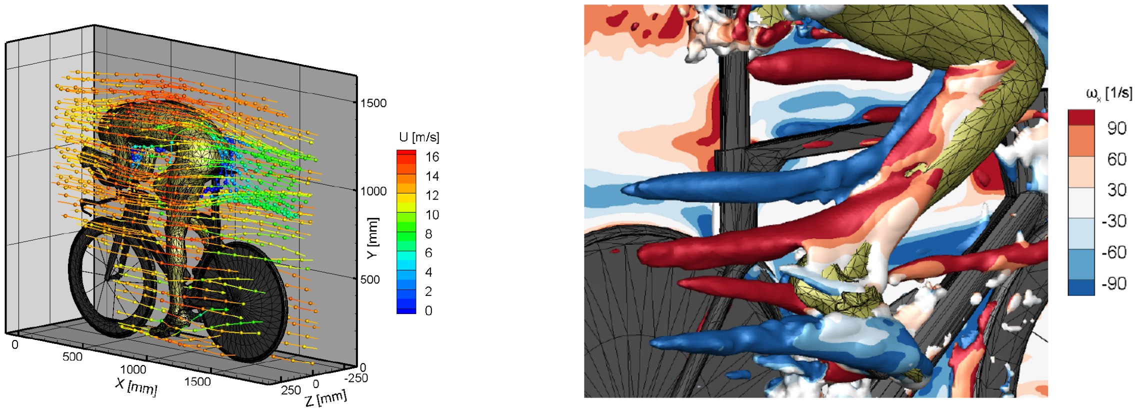

(a) Streamlines coloured by streamwise velocity

(b) Isosurfaces of Q-criterion coloured by streamwise vorticity

Figure 2.5: Robotic coaxial volumetric velocimetry results (Jux, 2017)

2.4. Drafting Aerodynamics

Drafting is the phenomenon where a cyclist travelling in the wake of another cyclist experiences lower aerodynamic drag, which translates to the trailing cyclist utilising lower power to travel at the same speed. Drag reductions of the order of 50% have been reported for a trailing cyclist closely following another. This phenomenon has been used extensively by cyclists in various racing events.

Concerning drafting aerodynamics of cyclists, it was understood early on that this aerodynamic benefit primarily depends on distance between the cyclists. However, the mechanism of this drag reduction as well as its dependence on distance was not very well established, with considerable variation in drag reduction between different studies. Recent developments in the fields of computing resources and experimental methods have helped gain new insight into its behaviour.

2.4.1. Effect of Distance

A number of studies have quantified the performance benefit for the trailing cyclist while drafting. This reduction was found to be maximum at minimum distance between the cyclist and decreased with increasing distance. However, the exact dependence of drag reduction on the distance between the cyclists was found to be inconsistent between studies.

Kawamura (1953) and Kyle (1979) conducted one of the first studies investigating the effect of drafting distance on aerodynamic drag. While the former conducted scaled wind tunnel tests, the latter conducted experiments in an enclosed 200 m coast-down track. Total resistance force was determined by measuring the rate of deceleration through the coast-down track. Figure 2.6a shows that these early studies do not agree with each other, with Kawamura (1953) reporting a maximum drag reduction of 54% while a maximum of 38% for Kyle (1979). In fact, the wind tunnel results show higher reductions for all drafting distances. Scaling effects and wind tunnel boundary layer effects are cited as possible sources of error for the former, and the latter mentions the difficulty in maintaining constant longitudinal and lateral distance between the cyclists. Further, coast-down tests are also limited by wind variation which was not recorded by the author.

Zdravkovich et al. (1996) performed wind tunnel measurements of two full-scale cyclists drafting for twenty different positions in tandem and staggered arrangement. Force balance measurements

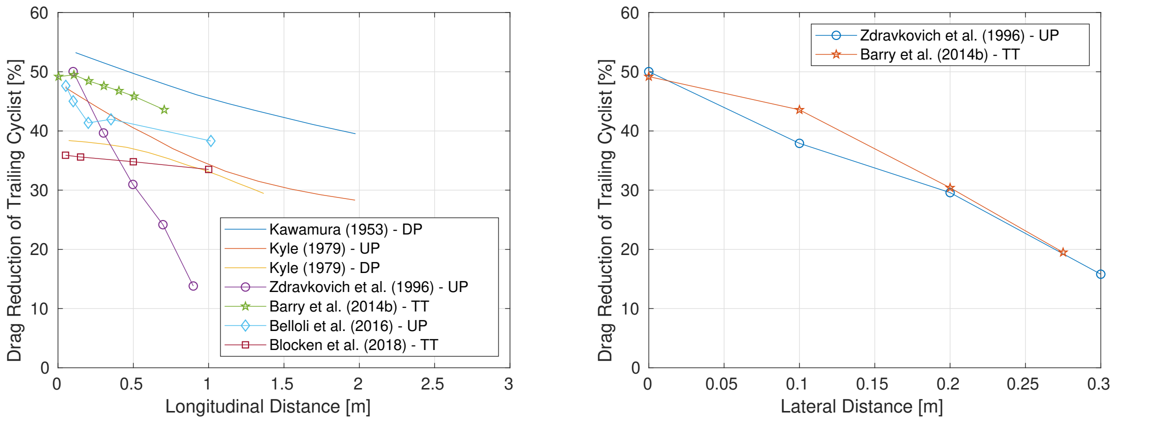

(a) Effect of longitudinal distance on drag reduction (at zero lateral spacing)

(b) Effect of lateral distance on drag reduction (at zero longitudinal distance)

Figure 2.6: Variation in findings regarding effect of distance

showed a maximum drag reduction of 49% for the closest tandem position. The study reported a very high decay of drag reduction with drafting distance with only 11% drag reduction at 0.9 m downstream of the first cyclist, which is lower than those reported by other studies. Further, a drag increase is reported for drafting distances of 20 cm and 30 cm in the staggered arrangement. Although wind tunnel tests are known for their high accuracy and precision, the experiments of Zdravkovich et al. (1996) were conducted with a blockage ratio of 15%. Also, it seems that the test subjects were quite close to the wind tunnel walls and cyclist wake could have potentially interacted with the boundary layer of the walls. It is not clear whether corrections for these effects were included in the results. Further, the measurements were taken with two cyclists whose isolated drag values differed by 30%. As a result, the decay of drag reduction with distance was different depending on which cyclist was leading, indicating the dependence on drag reduction on cyclist size as well as distance.

Recent wind tunnel studies on drafting distances were conducted by Barry et al. (2014) and Belloli et al. (2016). While the former studied the effect of both longitudinal and lateral distances using an athlete and a full-scale mannequin, the latter studied only the effect of longitudinal distance with two athletes. Force balance measurements were used to record the aerodynamic drag. Comparison of the results show although the drag reduction at minimum gap agree well with each other and with previous studies, the results disagree at higher longitudinal distances (Figure 2.6a). However, both authors report that the size of the leading and trailing cyclists are not the same, with the trailing cyclist being smaller in size compared to the leading. Thus, the drag reduction quoted in the study might not apply when the positions are reversed.

Both Zdravkovich et al. (1996) and Barry et al. (2014) showed that a change in lateral distance had a higher (negative) impact on drag reduction compared to a similar change in longitudinal distance (Figure 2.6b).

CFD simulations by Blocken et al. (2018) investigated the effect of longitudinal distance on drag reduction. 3D steady RANS approach was chosen along with a cyclist CFD model that included the bicycle. The results under-predicted the drag reduction for all longitudinal distances with a maximum drag reduction of 36% at minimum spacing. It can be seen in Figure 2.6a that the decay of drag reduction with distance is very low compared to other studies.

From the above studies, the general consensus is that drag reduction varies inversely with both longitudinal and lateral distances. However, the similarities end there with each study showing different decay rates of drag reduction with longitudinal distance. It is to be noted that a deeper investigation of these studies revealed several variations in their research methodologies such as the choice of freestream velocity, cyclist size, position and leg position (Table 2.1). As discussed in the aerodynamics of single cyclists, drag of the upright position differed by 20% compared to the time-trail position and drag of the symmetric leg position further differed by 15% compared to the asymmetric leg position. It can be concluded that the inconsistencies in the results between the studies can be attributed to a combination of these variations in research methodologies along with the limitations of each study such as scaling effects, imperfect drafting alignment, blockage effects and repeatability.

Table 2.1: Variation in research methodologies between studies

Study	Approach	Velocity [m/s]	Cyclist Position	Leg Position
Kawamura (1953)	Wind Tunnel	N/A	DP	N/A
Kyle (1979)	Coast-down	11.1	UP & DP	N/A
Zdravkovich et al. (1996)	Wind Tunnel	8.2	UP	N/A
Barry et al. (2014)	Wind Tunnel	18.1	TT	Symmetric
Belloli et al. (2016)	Wind Tunnel	13.9	UP	Pedalling
Blocken et al. (2018)	CFD	15	TT	Symmetric

2.4.2. Effect of Cyclist Size, Position and Posture

In the previous section, it was observed that athletes had different heights and weights across studies. It is evident that these athletes will thus have different frontal areas. Following this train of thought, it is logical to assume that the size of the wake is proportional to the frontal area (or size) of the cyclist. The amount of "sheltering" gained by a trailing cyclist depends on the size of the wake ahead, but also depends on his/her size (or frontal area) as well. This particular hypothesis was studied by Edwards and Byrnes (2007) where the influence of aerodynamic and anthropometric characteristics of both leading and trailing cyclist was researched. The study was conducted on a 200 m straight flat track, using hub-based power meters at 45 km/h and inter-wheel distance less than 0.5 m. Based on individual cyclist measurements, three cyclists were identified as maximum, median and minimum based on on their respective drag areas (i.e. $C_D A$). These cyclists were chosen as leaders for various two cyclist drafting configurations.

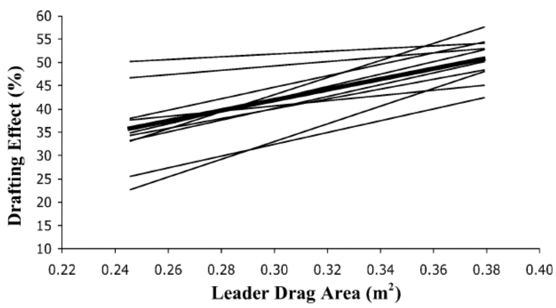

Figure 2.7: Variation of drag reduction with drag area of leading cyclist (Edwards and Byrnes, 2007)

The results showed that the drafting benefit for the second cyclist increased with increasing drag area of the leading cyclist (Figure 2.7). The average drag reduction for the trailing cyclist based on the size of the leading cyclist was found to be 51%, 41% and 35% for the maximum, median and minimum cyclist respectively. However, large variations were observed between different trailing cyclists for the same leading cyclist. The authors stated that although the leader drag area played an important role, it was not the only factor affecting drag reduction, which can be observed in the inconsistencies between the regression slopes in Figure 2.7. A number of correlations were calculated such as ratios of leader to drafter drag areas, ratio of frontal areas and ratio of drag coefficients to explain this variability. However, no significant correlation was obtained for any of the proposed ratios with the drafting benefit. Due to the low correlation coefficients, the authors suggested that drag coefficient had lower importance compared to drag area or frontal area. Further, the authors concluded that these variations could also be attributed to drafting skill i.e. the ability of the cyclists to maintain a constant drafting distance and alignment with the leader. Another possible reason for the low correlation could be the small number of observations for each configuration, suggesting high statistical uncertainty.

The effect of the position adopted by the cyclist on drag reduction was studied by Blocken et al. (2013). 3D steady RANS simulations of two cyclists drafting were conducted with the CFD model including only the cyclist body and omitted the bicycle to reduce complexity. It was ensured that there was no variation in size of the cyclists. Simulations were performed for configurations where both the cyclist adopted the upright, dropped and time trial positions.

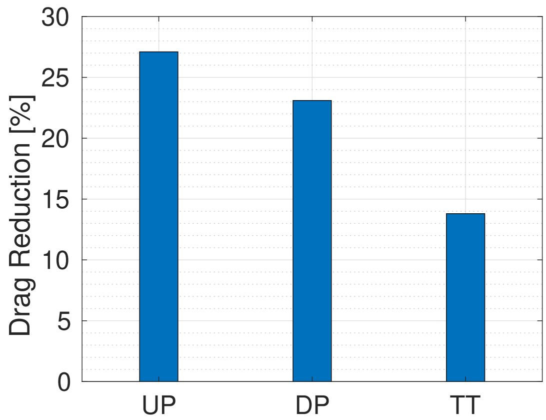

Figure 2.8: Dependence of drag reduction on cyclist position (Blocken et al., 2013)

The results showed drag reduction of 27.1%, 23.1% and 13.8% at minimum spacing for the upright, dropped and time trial positions respectively (Figure 2.8). The study reported that when both the cyclists adopted the time trial position, the trailing cyclist was more exposed to the freestream compared to the other cases, which resulted in lower "sheltering". Thus, it can be seen that the amount of benefit obtained depends not only on size, but also on the position adopted by the drafting cyclists.

The effect of cyclist size and posture was studied by Defraeye et al. (2014) using CFD simulations. The study involved four cyclists in a pace-line with the size and posture of each cyclist different from each other (Figure 2.9). Here, posture refers to the variations in the way a cyclist adopts the time trail position i.e. head raised, head lowered, arms spacing, etc. and does not refer to the "position" adopted by the cyclists (i.e. upright, dropped and time trial). With these cyclist models, four drafting configurations were tested with the position of each cyclist in the pace line being rotated. Further, each configuration of four cyclists was tested for two different arm spacings i.e. arms close together and far apart. The simulations were performed using the 3D steady RANS approach and to simplify the geometry, the bicycle was excluded from the CFD model.

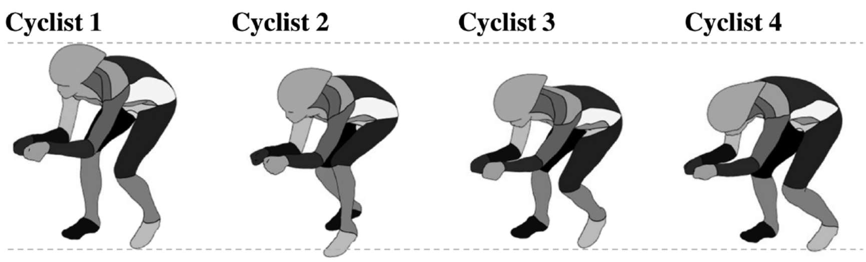

Figure 2.9: The four different CAD models of cyclists used by Defraeye et al. (2014)

The results showed that the highest drag reduction was obtained in the configuration where the largest cyclist was leading the smallest cyclist. In addition, a pronounced reduction in drag area is observed for the cyclist trailing the largest one in all configurations. The sum of drag areas of all cyclists was found to vary by small margins for different configurations. It was found that the lowest overall drag corresponded to the configuration where the largest cyclist was leading the pace-line and conversely the configuration where the largest cyclist at the back of the pace-line had the highest overall drag.

The results also showed higher drag area for the wider arm spacing in all configurations, individual and pace-line.

A similar study in the wind tunnel was conducted by Barry et al. (2015). Experiments were performed with four athletes in a pace-line while measuring the drag force of each athlete simultaneously using a bespoke force balance rig. Four riding postures were investigated based on the posture of the athlete's head (Figure 2.10). Further, the four athletes had different heights and weights as well.

Figure 2.10: Riding postures adopted by athletes: baseline, head raised, head lowered, elbows together (Barry et al., 2015)

The study concluded that postures that reduced drag for an individual cyclist had a higher reduction in a team environment while postures that increased drag for an individual cyclist had a lower drag increase in team environment. The study showed that changing the posture of any cyclist in the pace-line did affect the drag of other cyclists. However, the conclusions from the previous studies were not universally observed e.g. increasing the drag area of the leading cyclist resulted in both increase and decrease in drag reduction for the trailing cyclist. The author stated that these variations are caused due to subtle differences between each cyclist size and body shape and the interactions between these differences. Further, the study concluded that the drag interactions between the different cyclist in a peloton was a highly complex phenomenon that cannot be generalised for all athletes.

Apart from frontal area and posture, the effect of cyclists' mass was investigated by Fitton et al. (2018). Power meter measurements were made in a velodrome for different four-cyclist pace-line configurations. The results showed that the drag reduction experienced by a trailing cyclist correlated highly with the difference in mass between the leading and trailing cyclist. This correlation was found to be stronger compared to the correlation with the difference in drag areas. However, this correlation was only strong for the second cyclist in the pace-line and not for the other cyclists.

From the above discussion, it is clear that a number of studies have shown the dependence of drag reduction on the size of the cyclists involved, positions adopted by the cyclists and the variations in posture. Factors like bigger cyclist size, wide arm spacing, raised head, etc. that increased the drag area of the leading cyclist resulted in higher drag reductions for the trailing cyclist. Conversely, factors that increased the drag of the trailing cyclist resulted in lower drag reductions. Although this hypothesis was not observed universally, it can be argued that imperfect alignment, cyclist drafting skill and the presence of more than two cyclists could have influenced these measurements.

2.4.3. Drag Reduction of Leading Cyclist

Early studies on drafting aerodynamics hypothesised that during drafting, the leading cyclist also gains a benefit (Olds, 1998). The idea was that the low pressure in the wake of the leading cyclist was "filled" by the trailing cyclist. However, studies by Kyle (1979) and Zdravkovich et al. (1996) could not quantify this benefit. Numerical studies by Iniguez-de-la Torre and Iniguez (2009), Blocken et al. (2011) and Blocken et al. (2013) showed that there is indeed a benefit for the leading cyclist using CFD simulations. The drag reduction on average was found to be $\leq$5%, which is very low compared to the drag reduction for the trailing cyclist. Wind tunnel test also confirmed the drag reduction of the leading cyclist (Barry et al., 2014) with a maximum drag reduction of 5% at minimum spacing between the cyclists. Similar findings are reported by other studies by Defraeye et al. (2014), Barry et al. (2015), Belloli et al. (2016), Fitton et al. (2018) and Blocken et al. (2018).

This drag reduction was again inversely proportional to the distance between the cyclists. Results by Barry et al. (2014) also showed that the drag reduction for the leading cyclist had a strong dependence on longitudinal distance while lateral distance had a weaker influence.

Further, Blocken et al. (2013) showed that the highest drag reduction was obtained for the leading cyclist when both the cyclists adopted the time trial position as opposed to upright position. However, detailed studies have not been found in literature which study the effect of size and posture on the drag reduction of the leading cyclist.

2.4.4. Flow Topology

Most of the above discussion focused mainly on quantitative measurements of drag reduction while drafting. It is equally important to understand the behaviour of flow structures while drafting. In the previous section on single cyclist aerodynamics, it was understood that the flow around cyclists is characterised by large-scale streamwise counter-rotating vortices. Now the question arises, how do these flow structures behave in the presence of another cyclist?

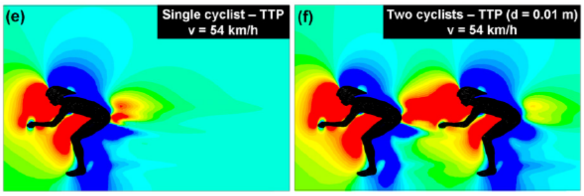

(a) Pressure coefficient contours in the vertical plane

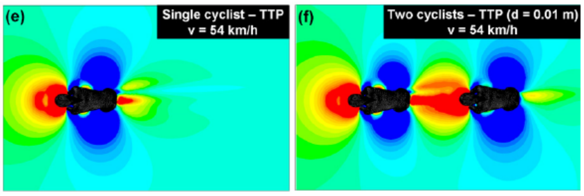

(b) Pressure coefficient contours in the horizontal plane

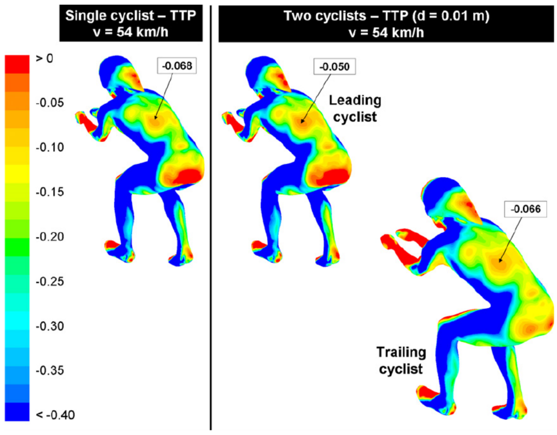

(c) Surface Pressure contours on cyclist body

Figure 2.11: Comparison of pressure coefficient contours between individual and drafting cases by Blocken et al. (2013)

Blocken et al. (2013) provided detailed analysis of pressure fields of two cyclists drafting using results from their CFD simulations. It can be seen from Figures 2.11a and 2.11b that the pressure fields of the cyclists interact with each other. Surface pressure contours of the cyclists was also compared and using the peak pressure values on the cyclists' back (Figure 2.11c), the following observations was made by the authors:

- The low pressure region in the wake of the leading cyclist while drafting was smaller compared to the individual case. This was due to upstream propagation of the high pressure region in front of the trailing cyclist.
- The high pressure in front of the trailing cyclist was reduced and the low pressure region in the wake of the trailing cyclist was alleviated. This effectively reduced the deficit in pressure across the trailing cyclist which was essential for drag reduction.

Wake studies were conducted by Barry et al. (2016b) for scaled static cyclist models in a water tunnel. Planar PIV measurements were conducted for a Reynolds number one order of magnitude lower than full-scale. Figure 2.12 compares the streamwise velocity contours between a single cyclist wake and in-between two cyclists while drafting. It was shown that the peak velocity while drafting at minimum spacing was lower compared to an individual cyclist, whereas for the case with higher spacing, the wake was similar to that of an individual cyclist. The authors suggested that the lower peak velocity in-between the cyclists was due to upstream interference of the trailing cyclist.

The vorticity field in the wake of the trailing cyclist was also compared with that of an individual cyclist (Figure 2.13). It was reported that the dominant flow structures in the wake of the trailing cyclist were

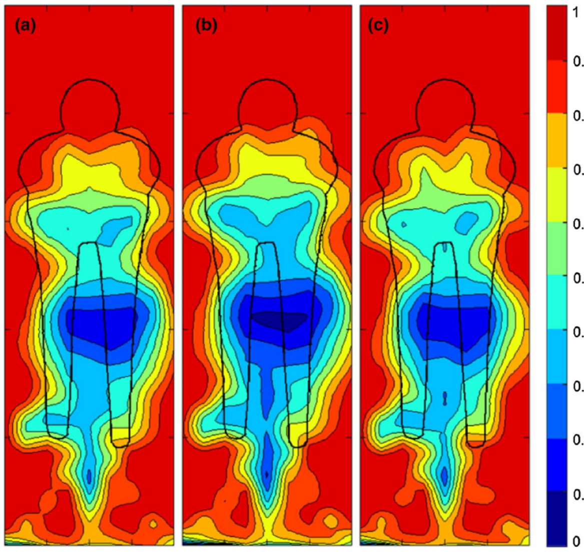

Figure 2.12: Streamwise velocity contours: (a) single cyclists wake, (b) in-between two cyclists at minimum wheel spacing, (c) in-between two cyclists at one bicycle length spacing (Barry et al., 2016b)

still characterised by upper hip vortices. However, a reduction in magnitude of vorticity was observed across the wake, which was attributed to low energy inflow for the trailing cyclist. Also, it was reported that the vortices were displaced downward and away from the centre due to changes in local in-plane velocity components. At higher spacing between the cyclists, the wake more closely resembled the wake of an individual cyclist as three ordered pair of counter-rotating vortices near the hips and lower back was observed at approximately the same locations.

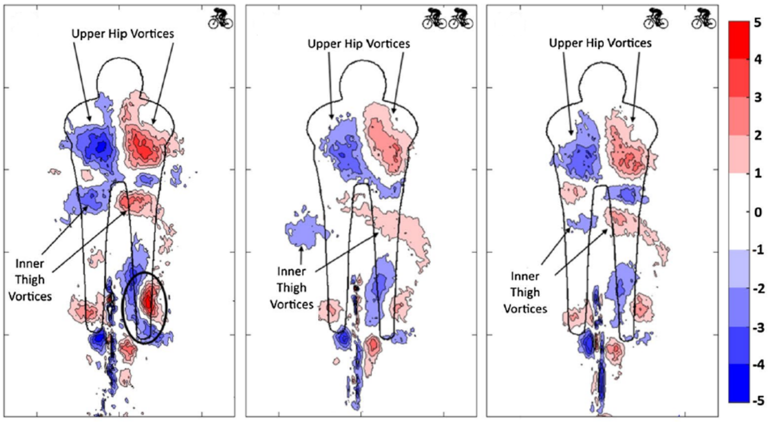

Figure 2.13: Streamwise vorticity contours: (a) single cyclists wake, (b) trailing cyclist wake at minimum wheel spacing, (c) trailing cyclist wake at one bicycle length spacing (Barry et al., 2016b)

The authors concluded that the primary mechanism responsible for drag reduction was due to the low energy inflow conditions for the trailing cyclist which resulted in lower relative velocity deficit. This low-energy inflow also resulted in diffusion of the peak vorticity in the wake of the trailing cyclist. However, this diffusion was considered to be “secondary contributors” to the drag reduction mechanism. Further, as the spacing between the cyclists was increased, the low-energy flow in-between the two cyclists was able to recover, closely resembling the individual cyclist wake and consequently, the wake of the trailing cyclist also agreed well with the individual cyclist wake.

Full-scale wake studies were also conducted in a follow-up study by Barry et al. (2016a) in the wind tunnel. Pressure probe measurements were made for a mannequin and pedalling athlete configuration covering a field of view of 0.8 m $\times$ 1 m. Results of time-averaged streamwise velocities showed a higher peak velocity in the wake of the trailing cyclist compared to single cyclist wake. Further, phase-averaged results showed that the wake of the trailing cyclist did not exhibit a pronounced reduction in vorticity magnitude compared to the single cyclist wake, indicating that drag reduction is not due to disruption of the dominant flow structures in the wake.

2.5. Methods of Assessment

In the above discussions, it can be seen that there are a number of qualitative and quantitative ways to study the aerodynamics of cyclists. Each method comes with its own advantages and disadvantages, which is briefly summarised below.

2.5.1. Wind Tunnels

Wind tunnels are one of the oldest and most common methods of investigating cycling aerodynamics as they offer a controlled and repeatable environment for testing a range of conditions. In the wind tunnel frame of reference, the object is stationary and the fluid flows around it, which is opposite to what happens in reality where the object is moving while the fluid is relatively stationary. Typical wind tunnels focus on quantitative measurements of forces and moments using force-balances, which are known for their very high accuracy and precision. Recent developments in flow measurement techniques have helped both qualitative and quantitative measurement such as oil and smoke flow visualisation, pressure taps and probes, hot wire anemometry and PIV, which provide useful information for flow diagnostics and topological analysis.

However, there are some disadvantages of wind tunnel testing such as scaling effects which affect measurements performed with scaled down models. These cases are usually performed at a Reynolds number that is an order of magnitude lower than full-scale, such as the water tunnel experiments by Barry et al. (2016b). In this particular case, it was found that the diffusion of flow structures was higher compared to the full-scale results.

Blockage effects are another limitation of wind tunnel tests which affect the forces measured. The measurements of Zdravkovich et al. (1996) were known to have blockage of up to 15%. At such high levels of blockage, certain corrections have to be made to the forces. However, it is not clear whether the results presented by the author included these corrections.

Other general limitations of wind tunnel tests are boundary layer development in the test section. Possible ways of countering this limitation is by conducting measurements on a raised platform, or certain tunnels have a moving floor arrangement to ensure no relative motion between the fluid and ground. Another issue is the repeatability of measurements, which can be tricky to achieve when athletes are used as it is difficult to maintain certain positions and postures accurately for long periods of time. Recent measurements have employed the use of mannequins which overcome this limitation. High-tech mannequins also come with pedalling legs to simulate the movement of the legs over the crank.

Wind tunnel facilities are designed to operate at very low freestream turbulence conditions along with high flow uniformity as this is essential for repeatability of results. However, the freestream conditions of on-site sports environments are characterised by gusts, atmospheric turbulence, air currents etc. which affect flow phenomenon such as transition, separation and reattachment especially for bluff bodies such as cyclists. Therefore, design and study based specifically on wind tunnel tests may not perform exactly the same way in reality.

With the advent of flow measurement techniques, new challenges arise such as setup of pipes and instruments for pressure probes. This problem becomes further cumbersome when surface measurements have to be made. PIV systems require optical access for laser and camera systems which is difficult to obtain in certain cases (Barry et al., 2016b).

2.5.2. Track Testing

Another type of experimental testing includes track testing where cyclists' performance is measured on-site using various techniques such as coast-down tests (Kyle, 1979; Kyle and Burke, 1984), oxygen consumption (Pugh, 1974) and more recently using hub-based power-meters (Bassett et al., 1999; Broker et al., 1999; Edwards and Byrnes, 2007; Fitton et al., 2018).

The advantages of such tests are that they are most representative of the performance in the "real" world as simplifications necessary to conduct wind tunnel tests are usually not made in these cases. However, the uncertainties of these measurements are higher than wind tunnel tests due to uncontrollable factors such as wind, rolling resistance, drive train losses, track gradients, cyclist skill, etc.

2.5.3. Numerical methods

Numerical methods involve simulating the flow around cyclists by solving the discretised Navier-Stokes equations. Improvements and advancements in meshing and turbulence modelling in recent years have made CFD a popular method to investigate cycling aerodynamics. Advantages of CFD include availability of full flow field information in space and time along with aerodynamic forces and moments. Further, the aerodynamic forces can be broken up into its constituent viscous and pressure components, which is useful for flow diagnostics.

Broadly speaking, CFD simulations are classified into Direct Numerical Simulations (DNS), Large Eddy Simulations (LES) and Reynolds Averaged Navier-Stokes (RANS) approaches, corresponding to decreasing accuracy and increasing modelling complexity respectively. Reasonably accurate results can be obtained using the RANS approach which has been used extensively in literature (Blocken et al., 2013, 2018; Defraeye et al., 2014; Griffith et al., 2014). However, it can be also be observed that CFD simulations require some simplifications especially with respect to the geometry such as omission of bicycle. The results from these simulations usually under-predict the aerodynamic forces and neglect the flow interactions between the rider and the bicycle. Further, CFD results are sensitive to domain size, initial conditions, mesh resolution, turbulence model and numerical schemes to name a few.

2.5.4. Ring of Fire

Based on the above discussion, it is clear that there is a need for techniques that measure both aerodynamic forces and flow field data for full-scale cyclists. Preferably, such a technique should also overcome the limitations of wind tunnel testing. Recent developments in the field of large-scale PIV with the use of HFSB as flow tracers gained a lot of traction, which led Sciacchitano et al. (2015) to envisage the novel “Ring of Fire” measurement technique. The technique involves performing large-scale stereo-PIV of transiting objects using HFSB. Measurement of flow fields upstream and downstream of the object enables one to evaluate integral momentum deficit analysis to obtain drag force.

The first study employing this technique was carried out by Terra et al. (2016a), where tomographic PIV measurements for a volume of 3 cm $\times$ 40 cm $\times$ 40 cm was recorded for a transiting sphere of diameter of 0.1 m moving at a velocity of 1.5 m/s. Drag obtained using the control volume approach was found to have large variation in the near wake region (< 2 diameters) and lower variations (of order of 1%) in the far wake. Regardless, the time-averaged drag agreed well with literature. Also, it was found that the pressure contribution decays rapidly with distance in the wake and thus in the far wake, pressure term can be neglected.

Ring of Fire was applied to a full-scale cyclist for the first time by Spoelstra (2017) in an outdoor environment (Figure 2.14a). Time-resolved stereoscopic-PIV measurements were taken in the wake of a transiting cyclist to determine the feasibility of the measurement system. Phase-averaged velocity fields were obtained over a measurement plane of 1 m $\times$ 1.7 m. Hip and thigh vortices were observed and agreed well with literature. As the measurements were made on-site, it was found that the wake interaction with the ground was not seen as opposed to that of wind tunnel measurements. The resulting drag measurements was found to have an uncertainty of 5% and differed by 10% when compared to wind tunnel measurements. The main issues expressed by the author was the tendency of the wake to move outside the measurement window and time required for data transfer between camera and acquisition computer.

The measurement system was used with a low-speed acquisition system and in an indoor environment by de Martino Norante (2018). To increase accuracy of measurement system, a larger tunnel structure was chosen to eliminate blockage effects (Figure 2.14b). Drag measurements were taken for upright and time-trail positions for symmetric, asymmetric and dynamic leg positions. The results showed that the uncertainty was reduced to 2% and the use of low-speed system reduced the transfer time to a maximum of 2 min from 8 min. The flow structures were in agreement with those found in literature and additional vortices were also identified for the upright position. Improvements in Dynamic Spatial Resolution (DSR) and Dynamic Velocity Resolution (DVR) was found due to low freestream turbulence in the indoor facility.

The most recent Ring of Fire measurements were conducted by Hirsch (2018) where drag values were compared with simultaneously acquired power-meter data. Measurements with athletes in upright and time-trail position, different helmets and also long distance drafting were performed using the same

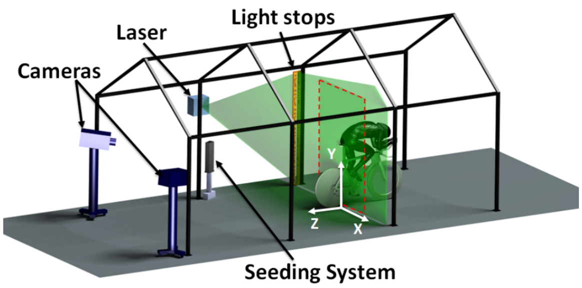

(a) Schematic of setup by Spoelstra (2017)

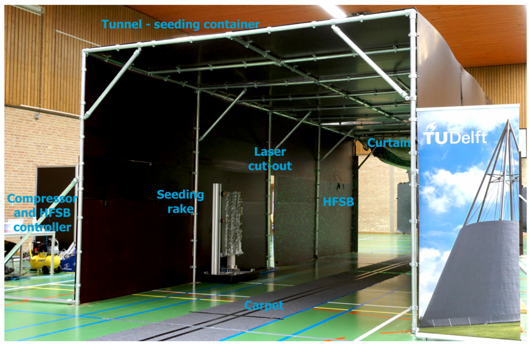

(b) Schematic of setup by de Martino Norante (2018)

Figure 2.14: Previous Ring of Fire experimental setup

tunnel structure as de Martino Norante (2018). The resulting drag measurements agreed well with power meter data and also previous studies. Drafting studies were conducted for longitudinal distances of 5 m to 10 m, with a drag reduction of 15% for the trailing cyclist and negligible drag reduction for distances above 9 m. The flow topology of drafting was found to agree with those found in literature. The main issue faced by the author was the artificial circulation created by continuous motion of the cyclists in a loop, which was counteracted by moving a large blanket in the opposite direction.

2.6. Research Questions and Thesis Objectives

From the above review of literature, it is apparent that there are large inconsistencies among studies regarding the effect of distance, cyclist size and posture. Further, very few studies have focused on the flow topology of drafting with the flagship paper conducting planar PIV on scaled models at a lower Reynolds number. There exists a need for a study that involves full-scale cyclists tested at conditions that are representative of competitive racing scenarios and also involving non-intrusive flow measurement for flow diagnostics. Given the recent development of Ring of Fire system by de Martino Norante (2018); Hirsch (2018); Spoelstra (2017), it seems that this need can be addressed using this technique. Based on the above research gap, the following objective is formulated for the current thesis:

"*Assess the feasibility of the Ring of Fire system for full-scale on-site drafting cyclists. Further, study the effect of cyclist size and drafting distance on drag reduction for two drafting cyclists.*"

An important aspect to understand the flow topology of drafting is to obtain flow fields in-between the cyclists while drafting. This poses a challenge in terms of optical access for the PIV acquisition system of Ring of Fire. Hence, the feasibility of the technique to perform such measurements has to be determined. As velocity fields of full-scale cyclists in close distance drafting have not been obtained on-site before, the results of the current experiments will provide important insight into the flow dynamics of drafting. Specifically, the current research aims to understand the effects of cyclist size and drafting distance on the aerodynamic drag. The effect of cyclist size is chosen as opposed to cyclist posture as it is difficult to ensure the repeatability of a given cyclist posture in an on-site environment.

A successful conclusion of the project would prove the viability of the Ring of Fire system to measure flow fields of drafting cyclists and eliminate the uncertainty in literature regarding the effect of cyclist size and drafting distance on drag reduction.

3 Theoretical Framework

This chapter briefly describes the theory behind the working principles of the Ring of Fire system, starting with PIV and the various parts of a typical PIV system such as seeding, illumination and imaging. This section details the theoretical basis required to setup and perform the PIV measurements. As the Ring of Fire system employs stereoscopic PIV, this technique is explored in the next section, describing the principle of perspective correction, determination of out-of-plane velocity and camera orientation. The next section discusses the control volume approach where the conservation of momentum is invoked to relate drag force and flow field data. The chapter concludes with the discussion of pressure reconstruction from velocity measurements using the pressure Poisson equation.

Contents

3.1. Particle Image Velocimetry (PIV)

PIV is a non-intrusive quantitative flow measurement technique that involves measuring the displacement of tracer particles in the flow between image pairs. Instantaneous velocity fields are obtained in a plane using these displacements and this technique can also be extended to volumetric measurements of velocity. First developed in the late 1980s, PIV has undergone tremendous development since then. Improvements in laser, imaging and seeding technologies have helped it become one of the most popular flow measurement techniques. The various components of a typical PIV system as shown in Figure 3.1 are discussed below:

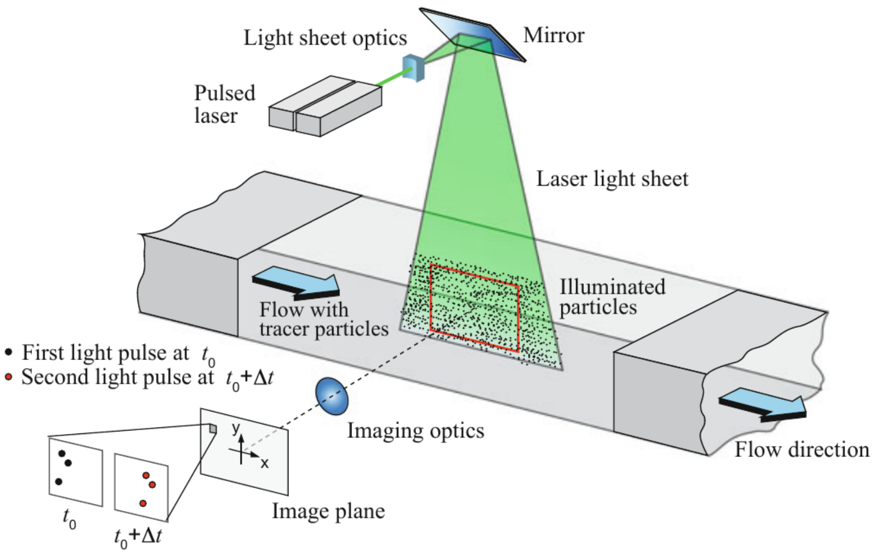

Figure 3.1: Working principle of planar PIV (Raffel et al., 2018)

3.1.1. Tracer Particles

As displacements of particles in the flow are used to determine velocity, the choice of particle is an important one. The particles “seeded” into the flow are chosen based on two major factors namely the flow traceability and light scattering ability. The ability to follow the flow accurately is determined by the slip velocity ($\mathbf{V}_s$), which is difference between the particle velocity and fluid velocity (Raffel et al., 2018):

$$\mathbf{V}_s = \frac{d_p^2\,(\rho_p - \rho)\;a}{18\;\mu} \tag{3.1}$$

Where d_p is the particle diameter, ρ_p is particle density, ρ is fluid density, a is acceleration of particle and μ is fluid viscosity. Low slip velocity corresponds to low response time, which results in better flow traceability. It can be observed that the response time is inversely proportional to the size of the particle and buoyancy of the particle in the fluid. Conversely to particle response time, the light scattering ability is directly proportional to the diameter of the particle and ratio of refractive indices, according to Mie scattering theory (Raffel et al., 2018). Thus, it can be seen that smaller particles are good for following the flow while larger particles are better for scattering light. An optimum particle size has to be found based on the buoyancy of the particle.

HFSB is a particularly novel solution for large-scale flows for their neutrally buoyant properties and large size for light scattering. By filling soap bubbles with Helium (which is lighter than air), the buoyancy can be controlled such that $\rho_p \approx \rho$ (Faleiros et al., 2019). This results in very low response time of the order of 10 μs (Scarano et al., 2015). With this neutral buoyancy, bubble diameters as large as 400 μm are possible. As light scattering intensity is proportional to the square of the particle diameter, these relatively large diameters (compared to fog particles) result in very high light scattering intensities (Bosbach et al., 2009). This improves the contrast of the particle images from the background resulting in better flow field determination.

3.1.2. Illumination

Lasers are primarily used as the light source to illuminate the particles in the flow. There are a number of reasons for this; Lasers produce pulses of very short duration (of the order of 5 ns) that ensures particle images appear as dots and not as streaks. Laser light is collimated which can be easily shaped into thin sheets and volumes using different combinations of optical lenses. For particle reflections to be detected by camera sensors, the particles have to be illuminated with very high light intensities, which is provided by laser light.

Solid-state lasers are commonly used for PIV applications such as the low speed Nd:YAG (neodymium doped yttrium aluminium garnet) laser as their pulse repetition rates are of the order of 10 Hz and the high-speed diode-pumped Nd:YLF (neodymium doped yttrium lithium fluoride) laser which are used for time resolved measurements as their pulse repetition rates are of the order of kHz. These lasers produce monochromatic light having a wavelength of approximately 530 nm.

3.1.3. Imaging

The illuminated particles are observed as light intensity distributions on the pixels of the camera sensor. The camera location can be approximated using the focal length of lens and object distance which is related by the thin lens equation:

$$M = \frac{d_i}{d_o} = \frac{\text{Pixel Size} \times \text{Resolution}}{\text{Field of View}} \tag{3.2a}$$

$$\frac{1}{f} = \frac{1}{d_i} + \frac{1}{d_o} = \frac{1}{Md_o} + \frac{1}{d_o} \tag{3.2b}$$

Where M is magnification, d_i is image distance, d_o is object distance and f is focal length of lens. The particle images appear as Airy patterns as they are affected by Fraunhofer diffraction due to the point-like nature of the light source from the particles and the large distance between the particles and the camera. Neglecting lens aberration effects and considering that the lens focal plane coincides with the illuminated particles, the effective size of the imaged particles (d_τ) is approximated as the Euclidean sum of diffraction diameter (d_{diff}) and geometrical image diameter (d_{geo}):

$$d_\tau = \sqrt{d_{\text{diff}}^2 + d_{\text{geo}}^2} \tag{3.3a}$$

$$d_{\text{diff}} = 2.44\ \lambda\ (1 + M)\ f_{\#} \tag{3.3b}$$

$$d_{\text{geo}} = Md_p \tag{3.3c}$$

Where λ is wavelength of laser light and $f_{\#}$ is the camera f-stop. In usual PIV applications, $d_{\text{diff}} >> d_{\text{geo}}$ and consequently, the effective particle image diameter is approximated as the diffraction diameter, $d_\tau \approx d_{\text{diff}}$. In order to obtain optimum optical sampling of the particle image on the camera pixels, this effective particle diameter has to be twice the size of one pixel of the camera (Adrian et al., 2011). However, the above relations only hold for particles in focus and thus should lie in the depth of field of the camera (Eqn. 3.4). This is the distance between the nearest and farthest object in focus by the camera.

$$\delta z = 4.88\ \left(\frac{1+M}{M}\right)^2\ f_{\#}^2\ \lambda \tag{3.4}$$

This essentially means that the laser sheet thickness has to be less than or equal to the depth of field. Thus, it can be observed that an optimum f-stop has to be chosen based on the effective particle image diameter and depth of field.

3.2. Stereoscopic PIV

The above discussion regarding PIV is concerned with the use of a single camera system which cannot cannot measure the out-of-plane component of velocity. Further, if this out-of-plane component is large, it can introduce perspective transformation errors into the measurements of the in-plane components. This problem can be alleviated using a second camera looking at the same field of view. This approach is called stereoscopic PIV. The two cameras measure the projections of in-plane velocity components which are used to determine the “true” velocity components, provided the orientations of the cameras with respect to the measurement plane are known.

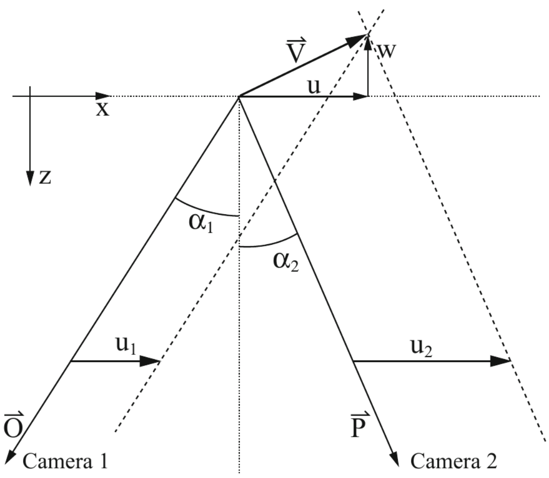

Figure 3.2: Stereoscopic viewing using two cameras (Raffel et al., 2018)

The true velocities are obtained using the measurements made by each camera using the following relations:

$$u = \frac{u_1 \tan\alpha_2 + u_2 \tan\alpha_1}{\tan\alpha_1 + \tan\alpha_2} \tag{3.5a}$$

$$v = \frac{v_1 \tan\beta_2 + v_2 \tan\beta_1}{\tan\beta_1 + \tan\beta_2} \tag{3.5b}$$

$$w = \frac{u_1 - u_2}{\tan\alpha_1 + \tan\alpha_2} = \frac{v_1 - v_2}{\tan\beta_1 + \tan\beta_2} \tag{3.5c}$$

Where α corresponds to the angle made by the out-of-plane axis and the camera line-of-sight when viewed from the top, β corresponds to the angle made by the out-of-plane axis with the camera line-of-sight when viewed from the side and the subscripted velocity components correspond to the first and second camera respectively (Figure 3.2). The out-of-plane velocity component is over-determined which is usually solved using a least-squares approach.

As cameras are placed at an angle with the measurement plane, only a part of the measurement plane will be in focus (Figure 3.3b). The most common method of correcting this is called the angular displacement method where the image plane is titled with respect to the lens plane. The orientation of the image plane is described by the Scheimflug principle which states that the object plane, lens plane and image plane have to intersect at a common point (Figure 3.3a). But, the implementation of this method results in additional perspective distortion and non-uniform magnification across the field of view.

The optimum angular orientation of the cameras with respect to the field of view can be determined using the uncertainties of the in-plane ($\sigma_{\Delta x}$) and out-of-plane ($\sigma_{\Delta z}$) velocity components (Raffel et al., 2018):

$$\sigma_{\Delta z} = \frac{\sigma_{\Delta x}}{\tan\alpha} \tag{3.6}$$

Where α is the angle between the camera line of sight and the normal to the measurement plane (i.e. half of total stereo angle). For smaller angles, the uncertainty of the out-of-plane component

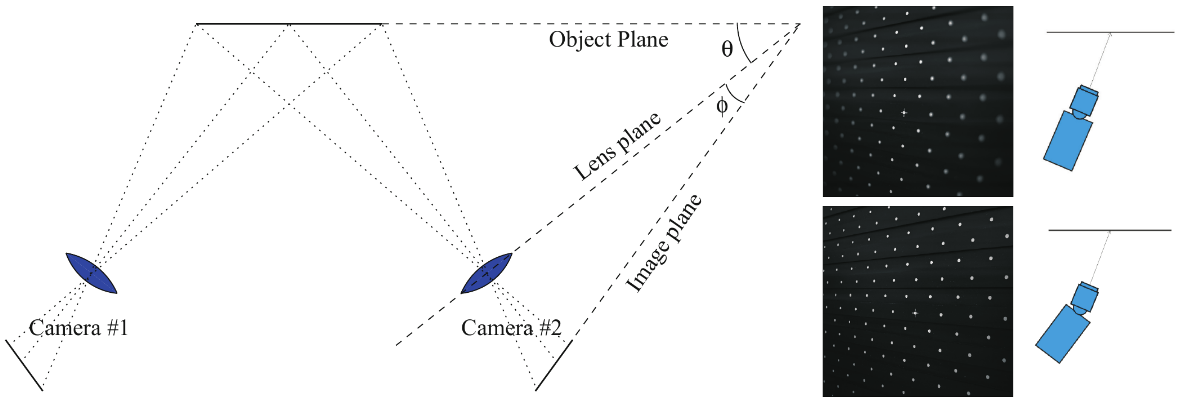

(a) Scheimflug principle (b) Focus of measurement plane

Figure 3.3: Angular displacement method (Raffel et al., 2018)

becomes significantly larger than those of the in-plane components and vice-versa for larger angles. Additionally, perspective error increases at higher angles and hence, $\alpha = 45^\circ$ is often chosen as a optimum as all components have the same uncertainty. In practise however, this is not the optimum value as velocity vectors are computed in a stereo-reconstructed coordinate system that is mapped from raw images, which reduces the pixel resolution for certain components. Further, additional errors are introduced when both cameras do not view the same measurement volume at higher stereo angles. The uncertainties due to these effects are difficult to determine and cannot be generalised. Therefore, stereo angles between 30° and 45° are recommended (Raffel et al., 2018).

3.3. PIV Cross-Correlation

Time-resolved PIV usually follows the principle shown in Figure 3.4, where cross-correlation is performed for consecutive images, resulting in (N-1) velocity fields for every N images. The disadvantage of this method is that when a random image has issues such as poor seeding, bad lighting, strong reflections, strong out-of-plane motion or high turbulence, then that image affects two velocity fields. This introduces more outliers and noise in the velocity fields.

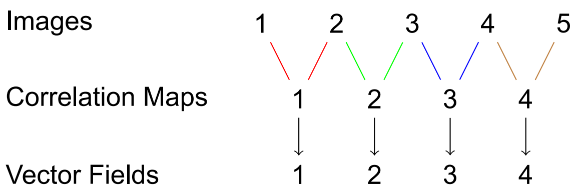

Figure 3.4: Principle of time-resolved cross-correlation

One of the data processing techniques used to improve the stability and accuracy of velocity fields is called the sliding sum of correlation method (Sciacchitano et al., 2012). From each image pair, the algorithm calculates only the correlation map and not the velocity field. A certain number of neighbouring correlation maps are then added with a Gaussian weighting, dampening the effect of correlation maps further away from the image. Finally, a single vector field is computed from the summed-up correlation planes (Figure 3.5). Filter length, L_f determines the number of neighbouring images on either side of a given image considered for summation and time separation, *dt* determines which images are chosen for cross-correlation.

The advantage of this method is that it dampens the effect of bad images and prevents outliers in the velocity field. However, the main disadvantage is that it is computationally more expensive and time consuming that the usual method. Further, less number of velocity fields are obtained compared to the conventional method.

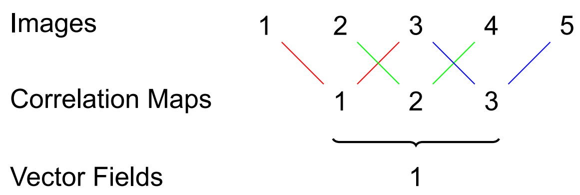

Figure 3.5: Principle of sliding sum of correlation (L_f = 2, *dt* = 2)

3.4. Integral Momentum Analysis

The integral form of the momentum equations can be utilised to obtain aerodynamic forces acting on an object such as a cyclist (Anderson Jr, 2010). Consider a control volume enclosing a stationary cyclist. Applying conservation of momentum over this control volume, the following expression is obtained:

$$\frac{\partial}{\partial t} \oiiint_{\mathcal{V}} \rho \mathbf{V} \, d\mathcal{V} \; + \; \oiint_{S} (\rho \mathbf{V} \cdot \mathbf{dS}) \mathbf{V} \; = \; - \oiint_{S} p \, \mathbf{dS} \; + \; \mathbf{F}_{\text{viscous}} \; - \; \mathbf{F}(t) \tag{3.7}$$

Where $\mathcal{V}$ is the control volume, $\mathbf{V}$ is velocity vector of the fluid, S is the control surface, p is the static pressure of the fluid, $\mathbf{F}_{\text{viscous}}$ is the total viscous force and $\mathbf{F}(t)$ is the instantaneous force vector acting on the fluid due to the cyclist in the control volume. Assuming the control volume is chosen as the stream-tube enclosing the cyclist as shown in Figure 3.6, some simplifications can be made. The first term represents the unsteadiness in the flow due to the pedalling motion of the cyclist legs and rotation of the wheels. Based on the work by Mohebbian and Rival (2012); Rival and Van Oudheusden (2017); Wu et al. (2005), this term can be expanded as follows:

$$\frac{\partial}{\partial t} \oiiint_{\mathcal{V}} \rho \mathbf{V} \, d\mathcal{V} \; = \; \rho \frac{\partial}{\partial t} \oiint_{S} \mathbf{x}(\mathbf{V} \cdot \mathbf{dS}) \; + \; \rho \mathcal{V}_{cyc} \frac{\partial w_{\text{cyc}}}{\partial t} \tag{3.8}$$

Where $\mathbf{x}$ is the coordinate vector, $\mathcal{V}_{cyc}$ is the volume of the cyclist and w_{cyc} is the velocity of the cyclist. As the time derivative of $(\mathbf{V} \cdot \mathbf{dS})$ and the cyclist velocity is small, especially given the small acquisition time (maximum of 1 s), this unsteady term can be neglected (de Martino Norante, 2018; Hirsch, 2018; Spoelstra, 2017). Also, as the control volume is chosen as the streamtube, it is assumed that there is no mass flow across the side surfaces. This means that the viscous force on the side surfaces of the control volume can be neglected (Kurtulus et al., 2007). Further, as this viscous force is relevant only on the surfaces of the cyclist, this force can be completely neglected when the upstream and downstream control surfaces are sufficiently far away from the cyclist (Kurtulus et al., 2007; Mohebbian and Rival, 2012). Moreover, considering the component of the equation acting along the direction of the cyclist, the equation simplifies to:

$$D(t) \; = \; - \oiint_{S} (\rho \mathbf{V} \cdot \mathbf{dS}) \, w \; - \; \oiint_{S} (p \, dS)_z \tag{3.9}$$

Where w is the component of velocity along the direction of the cyclist. Again, as there is no mass flow across the walls of the streamtube, the first term on the right side of the above equation can be simplified as:

$$\oiint_{S} (\rho \mathbf{V} \cdot \mathbf{dS}) \, w \; = \; \rho \left[- \oiint_{S_i} w_{\infty}^2 \, dS_i \; + \; \oiint_{S_o} w_{\text{wake}}^2 \, dS_o \right] \tag{3.10}$$

Where S_i and S_o represent the control surfaces normal to the streamwise direction upstream and downstream of the cyclist respectively, and w_{∞} and w_{wake} represent the streamwise velocity components upstream and downstream of the cyclist respectively. Substituting back into the equation and similarly expanding the pressure term:

$$D(t) = \rho \left[\oiint_{S_i} w_{\infty}^2 \, dS_i \; - \; \oiint_{S_o} w_{\text{wake}}^2 \, dS_o \right] \; + \; \oiint_{S_i} p_{\infty} \, dS_i \; - \; \oiint_{S_o} p_{\text{wake}} \, dS_o \tag{3.11}$$

Here p_∞ and p_{wake} represent the static pressure upstream and downstream of the cyclist respectively. It is to be noted that the above equation is further simplified by Anderson Jr (2010) using the integral equation of mass conservation. However, the same simplification cannot be performed here as the velocity upstream of the cyclist (w_∞) is not uniform, but exhibits spatial variation depending on the on-site wind conditions.

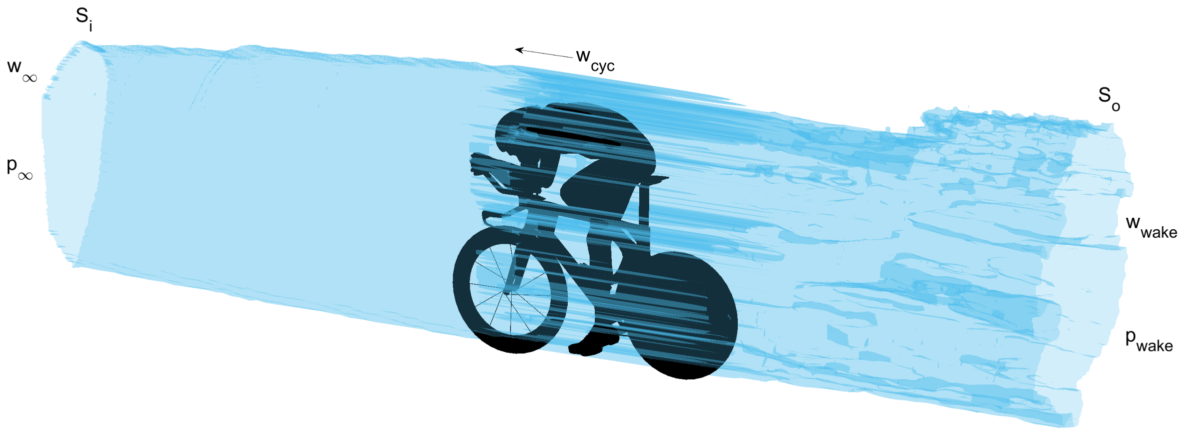

Figure 3.6: Control volume around a cyclist

The discussion till now was concerned with a wind tunnel reference frame where the object is stationary and the fluid is moving. However, in the current experiments, the reference frame is changed such that the cyclist is moving while the fluid remains stationary i.e. the cyclist moves through a fixed plane where measurements are taken at different instances of time. In this reference frame, measurements taken before the passage of the cyclist are considered as upstream measurements and similarly measurements taken after the passage of the cyclist correspond to wake velocity of the cyclist. When the measurements from this reference frame are converted to one where the cyclist is stationary, measurements at different time instants correspond to measurements at different locations in space. The reference frame of the measurements can be converted by subtracting the cyclist velocity (w_{cyc}) from all measured velocities:

$$D(t) = \underbrace{\rho \left[\oiint_{S_i} \left(w_\infty - w_{\text{cyc}}\right)^2 dS_i - \oiint_{S_o} \left(w_{\text{wake}} - w_{\text{cyc}}\right)^2 dS_o \right]}_{\text{Momentum Term}} + \underbrace{\oiint_{S_i} p_\infty dS_i - \oiint_{S_o} p_{\text{wake}} dS_o}_{\text{Pressure Term}} \tag{3.12}$$

This drag force can be normalised by the dynamic pressure to obtain instantaneous drag area:

$$C_D A(t) = \frac{D(t)}{\frac{1}{2}\rho \left(w_\infty - w_{\text{cyc}}\right)^2} \tag{3.13}$$

Thus, it can be seen that a drag area value can be obtained for different wake planes using a common upstream velocity measurement. However, measurements taken at different wake planes from the same cyclist pass are “correlated” to each other and hence do not provide statistical confidence in drag area. Measurements of drag area from multiple passages of the cyclist are not correlated to each other and an ensemble average from multiple passages will provide a statistically converged drag area.

3.4.1. Pressure from PIV

It can be seen from Eqn. 3.12 that pressure measurements are necessary for evaluating drag force. For individual cyclists, the control volume can be chosen such that $p_{\text{wake}} = p_\infty$ and that term can be neglected. This means that the wake measurements have to be taken at a location where the low pressure in the wake has recovered to freestream conditions. de Martino Norante (2018); Terra et al. (2016b) have shown that at distances greater than 3 m in the wake, the contribution of this pressure term is less than 1% and can be neglected.

However, for drafting cyclists with 30 cm wheel gap, the pressure field in-between the two cyclists is not equal to freestream and has to be considered for accurate drag measurements. PIV measurements only provide velocity fields and hence pressure fields have to be reconstructed. One method of determining pressure from velocity fields is by solving the pressure Poisson equation (PPE) (Van Oudheusden, 2013). This equation is obtained by taking the divergence of the momentum conservation equation as follows:

$$\nabla p = -\rho\left(\frac{\partial \mathbf{V}}{\partial t} + (\mathbf{V}\cdot\nabla)\,\mathbf{V}\right) + \mu\nabla^2\mathbf{V} \tag{3.14a}$$

$$\nabla\cdot(\nabla p) = \nabla\cdot\left(-\rho\left(\frac{\partial \mathbf{V}}{\partial t} + (\mathbf{V}\cdot\nabla)\,\mathbf{V}\right) + \mu\nabla^2\mathbf{V}\right) \tag{3.14b}$$

$$\nabla^2 p = -\rho\nabla\cdot(\mathbf{V}\cdot\nabla)\,\mathbf{V} \tag{3.14c}$$

The simplified PPE (Equation 3.14c) is valid for incompressible and divergence free ($\nabla\cdot\mathbf{V} = 0$) velocity fields. It can be seen that the evaluation of the pressure field requires spatial gradients of the velocity field. Although all three components of the velocity field can be obtained from stereoscopic-PIV, spatial gradients can be only be obtained for the in-plane velocity components. The gradients of the out-of-plane velocity components can be estimated by invoking Taylor's frozen turbulence hypothesis (Zaman and Hussain, 1981) which is popularly expressed as:

$$\frac{\partial}{\partial z} = -\frac{1}{U_{\text{conv}}}\frac{\partial}{\partial t} \tag{3.15}$$

Where U_{conv} is the mean convection velocity. However, it is known that the convection velocity of the wake of the cyclists varies both in-plane and out-of-plane (with distance in the wake) (Crouch et al., 2014). Further, the accuracy of this gradient is dependent on the temporal resolution of the velocity field. Therefore, the estimation of this out-of-plane gradient would introduce more error than when neglected. Hence, the in-plane velocity components can be used to obtain planar pressure fields, where the PPE simplifies to:

$$-\frac{1}{\rho}\left(\frac{\partial^2 p}{\partial x^2} + \frac{\partial^2 p}{\partial y^2}\right) = \left(\frac{\partial u}{\partial x}\right)^2 + 2\frac{\partial u}{\partial y}\frac{\partial v}{\partial x} + \left(\frac{\partial v}{\partial y}\right)^2 \tag{3.16}$$

4 Experimental Methodology

This chapter describes the experimental setup and techniques utilised as part of the thesis. The chapter details the reasons behind various choices made during the experiment such as classification of cyclists, tunnel size, PIV imaging details, acquisition details and drafting configurations. Further, certain challenges with regard to the feasibility of the experiments are also discussed. The chapter concludes with the enumerated steps taken to acquire the measurements of this experiment.

Contents

4.1. Cyclists and Track

Three development cyclists from cycling team Sunweb participated in the measurements. The cyclists are initially classified into three categories based on their heights:

Table 4.1: Classification of Cyclists

Classification	Height [m]	Mass [kg]
Small	1.75	61
Medium	1.85	70
Large	1.92	69

All the cyclists were professional cyclists fitted with Sunweb cycling equipment such as Lazer Victor helmet, Sunweb skin suit and Cervelo P5 2019 bicycles. However, it is to be noted that the small cyclist was part of a different cycling team as a short cyclist was not available from team Sunweb. The small cyclist did not use the same equipment as the other cyclists; a time trial helmet with an elongated tail section, different skin suit and custom TT bike. Although there were differences in the equipment between the cyclists, the same equipment was used for both individual and drafting configurations. To ensure safety, the cyclists wore laser goggles under the time trial helmets to avoid damage from the laser light.

The experiments were conducted at the Tom Dumoulin Bike park, Sittard-Geleen, Netherlands. The facility contains numerous courses with different distances, surface types, elevation and corners. The experiment was setup on the outermost track, a 1.125 km long rectangular loop. A schematic of the track layout is shown in Figure 4.1. This track was chosen as it had zero elevation change and the cyclists were able to accelerate on the main straight to reach the required speed. Further, after acquisition the time taken by the cyclists to complete the lap was used to transfer the acquired images from the camera to the computer.

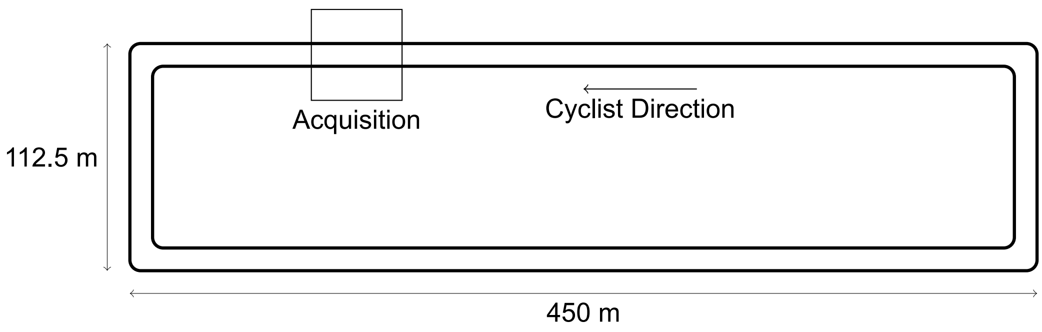

Figure 4.1: Schematic of track in Tom Dumoulin Bike Park

4.2. On-Site Setup

4.2.1. Tunnel

The previous two experiments (de Martino Norante, 2018; Hirsch, 2018) of the Ring of Fire project involved the use of indoor facilities, with a simple tunnel structure using custom poles and panels. As the current experiments involved outdoor track measurements, subject to environmental conditions such as wind and rain, the same tunnel structure could not be used. Further, windy conditions also required easily operable doors to contain the tracer bubbles near the measurement plane. Therefore, a commercial outdoor tent was used for the experiments. The tunnel was 8 m long, 5 m wide and 3 m tall, which was chosen such that aerodynamic blockage and boundary effects are not introduced. Although the total volume of the tunnel was the same as previous experiments by de Martino Norante (2018) and Hirsch (2018), the current tunnel is wider by 1 m and shorter by 2 m in length.

This tunnel structure was built near the end of the main straight of the track (Figure 4.1). The entrance and exit of the tunnel have doors that can be opened and closed using a system of pulleys and ropes (Figure 4.2b). The tunnel was constructed in the middle of the track and the location on the track was chosen such that the truck containing the laser head and control unit could be parked next to the tunnel (Figure 4.2a).

(a) Closed tunnel (b) Open tunnel

Figure 4.2: Tunnel structure

4.2.2. Laser Illumination

The laser head was placed outside the tunnel and a thin slit was made on the side wall of the tunnel so that laser light could enter the tunnel. This slit was made at the midpoint between the tunnel entrance and exit. The Nd:YLF diode pumped Quantronix Darwin-Duo was used to produce laser light with a wavelength of 527 nm with a pulse energy of 25 mJ at a repetition rate of 1 kHz.

The laser head was placed at a height of 0.5 m from the ground using the hydraulic bed of the truck, which was located 5 m from the side of the tunnel. The laser beam was expanded through a series of lenses to produce a laser sheet. First, the laser beam was expanded with a diverging spherical lens of focal length, f = -50 mm and next a converging cylindrical lens of focal length, f = 60 mm was used to restrict expansion in the horizontal direction. A strong diverging cylindrical lens of focal length, f = -100 mm was used at the end to expand the beam in the vertical direction.

The laser head was covered with safety screens to avoid direct visual contact with the laser source. The laser sheet covered the entire width of the tunnel forming a trapezoidal shape with 2 m height on the near side and 3 m height on the far side. The laser sheet thickness varied from 4 cm to 6.5 cm across the tunnel width with an average of 5.25 cm at the centre. The thickness of the laser sheet was chosen as four times the maximum out-of-plane displacement between consecutive images. This maximum displacement is calculated by using the maximum convection velocity of the particles (0.61 times the cyclist velocity (Crouch et al., 2014)) and acquisition frequency.

4.2.3. Seeding System

Helium Filled Soap Bubbles (HFSB) were used as tracer particles for their neutral buoyancy and light scattering capabilities. The bubble production was managed by the Fluid Supply Unit (FSU), which adjusted pressures for helium, air and soap. An electrically operated mobile air compressor unit supplied pressured air to the FSU while a pressurised helium tank supplied helium and a reservoir inside the FSU stored the soap solution. LaVision Bubble Fluid Solution (BFS), containing water, glycerine and soap was used as the soap solution.

The output of the FSU tubes were connected to the seeding rake placed inside the tunnel. The seeding rake consisted of a 2D array of 200 nozzles placed on the trailing edge of 10 wings (Figure 4.3b). The seeding rake at full operating condition produces 60000 bubbles per second with an average bubble diameter of 400 μm. Leakage of soap solution by the seeding rake was collected by a large tray placed underneath the rake, so that the cycling track would not become slippery. The seeding rake location was decided by assessing seeding distribution and wind conditions before each cyclist passage. At low wind conditions, the seeding rake was placed downstream of the laser sheet so that the bubbles would convect with the cyclist and at high head wind conditions, it was placed upstream of the laser sheet so that head wind would ensure bubbles stay near the measurement plane.

(a) Camera placement

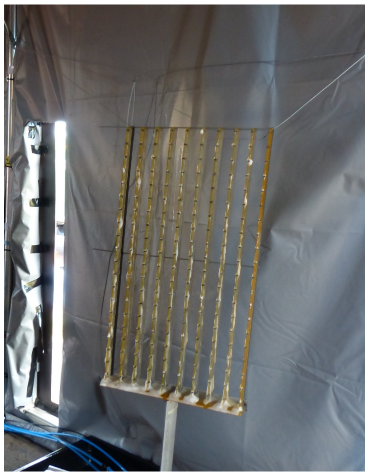

(b) Seeding rake

Figure 4.3: Experimental Setup

4.2.4. Imaging System

Two high-speed Photron FASTCAM SA 1.1 cameras were used to capture the images. The cameras have a 12-bit CMOS sensor with a pixel size of 20 μm and a resolution of 1024 $\times$ 1024 with a maximum acquisition frequency of 5.4 kHz at full resolution. The cameras have a built-in memory of 8 GB corresponding to a maximum storage of 5457 images. Nikon lens of 35 mm focal length were used along with Scheimflug adapters to ensure the entire measurement plane was in focus. The low focal length lens was used as the cameras were placed very close to the measurement plane compared to previous experiments. Bandpass filters were used to filter out unwanted light sources such as reflections and noise.

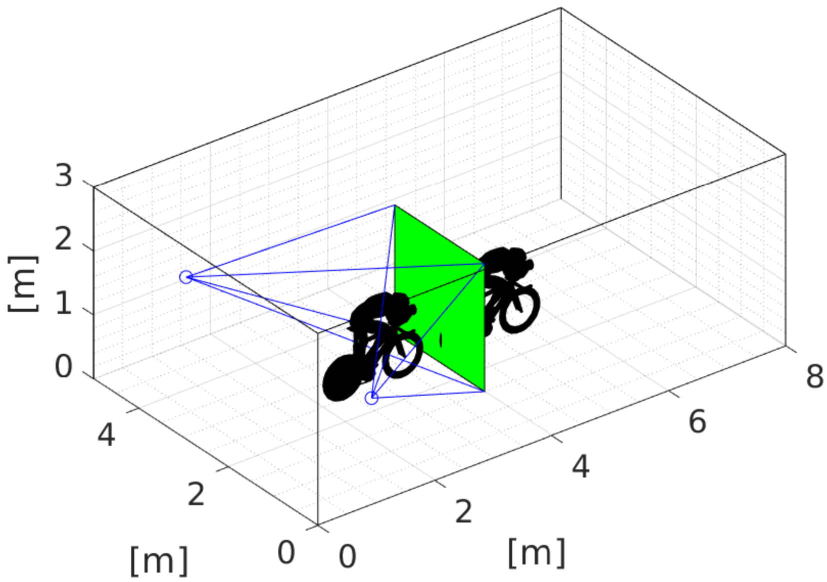

Figure 4.4: Visualisation of Setup (blue circles are cameras)

In order to determine the location of the two cameras, a simple calculation was performed to find an optimum between stereo angle, required field-of-view and sufficient overlap in the field-of-view of each camera. For drafting distances of 30 cm (inter-wheel gap) between the two cyclists, the presence of the second/trailing cyclist would block the optical access to the measurement plane. Therefore, an analysis was conducted in MATLAB (Figure 4.4) to determine the position and angle of the cameras such that velocity fields could be measured in-between two drafting cyclists.

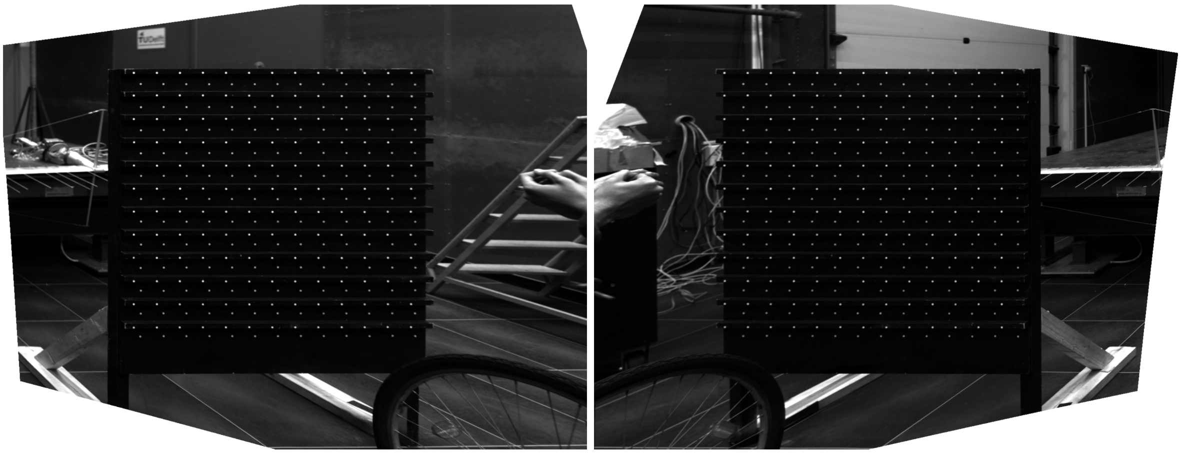

(a) Left Camera View (b) Right Camera View

Figure 4.5: Stereo Reconstructed Images

To validate the MATLAB calculations, the setup of the cameras was simulated at the Open Jet Facility of the aerospace engineering faculty. Different camera locations was tested along with a static cyclist for different drafting distances. The calibration plate was used as reference to qualitatively determine the overlap between the field-of-view of the cameras. It was observed that for a lateral spacing of 5 m between the cameras and for a drafting distance of 30 cm, the wake of the first cyclist would be captured completely with minimal interference from the second cyclist, which mostly affected the sides of the field-of-view (Figure 4.5).

The cameras were placed at a height of 1.35 m from the ground using traversing tripods (Figure 4.3a) and 2.75 m from the measurement plane towards the tunnel entrance (Figure 4.6). The cameras were placed close to tunnel side walls resulting in a lateral distance of 4.35 m between them. This resulted in a field of view of 2 m $\times$ 1.8 m with a resolution of 0.57 pixel/mm and a magnification of 0.01. This placement of the cameras resulted in a total stereo angle of $2\alpha \approxeq 98^{\circ}$.

Based on the above configuration, the lower limit of f-stop ($f_{\#}$) was calculated to be 1.45 using focal depth equal to laser sheet thickness (Eqn. 3.4). Thus, an f-stop of f/2.8 was used to allow enough light to enter and also capture the depth of field i.e. laser sheet thickness. It is to be noted that due to the large pixel size of the sensor, the effective image diameter of the particles was found to be smaller than one pixel, which introduced peak locking errors.

4.2.5. Acquisition System

Synchronisation between cameras and laser was enabled through the LaVision High Speed Controller (i.e. Programmable Timing Unit) and a network switch. Acquisition was performed using a Windows desktop computer with LaVision DaVis 8.4. A portable digital weather station was used to record environmental parameters such as air temperature, pressure and humidity. As these systems were placed outside the tunnel structure, they had to be covered with plastic screens and covers to protect the electronics from frequent rain.

4.3. Acquisition Procedure and Implementation

All measurements were conducted for a cyclist velocity of 13.3 m/s and for drafting configurations, the cyclists were asked to maintain a distance of 30 cm between the rear wheel of the leading cyclist and the front wheel of the trailing cyclist. The choice of acquisition frequency and number of images

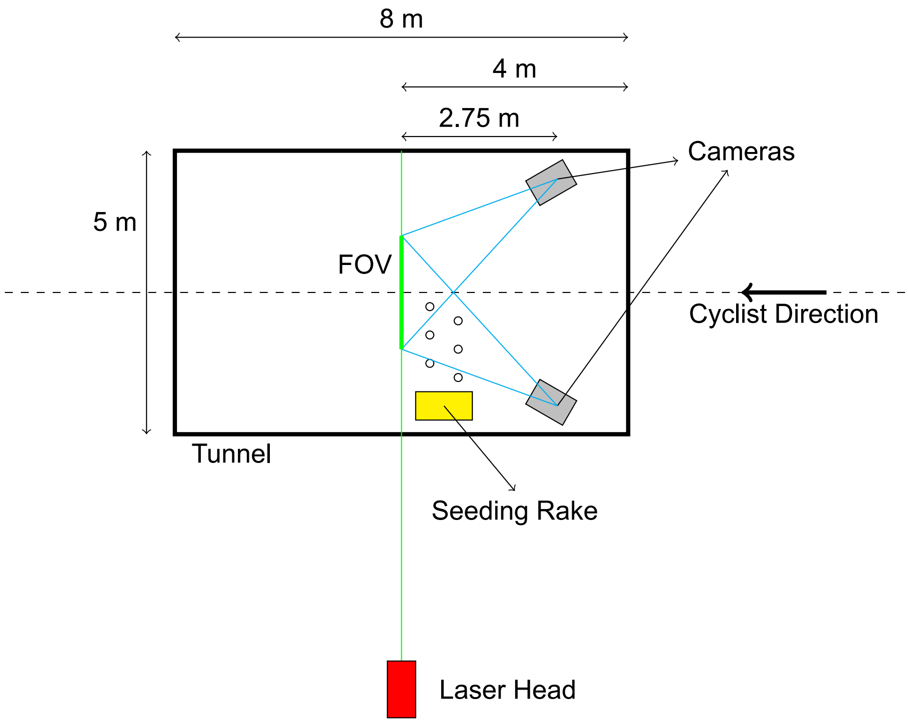

Figure 4.6: Schematic of setup inside tunnel (Top View)

to be captured was dependent on time taken to transfer images from the cameras to the computer and time taken by the cyclists to complete the rest of the track. Acquisition frequency and number of images acquired also affects size of the measured control volume i.e. distance captured upstream and downstream of the cyclist.

Table 4.2: Acquisition Details

Configuration	**Acquisition Frequency [Hz]**	**Number of Images per Camera**	**Distance Upstream of Cyclist [m]**	**Distance Downstream of Cyclist [m]**
Individual	500	1000	4	20
Drafting	1000	1100	4	7

The details of the acquisition are shown in Table 4.2 for both individual and drafting configurations. An acquisition frequency of 1 kHz was chosen for the drafting case to capture large number of images in-between the two cyclists. The images captured in-front of the cyclist should not be affected by upstream propagation and enough images have to be captured in the wake such that convergence is achieved with respect to drag area. Based on the work carried out by previous Ring of Fire experiments (de Martino Norante, 2018; Hirsch, 2018; Spoelstra, 2017), 4 m upstream and 7 m in the wake was chosen, resulting in 1100 images per camera in total (Figure 4.7). However, for the individual case, a lower frequency was chosen to acquire larger distance in the wake.

Calibration was performed at the start of each testing day with the large calibration plate shown in Figure 4.5. The square wooden plate has dimensions of 1.2 m × 1.2 m × 0.04 m with a staggered grids of dots. White circular stickers of 8 mm diameter were used as dots, placed at equal intervals forming a grid of 312 dots with a spacing of 90 mm. One set of grids are offset by 20 mm in the out-of-plane direction. The calibration plate is placed at the centre of the tunnel, aligned perpendicular to the cyclist direction and coinciding with laser sheet. Calibration was performed using the pinhole fit model and stereoscopic self-calibration was also performed starting with a window size of 64 pixels and 50% overlap and ending with a window size of 32 pixels and 75% over four passes (Wieneke,

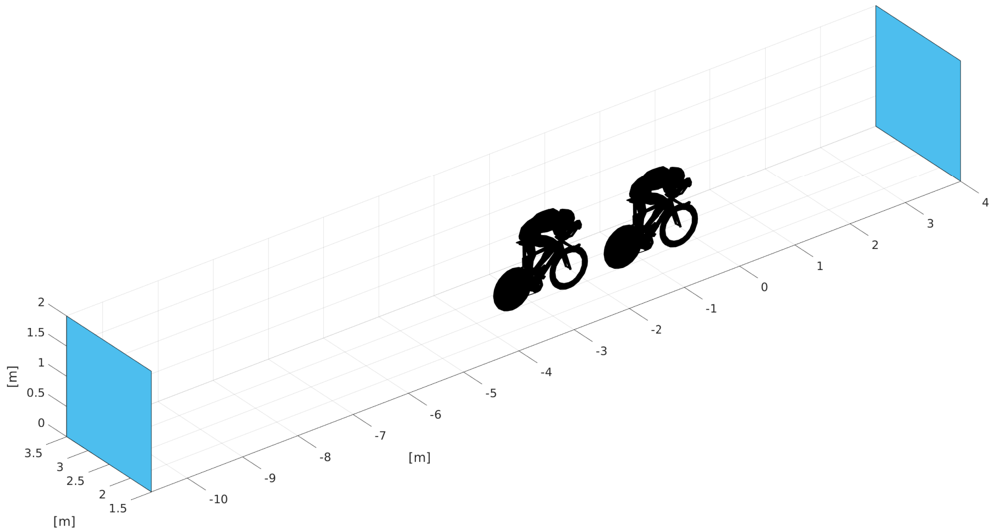

Figure 4.7: Visualisation of first and last image captured during drafting

2005). The final RMS-of-fit was found to be 0.57 pixel. Intensity calibration was also performed before the measurements using the lens caps.

A 20 kVA diesel generator was rented to supply power for the laser, computer systems, air compressor and other electronics. The procedure for acquisition required a series of steps to be followed in sequence to capture images with the optimum amount of seeding, illumination and distance in the wake:

1. The air compressor was switched on first and made to run till its reservoir was full. Both doors of the tunnel were closed at this point.
2. The inlet valve of air to the FSU was switched on along with the valves for helium and soap. The pressure for the helium and soap was set to 2 bar. This ensured continuous production of bubbles.
3. Seeding concentration and uniformity was checked in DaVis live mode. Acquisition frequency, camera exposure time and number of images were set along with the data set name.
4. Signal was given to the cyclists at the end of the straight to start riding.
5. When cyclists were 20 m away from tunnel, signal was given to open both doors of the tunnel.
6. When cyclists were 5 m away from tunnel, acquisition was triggered to acquire the full capacity of camera i.e. 5457 images.
7. The doors were held open till end of the acquisition and closed only after the laser light switches off. The valves for helium, soap and air were then switched off at the FSU. This was done to ensure the air pressure in the reservoir was not completely depleted.
8. Although 5457 images are captured, only the required images are saved e.g. 400 images upstream of the cyclists and 570 images in the wake for the drafting case. Saving of the images from the cameras to the computer usually took around 2 min.
9. During the transfer time, the cyclists looped back to the starting position while environmental conditions, data set details and description was recorded in the acquisition computer.

This is repeated 10 times for each case to achieve statistical convergence. Minimum of four people were required to perform this experiment; the cyclist, one person at the front tunnel door, one at the rear tunnel door and one person at the computer to trigger acquisition.

Four different configurations of two cyclist drafting were performed namely: Large - Small (L - S), Small - Large (S - L), Medium - Small (M - S) and Large - Medium (L - M), corresponding to the leading and trailing cyclist respectively. These configurations were chosen for the following reasons:

- L - S: Effect of a large leading cyclist on a small trailing cyclist. The trailing cyclist should experience the highest aerodynamic benefit compared to other configurations.
- S - L: Effect of small leading cyclist on a large trailing cyclist. The trailing cyclist should experience the lowest aerodynamic benefit compared to other configurations.
- M - S: Compared with L - S to determine the effect of replacing large leading cyclist with medium cyclist.
- L - M: Compared with L - S to determine the effect of replacing small trailing cyclist with medium cyclist.

5 Data Reduction and Analysis

The various data processing techniques adopted to extract useful information from the experimental measurements are discussed in the current chapter. The various topics addressed include determination of cyclist velocity, drafting distance, PIV data processing, velocity and pressure field manipulation. The chapter details the procedure employed to analyse the data and discusses the accuracy and uncertainty of the procedure. Although Ring of Fire data processing techniques were established by previous research campaigns, modifications, improvements and new data processing challenges due to drafting cyclists are addressed.

Contents

5.1. Cyclist Velocity

The cyclist velocity was measured using the images of the high-speed PIV cameras. The procedure is discussed below:

1. The distance between the front wheel and the rear wheel of the bicycle was chosen as the reference length and was measured for all the cyclists.
2. The image number corresponding to the tip of the front wheel touching the back plane of the laser sheet was noted (Figure 5.1a).
3. The image number corresponding to the tip of the rear wheel exiting the back plane of the laser sheet was noted (Figure 5.1b).
4. Using the acquisition frequency and the difference in image numbers, the time elapsed between the two images was determined.
5. Finally the velocity was determined using the reference length and time elapsed (Eqn. 5.1).

(a) Image #345 (b) Image #409

Figure 5.1: Example of images used for velocity calculation

$$w_{\text{cyc}} = \frac{L_{\text{ref}}}{\left(\dfrac{\Delta N}{f_{\text{acq}}}\right)} = \frac{1.695}{\left(\dfrac{409 - 345}{500}\right)} = 13.242 \text{ m/s} \tag{5.1}$$

This method provided one velocity value for each cyclist passage. It was assumed that the cyclist velocity during the acquisition time (2 s for individual and 1.1 s for drafting case) remained constant. Perspective errors can introduce uncertainty in this measurement procedure, causing misidentification of image numbers. The maximum uncertainty introduced due to this misidentification was found to be 1.6% and 0.8% for individual and drafting cases respectively. This uncertainty was reduced in the drafting case as the acquisition frequency was higher. The choice of using the back plane of laser sheet as reference was arbitrary and the front plane of the laser sheet could be chosen as well. Although the individual image numbers will differ when the front plane is chosen, the difference in image numbers would be same in both cases. However, it is to be noted that the identification of image numbers introduced some subjectivity, as the exact moment of the wheel touching/leaving the laser plane cannot be found and hence the choice of the image number was left to the judgement of the author.

5.2. Drafting Distance

Drafting distance in the current project was defined as the distance between the rear wheel of the leading cyclist to the front wheel of the trailing cyclist (i.e. inter-wheel gap). As this distance varied both longitudinally and laterally with respect to the cyclist direction, these were measured separately.

5.2.1. Longitudinal Distance

The longitudinal drafting distance was measured in a similar manner to the cyclist velocity as follows:

$$z = \overline{w_{\text{cyc}}} \frac{\Delta N}{f_{\text{acq}}} \tag{5.2}$$

Where $\overline{w_{\text{cyc}}}$ is the average velocity of the two cyclists, ΔN corresponds to the difference in image numbers between the two drafting cyclists and f_{acq} is the acquisition frequency. The uncertainty in longitudinal drafting distance due to misidentification of image numbers was found to be 2.3% on average.

5.2.2. Lateral Distance

The lateral drafting distance was determined by performing stereo-reconstruction of the images where the rear wheel of the leading and trailing cyclists' left the laser sheet (Figure 5.2). The x-coordinate was then measured in each image and the difference was used as the lateral drafting distance. For the example shown below, the lateral drafting distance corresponded to 0.12 m. This method assumed that both cyclists were travelling in a straight line. The accuracy of this method was dependent on the perspective errors introduced due to stereo-reconstruction as well as the ability to determine the exact location of the rear wheel. The uncertainty due to this location determination was proportional to the size of the reflection made by the tip of the rear wheel. The smaller the reflection, the more accurately the distance can be determined. Again, this uncertainty can be reduced by increasing the acquisition frequency.

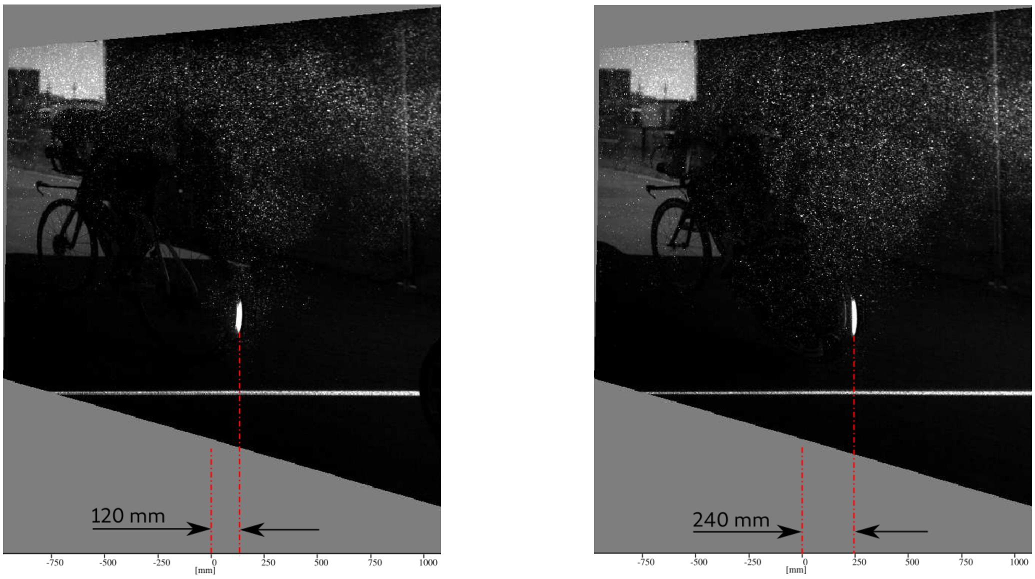

(a) First cyclist leaving the laser sheet

(b) Second cyclist leaving the laser sheet

Figure 5.2: Calculation of lateral drafting distance from stereo-reconstructed images

5.3. PIV Data Processing

The methodology of processing raw PIV images and obtaining velocity fields involved a number of steps and choices that affected the accuracy and uncertainty of the final result. These steps and choices are discussed and justified in the following sections.

5.3.1. Image Pre-Processing

Before performing PIV cross-correlation of the images, image processing steps were performed to remove unwanted reflections, glares, background noise and improve signal-to-noise ratio of particle intensities. For each run, after the cyclist was sufficiently far away from the measurement plane and no longer in the field of view, the minimum intensity in each pixel was calculated among the rest of the images in the acquisition. This was used as a “background” image and was subtracted from all the images in the acquisition. Further, a sliding minimum subtraction was performed for a window size of 3 px $\times$ 3 px. This window size was chosen after comparing different window sizes as shown in Figure 5.3. The smallest window size removed most of the background compared to the other cases. This can be observed especially with the high intensity background in the top left corner and the cyclist body. Window sizes smaller than 3 pixels tended to remove particle intensities and hence window size of 3 pixels was chosen as the optimum. Figure 5.4 compares the raw images with the final processed image and it can be seen that most of the high intensity glares, reflections and saturated regions were removed in the final image.

(a) 10 px $\times$ 10 px (b) 5 px $\times$ 5 px (c) 3 px $\times$ 3 px

Figure 5.3: Comparison of window size for sliding minimum subtraction

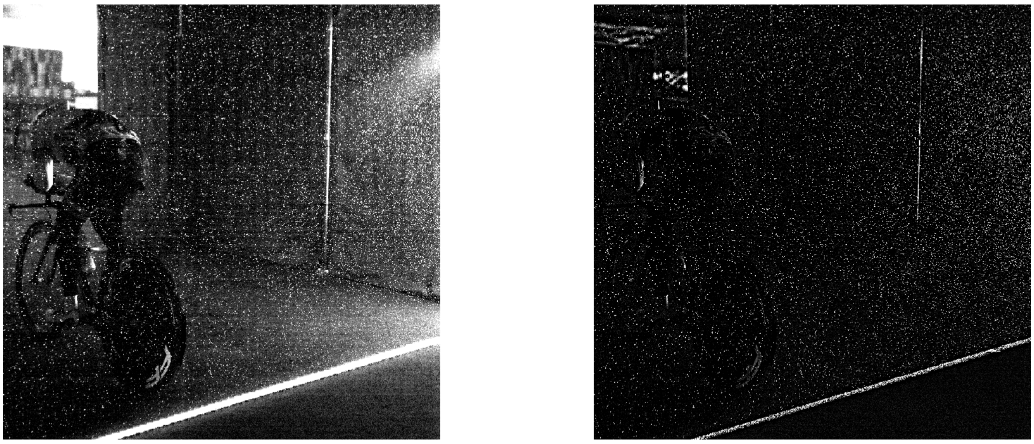

(a) Raw image (b) Final processed image

Figure 5.4: Image pre-processing

5.3.2. Vector Processing

For improved stability and accuracy, the sliding sum of correlation approach (Section 3.3) was utilised for processing PIV images. The details of the processing parameters chosen are shown in Table 5.1. The choice of filter length, time separation and interrogation window size was determined by qualitative and quantitative analysis of the velocity fields and drag area respectively. This analysis showed that higher values of filter length showed smoother variation of the drag area (Figure 5.5a). However, higher filter length values were more computationally expensive and took longer to process the same number of images. Hence, a compromise between stability and computational time was made and a filter length of 2 was chosen. Higher values of time separation introduced “unphysical” noise in the velocity field of the near wake and hence *dt* = 1 was chosen.

Table 5.1: Vector Processing Parameters

Parameter	Value
Filter Length, L_f	2
Time Separation, *dt*	1
Initial Window Size	$2 \times (64 \times 64)$
Final Window Size	$3 \times (24 \times 24)$
Window Shape	Round (1:1)
Overlap	75 %

The resolution of the vector field was iteratively refined with a decreasing multi-pass approach with an initial window size of 64 pixels reducing to 24 pixels. The final window size was chosen based on seeding concentration (approximately 15 particle images in one window), signal-to-noise ratio of the vector fields, amount of fluctuations in drag area (Figure 5.5b) and computation time.

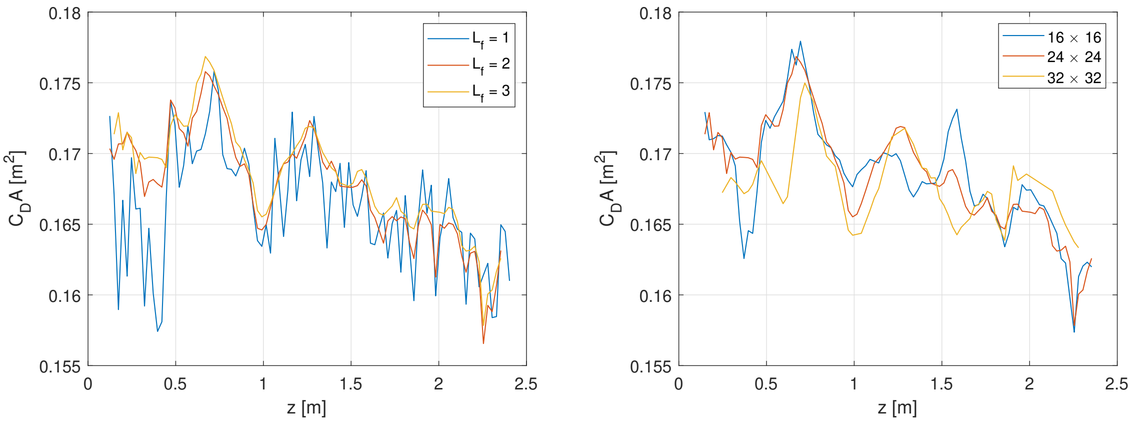

(a) Effect of filter length

(b) Effect of interrogation window size

Figure 5.5: Effect of processing settings on drag variation

Multiple passes of the initial and final window size was performed to obtain convergence of the vector field. The round shape with Gaussian weighting was chosen to ensure particle displacements were not biased towards any one direction while giving higher weighting for particle displacements at the centre of the interrogation window (Wieneke[1] and Pfeiffer[1], 2010). The multi-pass operation was performed with an overlap of 75% to improve the spatial resolution of the vector field for the given seeding density. Post-processing of the vector field was performed using universal outlier detection (Westerweel and Scarano, 2005) using a filter region of 5×5 windows. Vectors were removed when the median residual was greater than three standard deviations. Empty regions in the vector field were interpolated but smoothing/de-noising operations were not performed. Finally, the resulting vector field was cropped, resulting a field of view of 1.5 m $\times$ 1.6 m. The dynamic spatial resolution (DSR) in the horizontal and vertical direction was determined using the final interrogation window size of 24 pixels and the digital image resolution of 0.57 px/mm as follows:

$$\text{DSR}_h = \frac{1500 \times 0.57}{24} = 35.625 \tag{5.3a}$$

$$\text{DSR}_v = \frac{1600 \times 0.57}{24} = 38 \tag{5.3b}$$

Similarly the dynamic velocity range (DVR) was determined using the maximum measured velocity and one standard deviation of the freestream velocity from an ensemble averaged velocity field as follows:

$$\text{DVR} = \frac{12.43}{0.10} = 124.3 \tag{5.4}$$

It was observed that even after performing vector post-processing steps, the velocity fields had spurious data due to strong reflections from the cyclists' clothing and equipment (Figure 5.6a). These strong reflections were falsely recognised as particles and resulted in "unphysical" wake velocities. This strong reflection was usually picked up by the right camera as it captured forward light scattering. The velocity magnitude of this reflection is of the same order as the wake and is usually attached to the main wake region as shown in Figure 5.6b encircled in black. Therefore, this data cannot be corrected by the usually data filtering techniques and hence, velocity fields affected by this reflection is identified manually for each cyclist passage and removed from for all future calculations. The amount of velocity fields removed are predominantly in the near wake i.e. the first few images where the cyclist can still seen in the middle of the measurement plane. This spurious data can be avoided if the cyclists' clothing equipment are dark in colour, as then it can be removed using the image pre-processing steps.

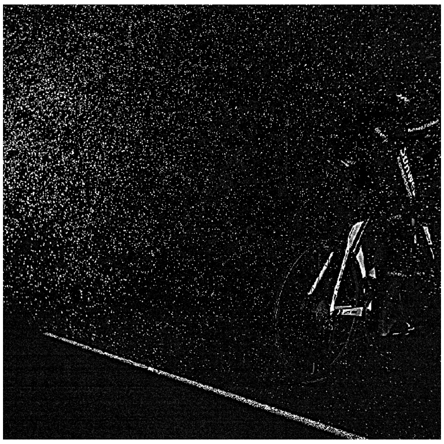

(a) PIV Image after image processing

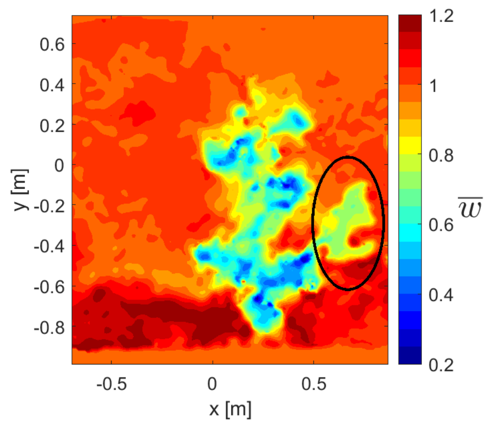

(b) Affected wake velocity field

Figure 5.6: Effect of strong reflections on velocity field

5.4. Wake Contouring

It was observed that the wake velocity fields were dominated by the wake of the cyclist and the freestream region outside the wake had fluctuations in velocity up to 15% of the cyclist velocity. These fluctuations were caused due to variations in outdoor environmental conditions. In order to remove these unwanted freestream fluctuations in wind, a "contour" of the cyclist wake had to be drawn such that velocity outside the contour was discarded, without altering the velocity inside the contour. This procedure is referred to as wake contouring. This procedure was performed using an algorithm in MATLAB which worked in the following manner:

1. A cut-off velocity (Λ) which defined the boundary of the cyclist wake was specified as the input to the algorithm.

2. The algorithm drew an isoline corresponding to the specified cut-off velocity.

3. The coordinates of this isoline were extracted using in-built MATLAB functions.

4. A matrix was constructed which contains '1's inside the isoline and '0's outside the isoline. The size of this matrix corresponded to the size of the specified wake velocity field.

5. This matrix served as the control surface such that when multiplied element-by-element to the wake velocity matrix, values outside the contour became zero while values inside the contour remained as is.

The MATLAB script is provided in Appendix A for further reference. The size of the resulting "contour" from this algorithm and consequently drag area were dependent on the specified cut-off velocity. Hence, it was important to choose the correct cut-off velocity to obtain accurate and repeatable drag measurements.

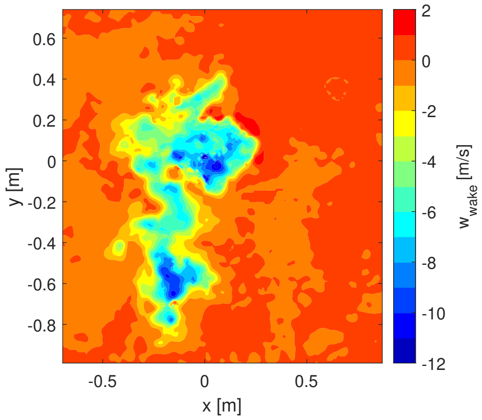

(a) Typical velocity field from Ring of Fire

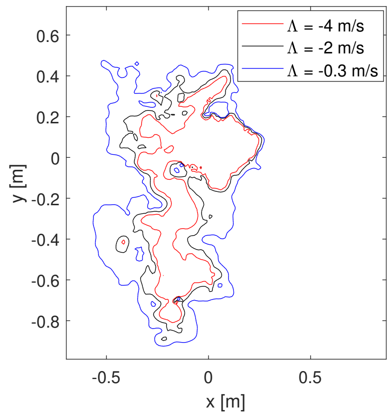

(b) Comparison of different cut-off velocities

Figure 5.7: Selection of cut-off velocity

The measured wake velocity was largely out-of-plane, going into the plane and negative in sign (Figure 5.7a). The core region of the cyclist wake was dominated by large velocity magnitudes (of the order of cyclist velocity). This high velocity magnitude decreased moving away from the core and eventually the sign of the velocity magnitude changed outside the cyclist wake region. This meant that the velocity would be zero at the boundary. However, a cut-off velocity of zero cannot be chosen as the boundary created using this velocity was not a well-defined region for most cases. Hence, the cut-off velocity should be as close to zero as possible while still maintaining a coherent wake contour (Figure 5.7b).

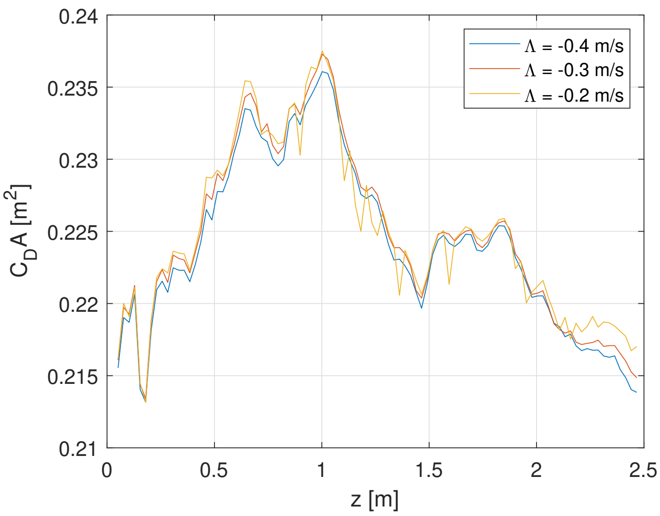

Figure 5.8: Effect of cut-off velocity on drag variation

Figure 5.8 shows the effect of cut-off velocity on the variation of drag area. It can be seen that cut-off velocities of -0.4 m/s and -0.3 m/s showed relatively smooth variations and agreed with each other, but cut-off velocity of -0.2 m/s showed fluctuations as the wake contour was not well-defined for that case. Further, the RMS difference between the curves of -0.4 m/s and -0.3 m/s was found to be 7×10^{-4}, corresponding to 0.3% of the mean drag area. Essentially, the effect of cut-off velocity decreased as the value reached closer to zero.

The choice of cut-off velocity was also dependent on the freestream wind conditions. Head wind in some data sets resulted in strong shear between the cyclist wake and freestream. In such cases, a cut-off velocity of zero can be chosen. Whereas data sets with tail wind made it difficult to identify the exact boundary of the cyclist wake and a cut-off velocity of zero will not work. Hence, to remain consistent among different data sets, a cut-off velocity of -0.3 m/s was chosen for all data sets. Figure 5.9 shows an example of the velocity field after the contouring procedure with a cut-off velocity of -0.3 m/s.

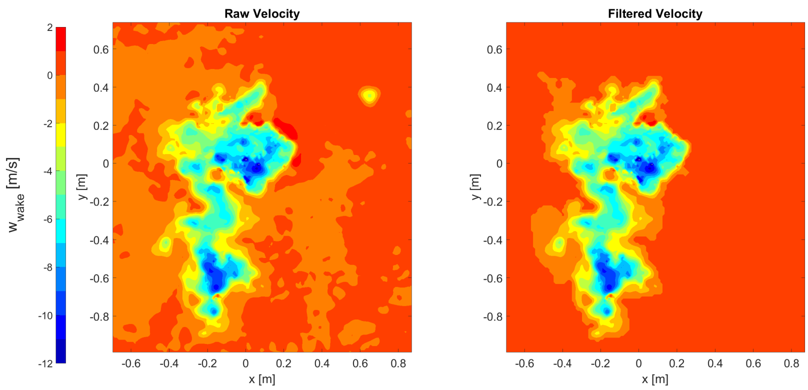

Figure 5.9: Comparison of raw velocity field and velocity field after contouring

5.4.1. Drafting Cyclists

In addition to the above discussed method, the drafting configurations required an additional "filtering" step. As discussed in Section 4.2.1, the presence of the trailing cyclist blocked optical access of the PIV cameras. This blockage could not be removed in the PIV data processing steps and hence the resulting velocity fields were characterised by this optical blockage. Figure 5.10a shows an example of such optical blockage, where regions resembling the cyclist were observed near the sides of the velocity field.

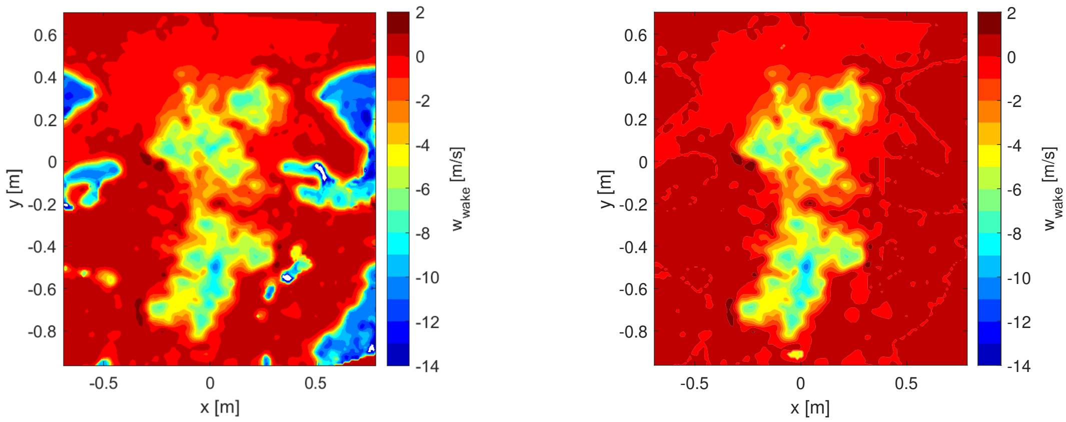

(a) Interference of trailing cyclist

(b) "Filtered" velocity field

Figure 5.10: Removal of false data from velocity fields in-between cyclists

This false velocity data had to be corrected as it was used for pressure reconstruction and also for upstream momentum integration. These false data was first identified and replaced by a moving median interpolation of the neighbouring data points. Care was taken to ensure that the wake region in the middle of the field was not affected by this interpolation. The resulting velocity field was free of this false data as shown in Figure 5.10b.

5.5. Contour Projection and Continuity

The calculation of drag area requires the integration of upstream and wake velocities over control surfaces (Equation 3.12). The assumption made in the integral momentum approach was that the control volume was assumed to be the streamtube enclosing the cyclist. Subsequently, the control surfaces are “slices” of the streamtube at different streamwise locations. As the streamtube expands from upstream to downstream of the cyclist (Figure 3.6), the upstream control surface has to be smaller than the downstream control surface. Thus the upstream and downstream control surfaces cannot be chosen as the entire measured field of view, but have to be chosen such that streamwise mass flow is conserved. The discussion in the previous section describes the methodology used to obtain the control surface for the wake velocity field. The determination of the upstream contour begins with this wake contour. It is assumed that the upstream contour is a scaled down version of the first contour in the wake velocity field. This procedure is called contour projection and was performed using the following algorithm in MATLAB:

1. The contour of the first velocity field in the wake of the cyclist was chosen for scaling. The first wake contour was chosen as this closely resembled the shape of the cyclist. Wake contours further downstream were usually deformed due to wake expansion, lateral movement of the wake and windy conditions.
2. Before scaling, this contour shape was simplified into a polygon to parametrise the shape. Now, the shape could be scaled up and down using a single scaling factor, c.
3. The shape has to be scaled such that the mass flow rate through the upstream contour and wake contour is equal to each other. The right scaling factor was determined based on the residual in mass flow rate defined as follows:

$$R = \dot{m}_i - \dot{m}_o = \oiint_{S_i} \rho \left(w_\infty - w_{\text{cyc}}\right) dS_i \; - \; \oiint_{S_o} \rho \left(w_{\text{wake}} - w_{\text{cyc}}\right) dS_o \tag{5.5}$$

   As the wake control surface (S_o) was already determined and the upstream control surface (S_i) was a scaled version of the wake control surface, the residual was ultimately a function of the scaling factor.

$$R = f(c) \tag{5.6}$$

   The procedure of finding the right scaling factor corresponded to a root-finding problem where an appropriate “root” (i.e. c) had to be determined such that the residual in mass flow rate was zero.
4. A numerical root-finding algorithm called the bisection method was utilised which worked as follows:
   (a) An interval [a b] was guessed such that f(a) and f(b) had opposite signs. This meant that the at least one root existed inside this interval.
   (b) The residual was evaluated at the midpoint of the interval, c = (a + b)/2 and the sign of f(c) was checked with f(a) and f(b). A new sub-interval was chosen such that the new limits again had opposite signs e.g. [a c] or [c b].
   (c) As the root again exists in this new sub-interval, the above step was repeated until the midpoint became the root and the residual became zero.
5. Once the appropriate scaling factor was determined using the bisection method, the first wake contour shape was scaled and the upstream contour matrix was constructed using that scaled shape.

As the above algorithm was executed in MATLAB, the residual did not reach absolute zero and hence, convergence was defined using a tolerance on the residual or when a specified number of iterations was exceeded. The bisection method is a simple and robust method which has a linear convergence rate. Although other faster root-finding methods exist such as secant method and inverse interpolation, it was observed that the bisection method found the root within 15 iterations and was not computationally expensive. Further, the other non-bracketed methods may not converge to the root if certain conditions aren't met, whereas the bisection method found a root for all cases. A more detailed working principle along with the flow chart of the algorithm is provided in Appendix B for further reference.

5.6. Pressure Poisson Equation

In order to determine accurate drag measurements, pressure fields have to be reconstructed from PIV measurements. Pressure fields were determined using the pressure Poisson equation as discussed in Section 3.4.1. The equation was re-written as follows:

$$
\begin{aligned}
\frac{\partial^2 p}{\partial x^2} + \frac{\partial^2 p}{\partial y^2} &= \frac{\partial}{\partial x}\left(\frac{\partial p}{\partial x}\right) + \frac{\partial}{\partial y}\left(\frac{\partial p}{\partial y}\right) \\
&= \frac{\partial}{\partial x}\left[-\rho\left(u\frac{\partial u}{\partial x} + v\frac{\partial u}{\partial y}\right) + \mu\left(\frac{\partial^2 u}{\partial x^2} + \frac{\partial^2 u}{\partial y^2}\right)\right] \\
&+ \frac{\partial}{\partial y}\left[-\rho\left(u\frac{\partial v}{\partial x} + v\frac{\partial v}{\partial y}\right) + \mu\left(\frac{\partial^2 v}{\partial x^2} + \frac{\partial^2 v}{\partial y^2}\right)\right] \qquad (5.7a)
\end{aligned}
$$

$$\Rightarrow Ap = b \qquad (5.7b)$$

For discrete velocity measurements, Equation 5.7a becomes a system of linear equations represented by Equation 5.7b. The two-dimensional laplacian operator was discretised using the second order five-point finite difference method as follows:

$$\Delta p = \frac{p(i-1,j) + p(i+1,j) + p(i,j-1) + p(i,j+1) - 4p(i,j)}{h^2} \qquad (5.8)$$

Where (i, j) represents the indices in the x and y directions respectively and h represents the grid spacing of the measurement field. Neumann boundary condition was applied on all four sides of the 2D grid.

$$\frac{\partial p}{\partial \mathbf{n}} = 0 \qquad (5.9)$$

Where $\mathbf{n}$ denotes the normal vector to the boundary. The RHS of the equation was evaluated using the second order central difference scheme. The system of equations were solved directly by inverting the coefficient matrix. As the equations were solved entirely with Neumann boundary conditions, the resulting pressure field was normalised using the measured quiescent air pressure as reference.

5.6.1. Validation

The numerical procedure was validated by reconstructing pressure for a synthetic flow field consisting of a Lamb-Oseen vortex (Azijli et al., 2016). Expressed in 2D polar coordinate system with radius r

and azimuthal angle θ, the analytical velocity and pressure field are described as follows:

$$V_\theta = \frac{\Gamma}{2\pi r}\left(1 - \exp\left[\frac{-r^2}{4\nu t}\right]\right) \tag{5.10a}$$

$$V_r = 0 \tag{5.10b}$$

$$p = \frac{\rho\Gamma^2}{4\pi^2}\left[-\frac{1}{2r^2} + \frac{\exp\left[-r^2/4\nu t\right]}{r^2} - \frac{1}{2}\frac{\exp\left[-2r^2/4\nu t\right]}{r^2} + \dots \right.$$
$$\left. + \; Ei\left(\frac{-2r^2}{4\nu t}\right)\frac{1}{4\nu t} - Ei\left(\frac{-r^2}{4\nu t}\right)\frac{1}{4\nu t}\right] \tag{5.10c}$$

Where ν is the kinematic viscosity, Γ is the vortex circulation, t is time and Ei is the exponential integral function.

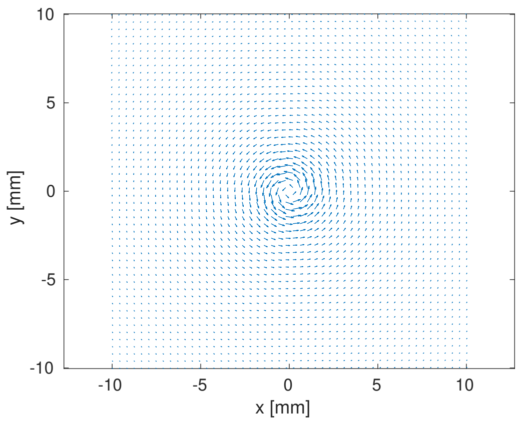

(a) Synthetic velocity field

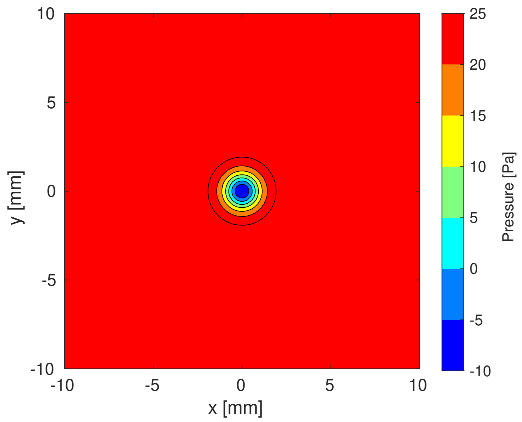

(b) Analytical Pressure field

Figure 5.11: Analytical solution of Lamb-Oseen vortex

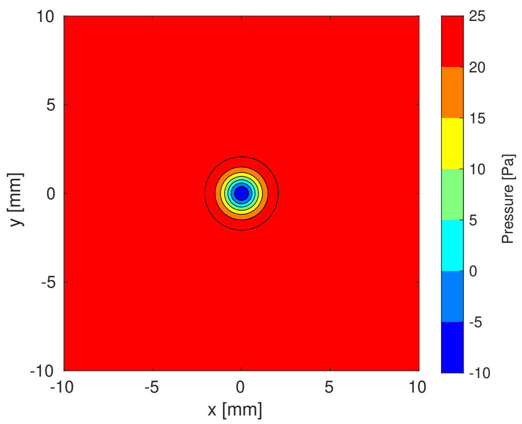

(a) Pressure field from PPE

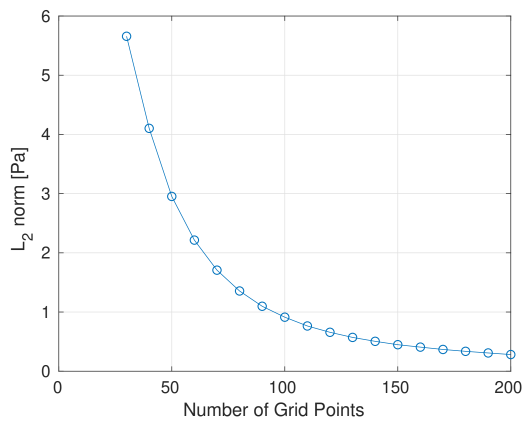

(b) Effect of grid resolution on RMS error

Figure 5.12: Numerical solution of Lamb-Oseen vortex

A 2D square domain of 20 mm length was chosen with the vortex core at the centre of the domain. Figure 5.11 shows the stationary Gaussian vortex and the associated pressure field with very low pressure at the vortex core. The velocity field described by Equations 5.10a and 5.10b were converted to Cartesian coordinates and subsequently, the pressure field was reconstructed by solving the pressure Poisson equation. The resulting pressure field (Figure 5.12a) agreed well with the analytical solution. Further, as the grid resolution was refined, the RMS error between the analytical and numerical solutions decreased rapidly as shown in Figure 5.12b. This RMS error was calculated based on the centreline pressure variation.

6

Results and Discussions: Individual Cyclists

The results of the individual cyclists are discussed in this chapter, starting with a qualitative discussion of flow fields. The full wake of an individual cyclist is analysed from ensemble averaged velocity and pressure fields, followed by a comparison between the three cyclists. Quantitative analysis using drag area is discussed in the next section, addressing the sensitivity to wind and distance in the wake. The spread of data is also addressed along with the contribution of the momentum and pressure term to the total drag. The chapter concludes with the discussion on ensemble-averaged drag and the associated uncertainty.

Contents

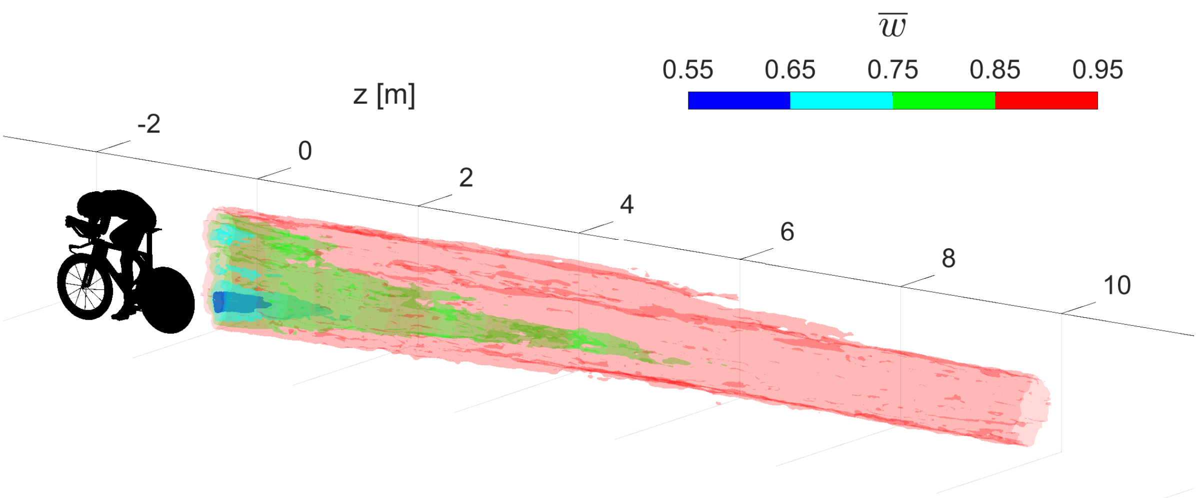

Figure 6.1: Isosurfaces of ensemble averaged non-dimensional wake velocity

6.1. Flow Fields

The coordinate system used by LaVision DaVis 8.4 was adopted with the x-coordinate representing the lateral direction, y-coordinate representing the vertical direction and z-coordinate representing the streamwise/longitudinal direction, with the origin at the rear of the cyclist. In this frame of reference, the cyclist is moving into the measurement plane with the cycling direction corresponding to negative z-direction.

The wake flow fields are ensemble averaged using data obtained from multiple cyclist passages, with 6, 10 and 11 passages for the small, medium and large cyclist respectively. Windy outdoor conditions caused low and non-uniform seeding concentration for the small cyclists which resulted in fewer usable data sets. The crank angle history of the cyclists were not tracked during the experiments and hence, the flow fields are not phase-averaged like previous Ring of Fire experiments (de Martino Norante, 2018; Spoelstra, 2017). Therefore, the averaged flow fields contain information from all possible crank angle positions. As the flow fields are not aligned in the lateral direction, they are shifted to the centre of the domain and then averaged. The velocity fields are non-dimensionalised with the freestream velocity after converting the frame of reference as follows:

$$\overline{w} = \frac{w_{\text{wake}} - w_{\text{cyc}}}{w_{\infty} - w_{\text{cyc}}} \tag{6.1a}$$

$$c_p = \frac{p_{\text{wake}} - p_{\infty}}{\frac{1}{2}\rho\left(w_{\infty} - w_{\text{cyc}}\right)^2} \tag{6.1b}$$

6.1.1. Full Wake

Figure 6.1 shows isosurfaces of ensemble averaged non-dimensional velocity fields in the wake of the large cyclist. It can be seen that the region of velocity deficit corresponding to 20% and 10% extends up to 6 m and beyond 10 m respectively, indicating that a trailing cyclist 10 m behind the leading cyclist can still experience a benefit. The evolution of the cyclist wake can be observed in Figure 6.2, where it can be seen that the average wake velocity decreases with increasing distance in the wake, with the region of high deficit (40%) extending to less than 2 m in the wake.

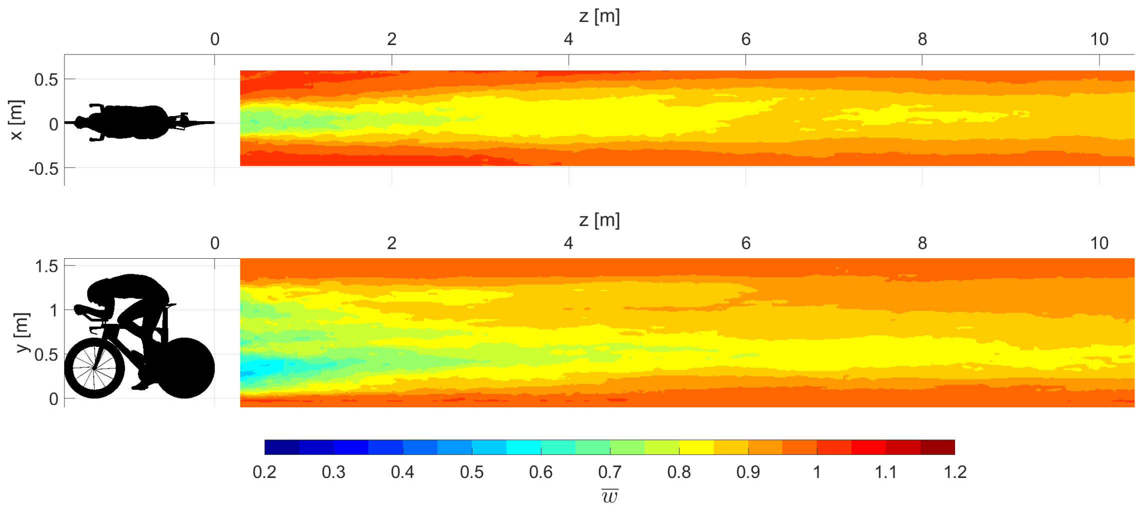

Figure 6.2: Top view at y = 0.8 m and side view at x = 0 m of ensemble averaged non-dimensional wake velocity

The top view in Figure 6.2 shows that the wake expansion is greater in the lateral direction compared to the vertical direction. These observations agree with those reported by Spoelstra (2017), where similar wake evolution was observed. It can be seen that the wake expansion is limited in the vertical

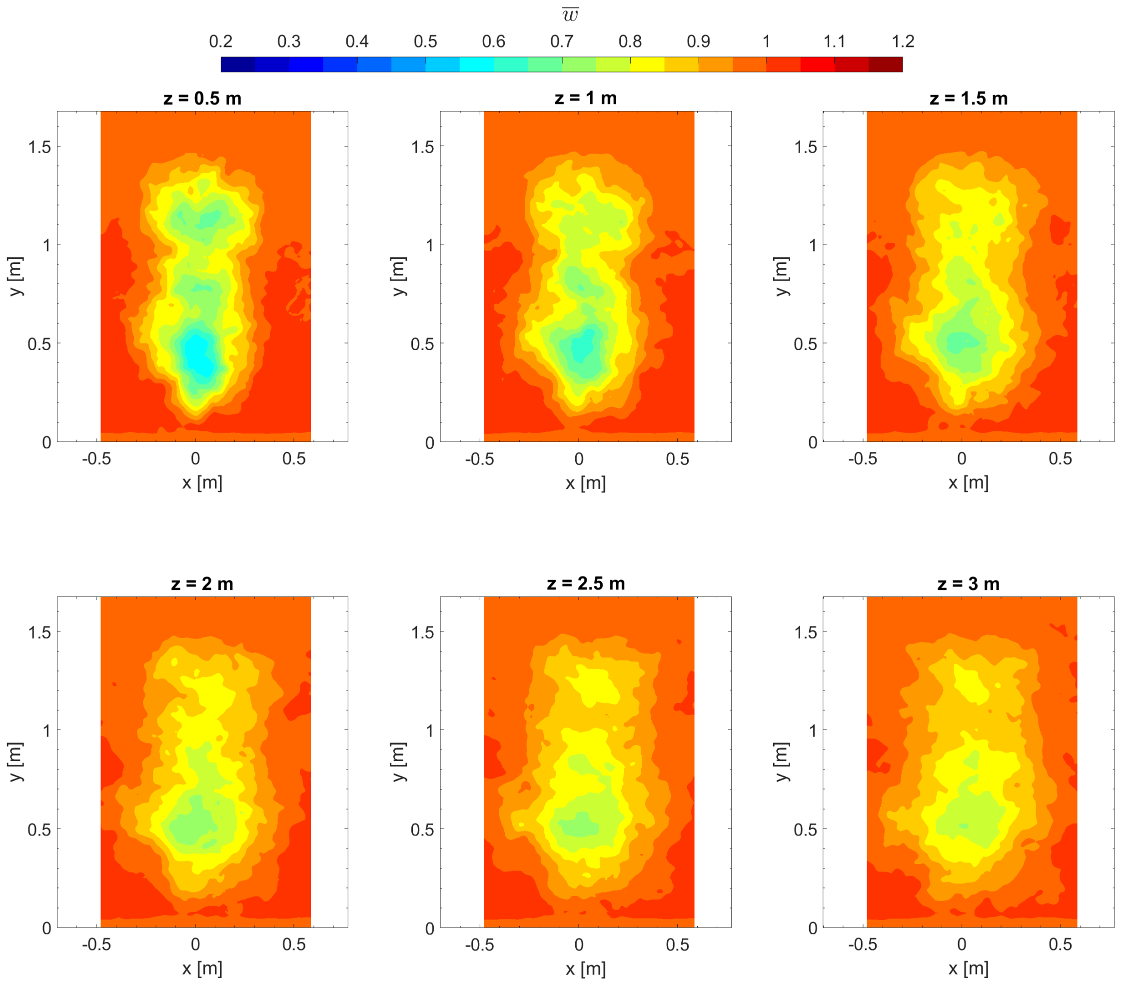

(a) Variation of ensemble averaged non-dimensional wake velocity with distance

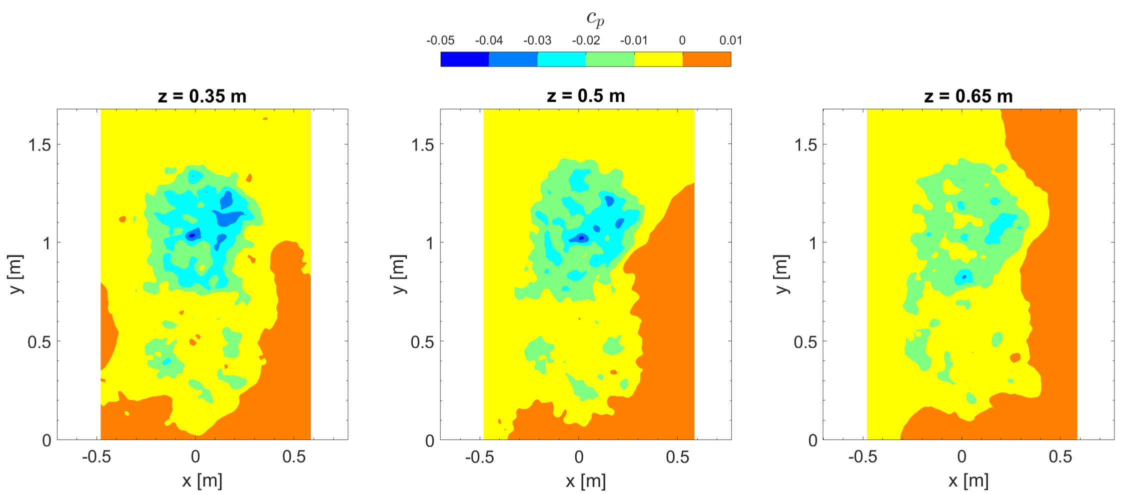

(b) Variation of ensemble averaged pressure coefficient with distance

Figure 6.3: Variation of wake flow fields with distance

direction due to the presence of the bottom wall/ground. Figure 6.3a shows the wake velocity at different planes normal to the cyclist direction. Three regions of high deficit can be observed in the first plane with a maximum deficit of 45% from the lower part of the field of view. The large area of deficit at the lower part of the wake is due to the wake of the rear wheel and the drive train. This deficit is highest as this plane is closest to the rear wheel. The area of deficit in the middle approximately corresponds to the location of vortices shed from the inner thigh and lower hip of the cyclist (Crouch et al., 2014). The region of deficit at a height of 1.2 m corresponds to the location of the upper back of the cyclist and the presence of such deficits at z = 0.5 m suggests that these are areas of improvements for the cyclists as such deficits were reported to recover before z = 0.5 m by Crouch et al. (2014). Nonetheless, this region at 1.2 m height is the first to recover after 1 m in the wake, while the middle region at 0.8 m height recovers next after 2 m in the wake and lastly the high deficit originating behind the drive train recovers after 3 m where the overall peak velocity deficit has reduced to 25%. Therefore, it can be seen that a trailing cyclist 3 m behind can still experience a significant aerodynamic benefit.

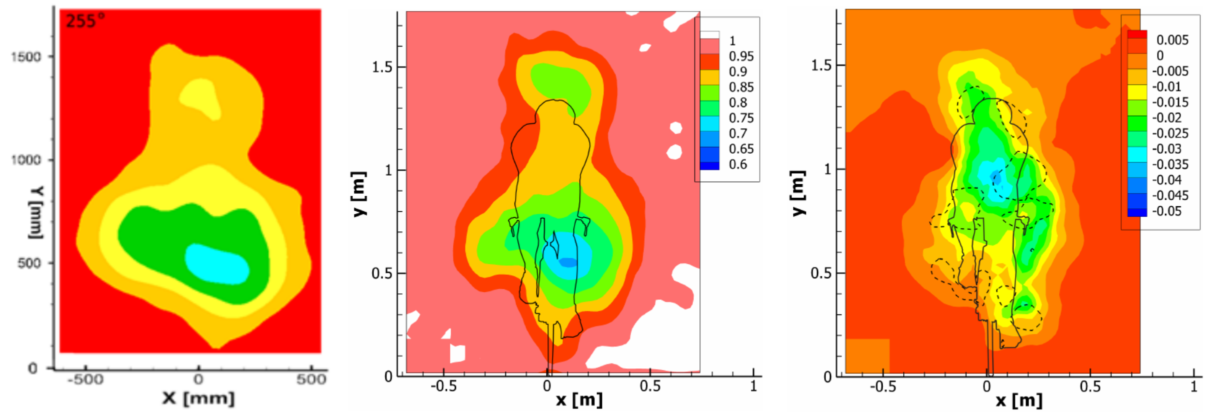

(a) Phase-averaged non-dimensional velocity at z = 2.7 m (Spoelstra, 2017)

(b) Phase-averaged non-dimensional velocity at z = 2.8 m (de Martino Norante, 2018)

(c) Phase-averaged pressure coefficient at z = 0.56 m (de Martino Norante, 2018)

Figure 6.4: Velocity and pressure fields reported by previous Ring of Fire experiments

The observation made in Figure 6.2 is confirmed with the wake expanding more in the lateral direction compared to the vertical direction. The combination of strong downwash in the wake of the cyclists (Crouch et al., 2014; de Martino Norante, 2018; Hirsch, 2018; Spoelstra, 2017) and the presence of the ground counteracts wake expansion in the vertical direction. Furthermore, wake expansion in the lateral direction is greater in the lower half of the wake compared to the top half, which was also reported by previous Ring of Fire experiments (Figures 6.4a and 6.4b). Hirsch (2018) showed that the circulation due to the dominant hip vortices create outwash and inwash at the lower and upper half of the wake respectively. This results in higher expansion in the lower half compared to the upper half of the wake (Figure 6.5c).

The evolution of pressure coefficient in the wake of the cyclist with distance can be observed in Figure 6.3b. The magnitude of pressure coefficient is quite low to begin with and the recovery of the low pressure regions is much faster compared to velocity, with the effect of pressure being minimal at 0.65 m, with similar observations made by Terra et al. (2016a) and de Martino Norante (2018). Low pressure regions can be observed in the wake with higher contribution from the top half of the wake compared to the lower half. Vortical structures cannot be identified without confidence as the flow fields are not phase-averaged. However, the presence of these low pressure regions in the upper half of the wake suggests that it is mainly due to separation from the back of the cyclist. Even so, local regions of low pressure in the lower half correspond to locations of knee and shin vortices as reported by previous experiments (Figure 6.4c).

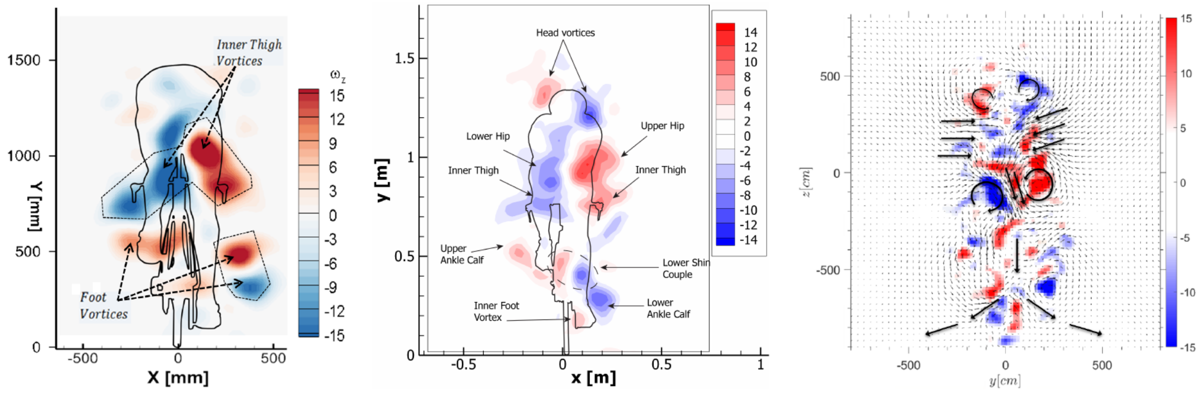

(a) Phase-averaged streamwise vorticity at 0.8 m behind the saddle reported by Spoelstra (2017)

(b) Phase-averaged streamwise vorticity at 0.56 m in the wake reported by de Martino Norante (2018)

(c) Ensemble-averaged streamwise vorticity at 0.5 m in the wake reported by Hirsch (2018)

Figure 6.5: Streamwise vorticity reported by previous Ring of Fire measurements

6.1.2. Near Wake Comparison

Ensemble averaged non-dimensional wake velocity is compared between the three cyclists in Figure 6.6. It can be seen that the peak velocity deficit does not follow the classification made based on the cyclists' height, with medium, large and small corresponding to increasing order of peak velocity deficit in the wake respectively.

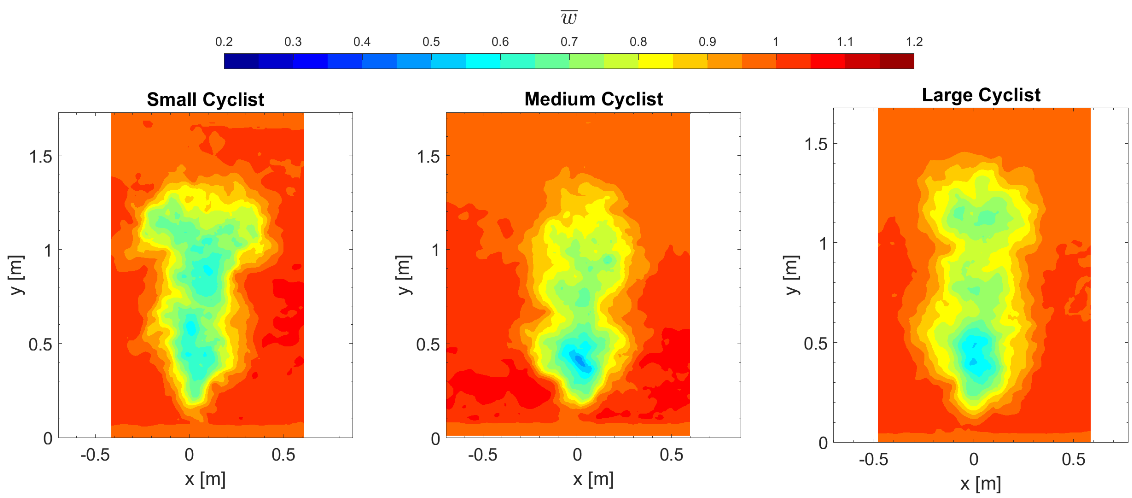

Figure 6.6: Comparison of ensemble averaged non-dimensional wake velocity at z = 0.5 m

Similarly, the size of the wake does not follow the classification, with the medium, small and large corresponding to increasing order of wake size respectively. It can be seen that the wake shape of the small cyclist is distinctly different from the others i.e. the wake has a narrow bottom half with a wide top half which is not observed for the medium and large cyclist (Figure 6.7). Pressure coefficient comparison between the cyclists reveals that the the top half of the wake is characterised by low pressure (Figure 6.8). Further, the size of the low pressure region is bigger for the small cyclist compared to the other cyclists. Crouch et al. (2014) and Figure 6.5 shows that these regions are dominated by counter-rotating vortices. It seems that these vortices of the small cyclist are stronger relative to the medium and large cyclist. Given that the small cyclist used different equipment, particularly clothing and helmet, this difference in shape of the wake can be attributed to this difference in equipment. However, phase-averaged velocity and pressure fields is required to confirm this deviant behaviour of the small cyclist.

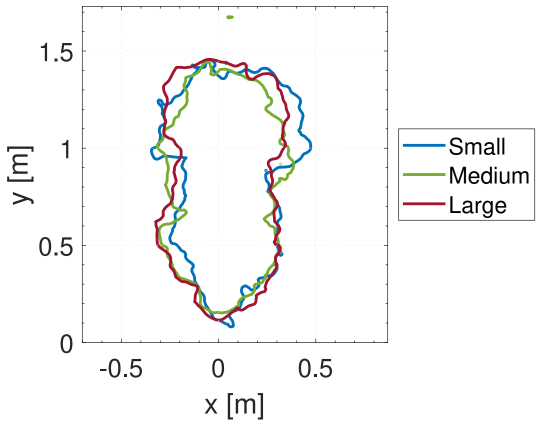

Figure 6.7: Comparison of isoline of velocity between different cyclists at z = 0.5 m

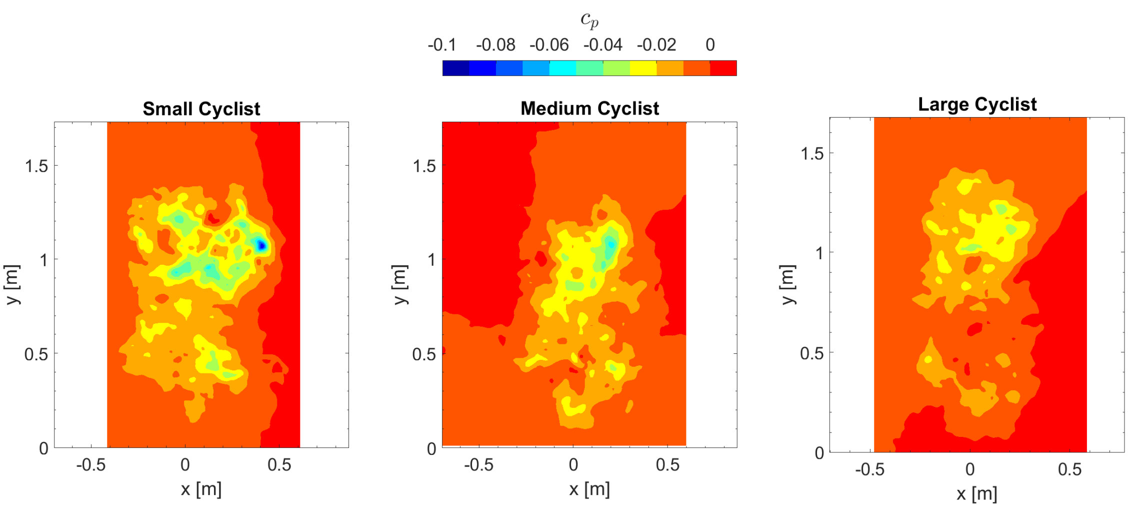

Figure 6.8: Comparison of ensemble averaged pressure coefficient at z = 0.5 m

The near wake of the three cyclists along streamwise vertical and horizontal planes are compared in Figure 6.9. The first, second and third row correspond to the small, medium and large cyclist respectively. The side view of the wake confirms the observations made using Figure 6.6 with respect to the size of the wake as well as velocity deficit for the three cyclists. Surprisingly, the peak velocity deficit of the medium cyclist is strongest while the deficit of the small cyclist decays faster compared to the other two. The top view of the comparison at a height of 0.4 m from the ground shows that the expansion of the wake is quite conservative for the small cyclist whereas the wake expands quite rapidly for the large cyclist. It was also observed that the velocity deficit of the medium cyclist extends further into the wake compared to the other cyclists. Figures 6.6, 6.8 and 6.9 show the while peak velocity deficit and peak c_p cannot be used as qualitative indicators of cyclist size, the size and evolution of the wake does follow the classification made using the heights of the cyclists. However, the small cyclist is the exception to this, with the shape and size of the wake being different. This suggests that others factors such as cyclist clothing, equipment, bicycle and cycling skill may also have an influence.

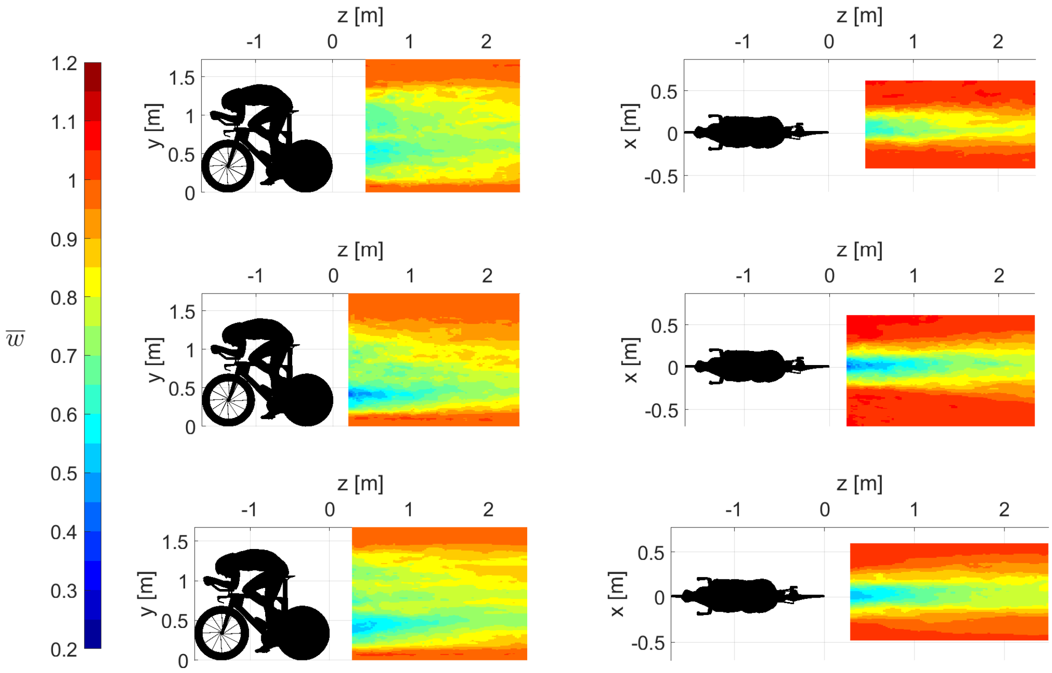

Figure 6.9: Comparison of side (at x = 0 m) and top view (at y = 0.4 m) of ensemble averaged non-dimensional wake velocity for different cyclists. Small, Medium and Large correspond to the first, second and third row respectively.

6.2. Drag Analysis

Conservation of momentum is applied between velocity fields captured upstream and downstream of the cyclist, using which the drag force is calculated and subsequently normalised with dynamic pressure to obtain drag area. Every velocity field in the wake of the cyclist is associated with a drag area value. As velocity fields in the wake correspond to different distances away from the cyclist, drag area can be plotted as a variation with this distance. Figure 6.10 shows the variation of drag area for different locations in the near wake of the cyclists. The light grey coloured lines represent the drag variations obtained during different cyclist passages, while the black line represents the ensemble averaged drag area. Statistical uncertainty of the mean drag area is also shown using error bars. This uncertainty (U) is determined using the standard deviation (σ) and a 95% confidence interval (k = 2) as follows:

$$U = k\frac{\sigma}{\sqrt{N}} \tag{6.2}$$

It is to be noted that the error bars are shown only for every 5th data point to avoid clutter and improve visualisation. Firstly, it can be seen that the magnitude of drag area for all three cyclists are lower than those reported by wind tunnel experiments as well as by previous Ring of Fire experiments (Crouch et al., 2014; de Martino Norante, 2018; Hirsch, 2018; Spoelstra, 2017). Particularly, comparing with the drag area reported by Hirsch (2018), the current experiments are lower by approximately 10% on average. These low drag area values seem to be a systematic error as opposed to a random error as all uncorrelated measurements have low drag area. A closer examination of the methodology used to calculate drag area revealed that the wake contouring procedure (discussed in Section 5.4) may be responsible for this low magnitude of drag area. Essentially, an isoline of velocity ($\overline{w}$ = 0.97 on average) was used to identify the wake, with only velocity data inside the contour being considered for drag calculation. It can be seen that some data outside this contour, but still part of the wake, is not considered, resulting in lower drag area. A bigger contour could not be used for the current experiments as it was found that the shape of the contour was not coherent and well defined for isolines of velocity greater than 0.97. Previous Ring of Fire experiments utilised a similar contouring procedure with an isoline of velocity but this contour was expanded in size to include the wake region outside. Given that the current experiments have issues with strong reflections (Figure 5.6) and blockage of optical access due to cyclists (Figure 5.10a), a wake expansion procedure would be specific and different to each data set and would be arbitrary. Hence, in order to remain consistent with both individual and drafting results, such an expansion procedure was not employed. It can be seen that the systematic error introduced does not affect the precision of the drag area values as the drag reduction from drafting cyclists agrees well with literature, which is discussed in more detail in the following chapter.

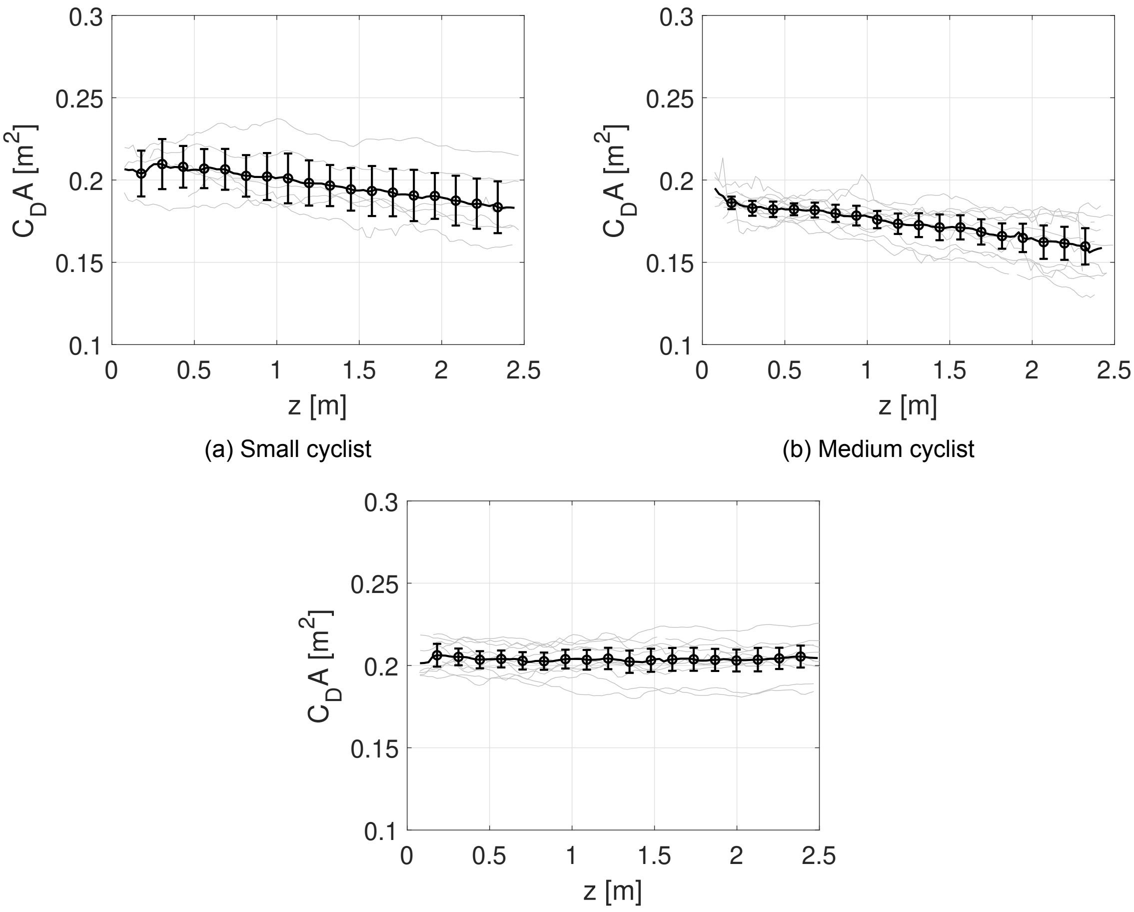

(a) Small cyclist

(b) Medium cyclist

(c) Large cyclist

Figure 6.10: Variation of ensemble averaged drag area with distance

Drag area is observed to decrease with distance, with a reduction of 11% and 18.6% over 2.4 m for the small and medium cyclist respectively. However, drag area remains relatively constant for the large cyclist, with a maximum change of 1.6% over 2.4 m in the wake. This suggests that this reduction is not due to processing techniques such as pressure reconstruction or wake contouring, as such an error would introduce the same reduction for all cyclists. It was observed that the testing days were characterised by strong winds and gusts and hence, a closer look at the velocity fields was prompted.

Figure 6.11 shows ensemble averaged non-dimensional velocity fields, with the first row corresponding to measurements upstream of the cyclist and the second row corresponding to measurements taken in the wake of the cyclists at z = 0.4 m. The contour levels are limited between 0.9 and 1.1 to visualise wind variation specifically. Comparing upstream and wake velocity fields for each cyclist shows that there is considerable change in wind before and after the cyclist passage. Specifically, this change in wind is significant for the small and medium cyclist, while lower fluctuations can be seen for the large cyclist. The high velocity (coloured by red) wind is strengthened in the wake for both the small and medium cyclist. This change in wind between upstream and downstream counteracts the wake of the cyclists, reducing the size of the wake and consequently momentum deficit. In order to quantitatively assess the effect of wind, the size of the wake is calculated at various locations in the wake of the

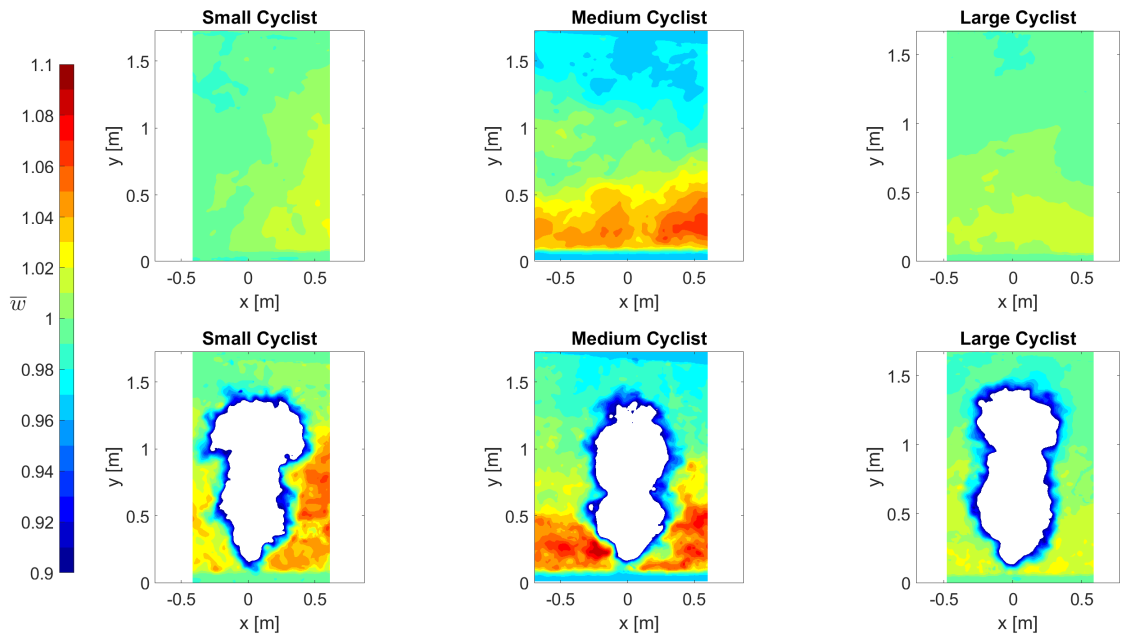

Figure 6.11: Variation of ensemble averaged non-dimensional velocity between upstream and wake at z = 0.4 m

cyclists. Figure 6.12 shows the evolution of the wake size with distance for the three cyclists. The size of the wake increases as expected for all cyclists, but the rate of growth is different, with the wake of the large cyclist growing at a faster rate compared to the other two cyclist. Figures 6.11 and 6.12 show that windy outdoor conditions can affect Ring of Fire measurements. It is to be noted that the measurements of the small and medium cyclists were taken on the first day of testing while measurements of the large cyclist were taken on the second testing day, which explains why such fluctuations and variations are common for the small and medium cyclist while they are not found for the large cyclist.

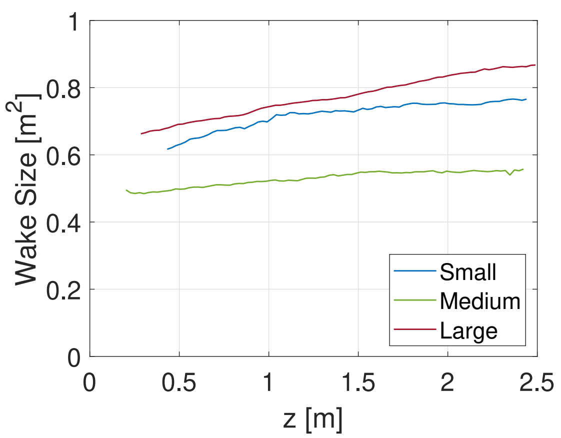

Figure 6.12: Variation of wake size with distance

6.2.1. Statistical Spread of Drag Area

Fluctuations of drag area in each cyclist passage is low compared to previous outdoor Ring of Fire experiments conducted by Spoelstra (2017), resulting in relatively low uncertainties of 2.4% on average for the medium and large cyclists, which is closer to the uncertainties reported by indoor Ring of Fire measurements of de Martino Norante (2018) and Hirsch (2018). The key difference between the current experiments and the previous outdoor Ring of Fire experiments is the data reduction techniques, specifically the contouring of the upstream and wake velocity fields. Essentially, the contouring procedure removes most of the “noise” in the velocity field outside the main wake region, resulting in lower spread of drag area in the current outdoor experiments. Comparing the drag area variation between different cyclist shows that the spread of drag area of the small cyclist is larger than the other two cyclists. As discussed before, this spread should not have a numerical cause. Although wind variation might have caused this spread, it cannot be the sole reason as then the spread of the medium cyclist should also be affected. It is to be noted that the number of usable data sets for the small cyclist was 6, compared to 10 and 11 for the medium and large cyclist respectively, and this is also one of the possible reasons for the larger spread. Further, the small cyclist was not part of Team Sunweb, but from another professional cycling team and hence, used different clothing, equipment and bicycle. In particular, the small cyclist used a time trial helmet with an elongated tail section, which was different from the other two cyclists. The raw images captured by the PIV cameras show that the small cyclist used different head postures in different passages (Figure 6.13). It was found that adopting a “head down” posture exposed more of the helmet tail to the freestream, while the “head up” posture tucked the helmet tail behind the head, shielding it from the freestream. This difference in head posture resulted in a maximum difference of 0.0158 m^2 in drag area for the two runs shown in Figure 6.13, which translates to 7.7% of the mean drag area. Hence, the combination of fewer usable data sets, variation in wind between upstream and wake planes, and variation in head postures resulted in higher statistical spread for the small cyclist.

(a) Run #004

(b) Run #010

Figure 6.13: Variation of head posture between different cyclist passages

6.2.2. Components of Drag Area

The contributors of drag area can be divided into momentum and pressure terms as described in Equation 3.12. Figure 6.14 shows the contribution of the components of drag area at different locations in the wake of the cyclists. The effect of the pressure term is highest (6% on average) just behind the cyclist and decays quite rapidly to approximately 4% at 0.5 m behind the cyclist, after which the rate of decay slows down, reaching an average of 2.5% at 2.5 m in the wake.

While the curves of the medium and large cyclist closely follow each other, both in terms of momentum and pressure contribution, the behaviour of the small cyclist is offset, showing larger pressure deficit at all distances compared to the other two cyclists. Higher relative pressure deficit suggests that amount of separation for the small cyclist is higher. The main difference between the small cyclist and other two is the equipment used such as the time trial helmet, skin suit and bicycle. The negative effects of changing postures was already discussed in the previous section and further, it was observed that the skin suit used by the small cyclist was not as close fitting as the other two cyclist from Team Sunweb, which may be another contributing factor towards higher pressure deficit. Higher pressure deficit suggests that a cyclist trailing the small cyclist would experience a higher benefit in terms of pressure term, compared to trailing the medium or large cyclist.

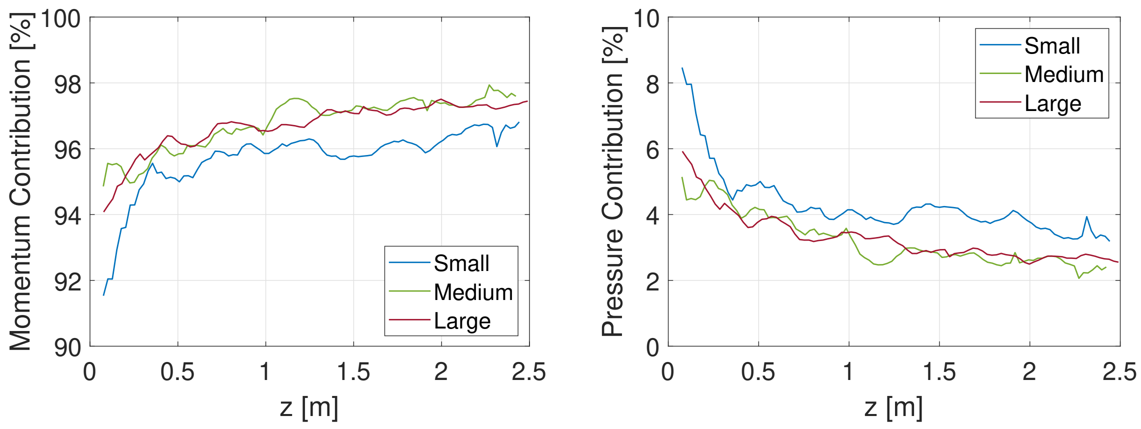

(a) Contribution of momentum term to total drag (b) Contribution of pressure term to total drag

Figure 6.14: Breakup of drag area into components

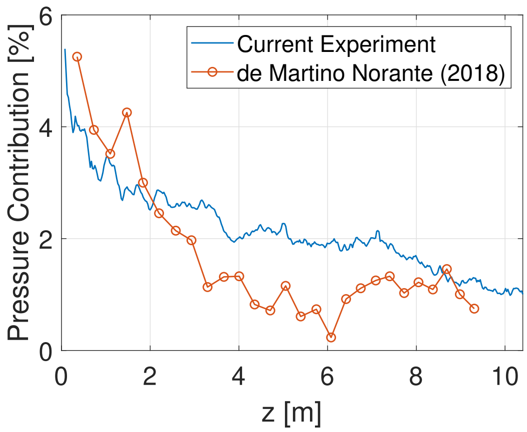

Figure 6.15: Comparison of pressure contribution

Comparison of the pressure contribution with previous literature shows that the current measurements do not agree with those reported by Shah (2017) where the pressure term was found to be 0.5% at a distance of 0.8 m behind the cyclist. It is to be noted that while pressure fields were reconstructed from volumetric velocity measurements by Shah (2017), the evaluation of the pressure term in the current experiments was performed using 2D velocity fields as out-of-plane gradients were not available from stereo-PIV measurements (Section 3.4.1), which might introduce some errors into the pressure reconstruction process. Comparison with previous Ring of Fire experiments of de Martino Norante (2018) in Figure 6.15 shows reasonable agreement up to 2 m in the wake, after which the rate of decay of the pressure term slows down in the current experiments. It is to be noted that the previous Ring of Fire experiments were conducted at a lower cyclist velocity of 5.3 m/s, which might explain the rapid decay of the pressure term compared to the current experiments.

6.2.3. Ensemble Averaged Drag

Drag area from different locations in the wake for each cyclist passage is averaged to obtain one drag area value for each passage. The standard deviation of such drag area values obtained from multiple cyclist passages are used to determine the statistical uncertainty using Equation 6.2. This uncertainty along with the drag area averaged over multiple passages is shown in Table 6.1. In order to remain consistent with drag area obtained from drafting configurations, the mean and uncertainties shown are calculated only over the first 1 m in the wake. The choice of using data only within 1 m will be explained in more detail in the next chapter.

Table 6.1: Average drag area

Cyclist	C_DA [m^2]	Uncertainty [m^2]	Uncertainty [%]
Small	0.2046	$\pm$ 0.0115	$\pm$ 5.6
Medium	0.1821	$\pm$ 0.0041	$\pm$ 2.3
Large	0.2038	$\pm$ 0.0048	$\pm$ 2.4

It can be seen that the classification of the cyclists based on height agrees with the medium and large cyclist, but the small cyclist is an outlier. The medium cyclist has the lowest drag area, while there is negligible difference between the drag areas of the small and large cyclists. Figure 6.16 shows that there is no overlap between the uncertainties (shown using error bars) of the medium cyclist with the large cyclist, indicating that this difference in drag area is not due to measurement uncertainty. Further, it can be seen that the uncertainty in drag area of the small cyclist is more than twice than that of the other cyclists.

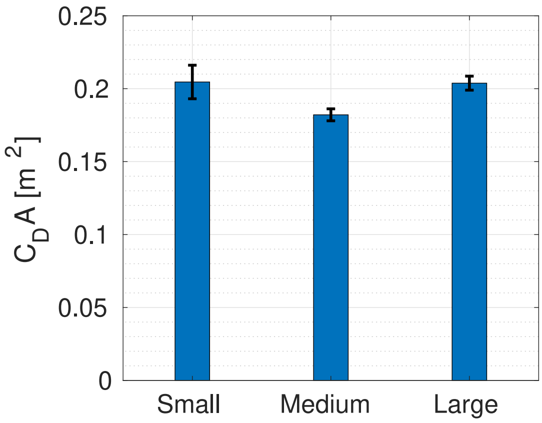

Figure 6.16: Comparison of drag area between cyclists

Considering Figure 6.9 and the resulting drag value in Table 6.1, it can be seen that although the medium cyclist had highest peak velocity deficit compared to the other two cyclists, it did not result in a higher drag area, suggesting that the size of the wake is a better indicator of drag area of a cyclist compared to other qualitative parameters.

7 Results and Discussions: Drafting Cyclists

The results from drafting cyclists are discussed in the current chapter starting with the discussion on drafting distance and the variations observed between different data sets as well as different configurations. The flow fields are discussed next starting with flow visualisation in-between the cyclists. Velocity and pressure fields are compared with each other and with individual wake. Similarly, the wake of the trailing cyclist is also investigated and the mechanism of drag reduction is addressed. Further, the effect of the size of the leading cyclist is discussed comparing velocity fields in-between and in the wake of the trailing cyclist. Quantitative analysis with drag area of the leading and trailing cyclist along with the drag area considering the two cyclists as a group is presented next. The effect of drafting distance on the drag reduction of the trailing cyclists is discussed. Investigations of anomalies in the drag data showed a correlation between the instantaneous “phase” difference between the leading and trailing cyclist on the flow fields and drag area.

Contents

7.1. Drafting Distance

Four configurations of two cyclists in drafting formation were tested with each configurations being repeated 10 times. However, low and non-uniform seeding distribution reduced the amount of usable data sets as shown in Table 7.1. Drafting distance in terms of longitudinal and lateral separation between the rear wheel of the leading cyclist and front wheel of the trailing cyclist (inter-wheel gap) was determined for each data set and the magnitude of these distances are shown in Figure 7.1.

Table 7.1: Number of usable data sets for drafting configurations

Configuration	Abbreviation	Number of Data Sets
Large - Medium	L - M	6
Small - Large	S - L	9
Large - Small	L - S	7
Medium - Small	M - S	10

Figure 7.1 is a scatter plot showing magnitude of longitudinal distance along the horizontal axis and magnitude of lateral distance along the vertical axis for different data sets of all the drafting configurations. Although all the cyclists were asked to maintain a constant drafting distance of 30 cm in the longitudinal direction with zero lateral offset, it can be seen that there is quite a large variation in drafting distance between different data sets of the same configuration as well as between different configurations. Longitudinal distance varies from 0.25 m to 0.86 m, while the maximum lateral distance was found to be 0.186 m.

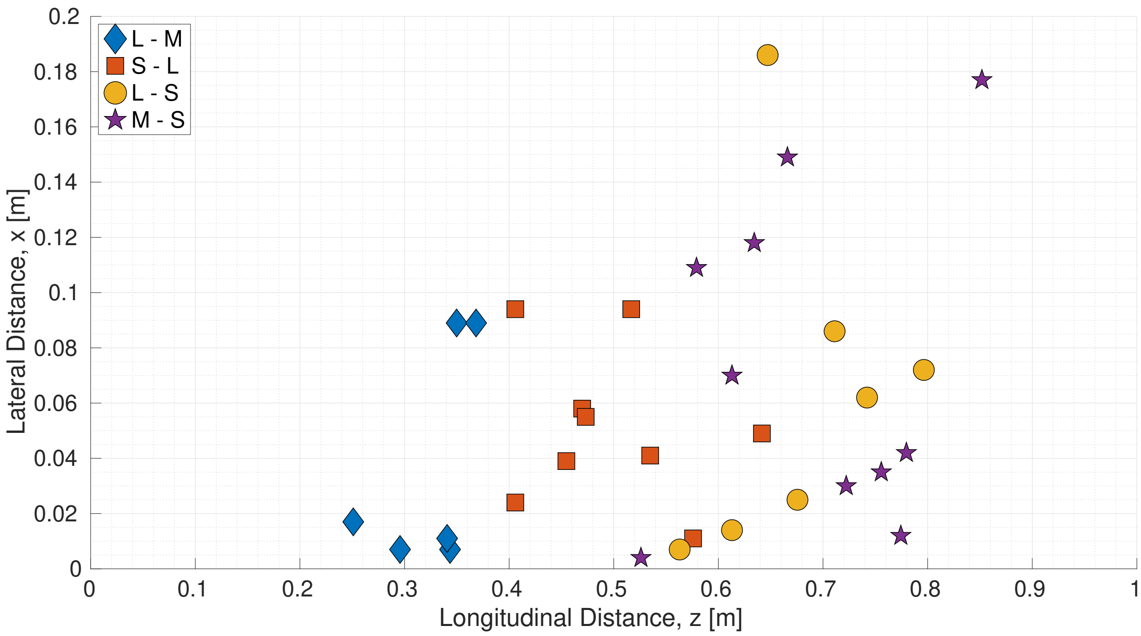

Figure 7.1: Variation of drafting distances between different cyclist passages

Table 7.2 shows the average and standard deviation of drafting distances maintained by each cyclist when they are trailing another cyclist. It is to be noted that these distances are determined only at the measurement plane and hence, one longitudinal and one lateral distance is obtained for every cyclist passage. On average, it can be seen that the medium cyclist was the closest to the required drafting distance while the small cyclist maintained more than double the required value. Although, these distances might not be representative on track, the variation in drafting distance between different data sets can be used as an indicator of the drafting ability/skill of the cyclist.

Table 7.2: Variation in drafting distances for each cyclist

Cyclist	$\bar{z}$ [m]	σ_z [m]	$\bar{x}$ [m]	σ_x [m]	$\bar{d}$ [m]	σ_d [m]
Small	0.685	0.091	0.071	0.059	0.691	0.092
Medium	0.325	0.043	0.037	0.041	0.329	0.047
Large	0.498	0.078	0.052	0.028	0.501	0.077

It can be seen from Figure 7.1 that at most three data sets from each drafting configuration can be found that are close together in terms of drafting distance, which means that it is not possible to obtain statistical convergence when ensemble averaging is performed. Hence, the inferences drawn from these comparisons might not be conclusive. However, the large variation in drafting distance will utilised to investigate the effect of drafting distance on drag reduction in more detail. It was seen from the previous chapter that fluctuations in wind can have an adverse impact on the determination of drag area. Therefore, in order to remain consistent between individual and drafting results, averaging of drag area from each data set was limited to the first 1 m (maximum longitudinal drafting distance) in the wake for all cases including individual configurations.

7.2. Flow Fields

Flow fields are obtained in-between the two cyclists (i.e. wake of leading cyclist) and downstream of both cyclists (i.e. wake of the trailing cyclist) which are ensemble averaged over multiple cyclist passages and compared with the flow fields from the individual results.

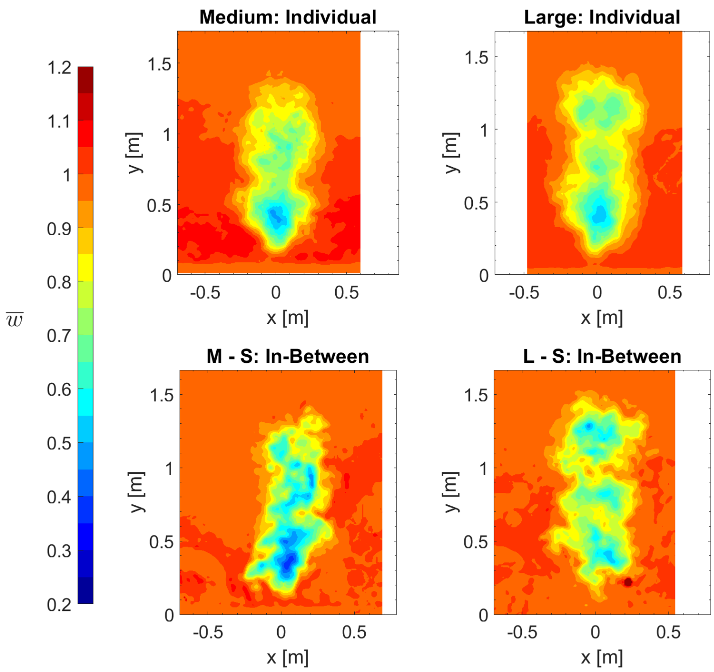

Figure 7.2: Comparison of ensemble averaged non-dimensional velocity between individual cyclist wake and wake of leading cyclist in drafting at z = 0.35 m

7.2.1. Wake of Leading Cyclist

The number of data sets available for averaging are particularly low for the in-between flow fields as they are affected by both the leading and trailing cyclist. Suppose 30 velocity fields are obtained in-between two cyclists, the central wake region in first few velocity fields are usually affected by strong reflections from the leading cyclist and hence, the first 10 fields are not considered and similarly, the last 10 velocity fields have to be neglected as the trailing cyclist interferes with the optical access of the PIV cameras, resulting in “unphysical” velocity fields. Effectively, only the middle 10 fields can be extracted as useful information. In some cases, there seems to be an overlap between the fields affected due to the leading and trailing cyclists and hence, no useful velocity fields can be obtained in-between the cyclists for that data set.

Nevertheless, certain data sets are identified with common drafting distances which have enough velocity fields in-between the cyclists and the ensemble averaged non-dimensional velocity in the wake of the leading cyclist is compared with their respective individual runs in Figure 7.2. It is to be noted that the number of data sets used for averaging are two and three for the M - S and L - S configurations respectively. Unfortunately, this comparison could not be made for the small cyclist as data sets with overlapping drafting distances did not have velocity fields in-between the cyclists. It can be seen that peak velocity is lower in the drafting configurations compared to their individual counterparts, with the M - S configuration showing 26.4% lower and the L - S configuration showing 5.7% decrease, compared to their respective individual wakes. This behaviour was reported by (Barry et al., 2016b) where a similar decrease in peak velocity was observed when compared to an individual cyclist. Upstream interference due to the trailing cyclist is the likely cause for this increase in velocity deficit, with the trailing cyclist “pushing” the air ahead.

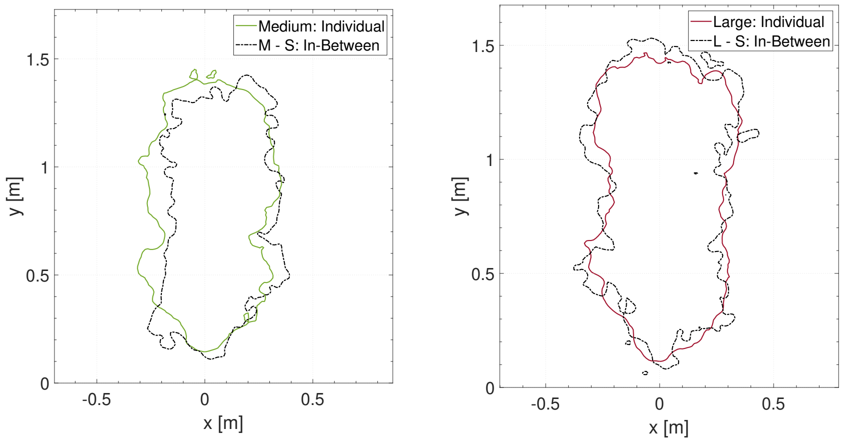

Figure 7.3: Comparison of wake sizes between individual and drafting configurations at z = 0.35 m

The size of the wakes between individual and drafting configurations is compared in Figure 7.3. The wake sizes are visualised using an isoline of $\overline{w}$ = 0.95 at the same distance in the wake. The size of the drafting wakes are consistent with the individual wakes, with small differences in the shape of the wake, especially for the medium cyclist. However, given that the M-S velocity fields are only averaged over two data sets, such conclusions cannot be drawn as statistical convergence from ensemble averaging is not achieved.

Figure 7.4 compares ensemble averaged pressure coefficient in the wake of the leading cyclist with individual wake for the medium and large cyclists. Similar to peak velocity, lower peak c_p can be observed while drafting compared to individual configurations. This is in contradiction with the CFD results of Blocken et al. (2013) which concluded that the presence of the trailing cyclist reduced the under-pressure in the wake of the leading cyclist. This is cited as one of the mechanisms for drag reduction associated with the leading cyclist. Lower magnitudes of pressure coefficient would translate to higher drag for the leading cyclists, resulting in increase in drag as opposed to drag reduction. More data sets are required for ensemble averaging to improve the statistics of the flow field and confirm this high pressure deficit.

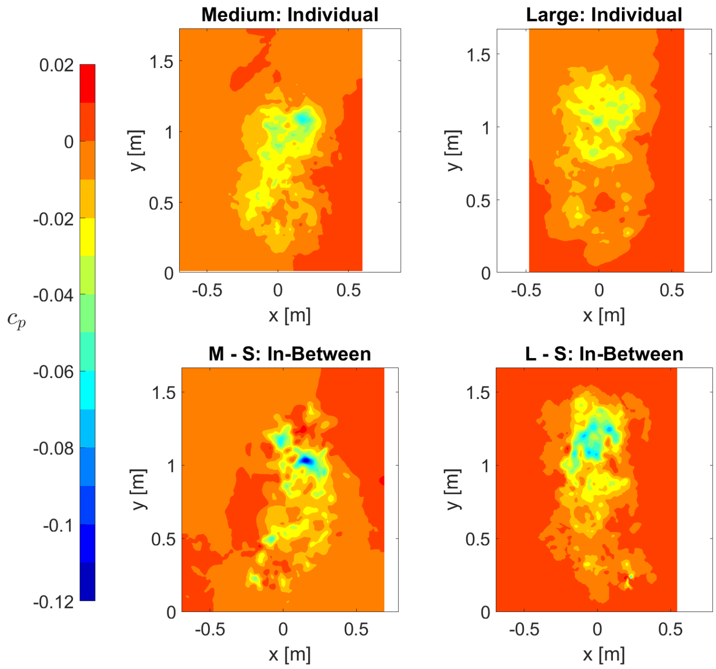

Figure 7.4: Comparison of ensemble averaged pressure coefficient between individual wake and in-between drafting cyclists at z = 0.35 m

7.2.2. Wake of Trailing Cyclist

The ensemble averaged non-dimensional velocity in the wake of the trailing cyclist in drafting is compared with the corresponding individual velocity fields in Figure 7.5. Three data sets were used for ensemble averaging of the drafting velocity fields. The size of the wake is bigger in drafting compared to the individual configurations as the wake of the leading cyclist is expanded by the passage of the trailing cyclist (Figure 7.6).

Disturbance of the in-plane velocities in the wake of the leading cyclist due to the trailing cyclist were reported to displace the thigh vortices away from the vertical centreline by Barry et al. (2016b), causing the wake to expand in the lateral direction. Further, the peak velocity is lower in the wake of the trailing cyclist compared to an individual cyclist. The lower velocity peaks in the wake of drafting cyclists shows that there is lower recovery of the flow to freestream conditions compared to individual wake and hence, the wake of the trailing cyclist is not the main reason for large drag reductions reported in literature.

Figures 7.2 and 7.4 show that the flow upstream of the trailing cyclist is characterised by low velocities and low pressure regions, resulting in overall lower momentum compared to the upstream flow experienced by an individual cyclist. Hence, this low energy flow upstream of the trailing cyclist is the main mechanism for the large drag reduction of the trailing cyclist. Barry et al. (2016b) and Barry et al. (2016a) showed similar low velocity in the wake of the trailing cyclist, attributing it to the low pressure flow upstream and also showed that the drag reduction of the trailing cyclist was due to the upstream flow. Further, symmetry in the wake of the trailing cyclist with respect to the vertical axis is not observed while this symmetry can be observed for the individual wakes. This indicates to possible interactions between the dominant flow structures of the leading wake with the trailing cyclist. However, this lack of symmetry in the wake of the trailing cyclist can also be attributed to the fewer number of data sets available for ensemble averaging.

Ensemble averaged pressure coefficient between the individual and drafting cyclists are compared in Figure 7.7. In general, peak c_p is lower in the wake of the trailing cyclist compared to individual wakes. As the wake of the trailing cyclist contains information about vortex structures shed by both the leading and trailing cyclist, it seems likely that these complex vortex combinations may be responsible for the low pressure regions observed. However, the study by Barry et al. (2016b) found that the strength of the

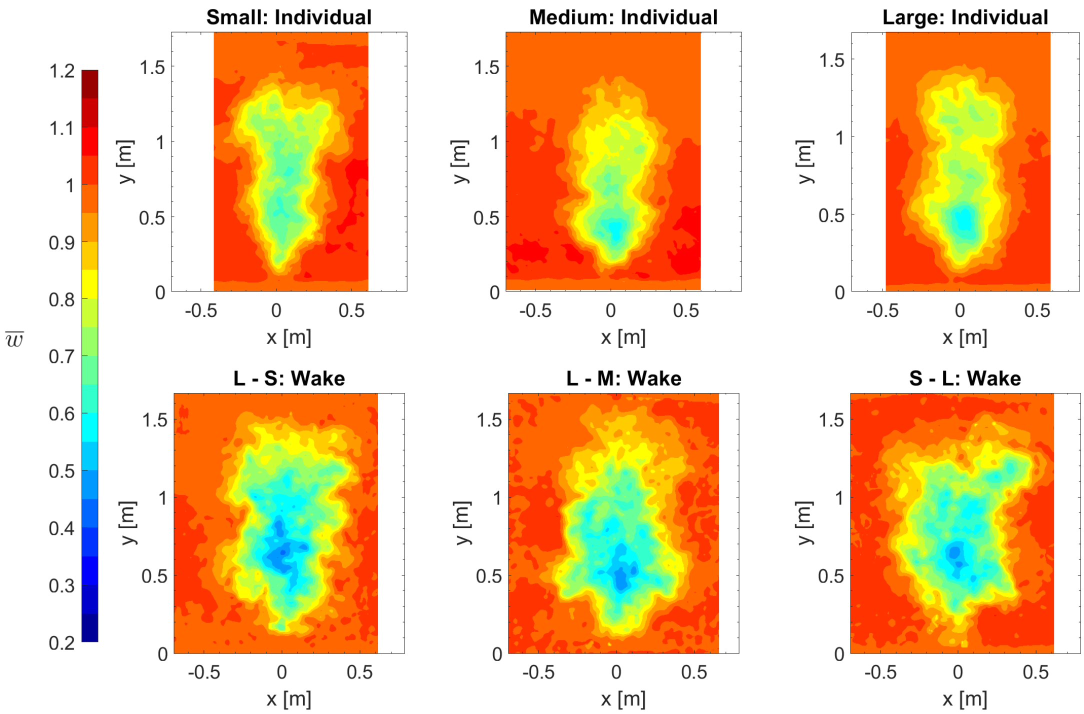

Figure 7.5: Comparison of ensemble averaged non-dimensional velocity between individual wake and wake of trailing cyclists at z = 0.8 m

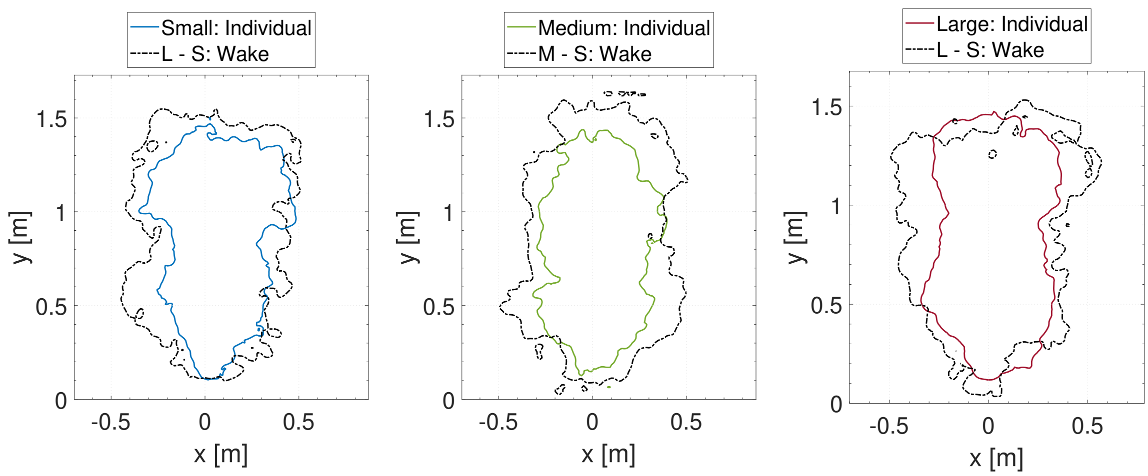

Figure 7.6: Isolines of wake velocity at z = 0.8 m

vortex structures (vorticity magnitude) in the wake of the trailing cyclist was lower than those observed for the individual cyclist wake. Moreover, the study showed that the leader wake had a significant influence on the wake structure of the trailing cyclist. Vortex structures shed by the leading cyclists were disturbed by the trailing cyclist and led to constructive and destructive interactions depending on specific crank angles adopted by both cyclists. Ensemble averaging over data sets results in mixing and such flow interactions cannot be characterised. Therefore, it is difficult to interpret and compare wake pressure fields of trailing cyclists from the current experiments.

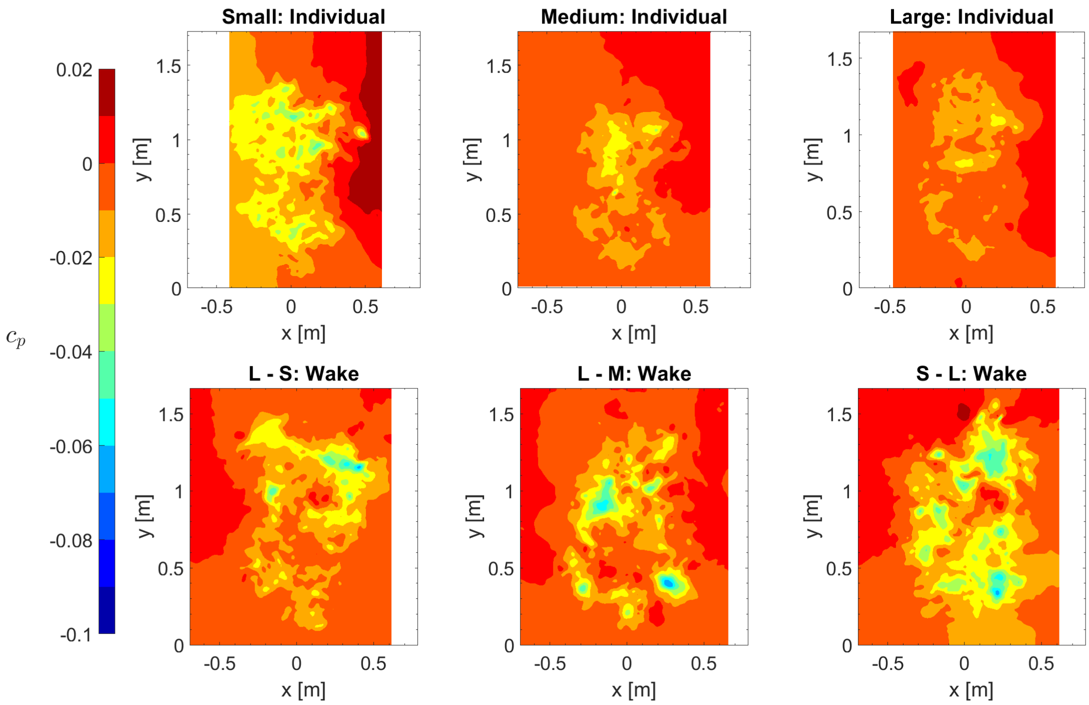

Figure 7.7: Comparison of ensemble averaged pressure coefficient between individual wake and wake of drafting cyclists at z = 0.8 m

7.2.3. Effect of Leading Cyclist

Review of literature shows that the size of the cyclist plays an important role in the drag reduction experienced while drafting (Section 2.4.2). Specifically, Edwards and Byrnes (2007) reported that the size and consequently drag area of the leading cyclist was directly proportional to the amount of drag reduction for a trailing cyclist. Although the current experiments were designed to study this effect of cyclist size, variation in drafting distance has prevented ensemble averaging over multiple cyclist passages. Nevertheless, an attempt is made to investigate this effect from instantaneous flow fields and drag data. In order to study the effect of size of the leading cyclist, the instantaneous velocity fields of the M-S and L-S configurations are compared in Figure 7.8, with the first and second row corresponding to upstream and downstream of the trailing cyclist respectively. These two data sets are chosen such that there are close together in terms of drafting distance (maximum difference in overall drafting distance is approximately 0.09 m).

The size of the leading cyclist seems to have an effect on the shape of the wake behind the trailing cyclist, with the wake of the L-S configuration being taller while the wake of the M-S configuration is relatively shorter and wider. This can be seen more clearly in Figure 7.9 which compares isolines of velocity behind the trailing cyclist for both the configurations. However, the size of the wake only shows a difference of 2.8% between the wakes of M-S and L-S configurations.

This difference in shape of the wake did not translate to drag area as the difference in drag reduction of the trailing cyclist between the M-S and L-S configurations was approximately 3%. Given that these comparison are made between instantaneous data and the measurement uncertainty of the Ring of Fire is of the same order, these observations may not not conclusive. Flow fields and drag area ensemble averaged over multiple data sets with the same drafting distance will provide a more concrete picture of the effect of the leading cyclist. A similar investigation on the effect of change in trailing cyclist could not be performed as no two drafting configurations were found close together in terms of drafting distance.

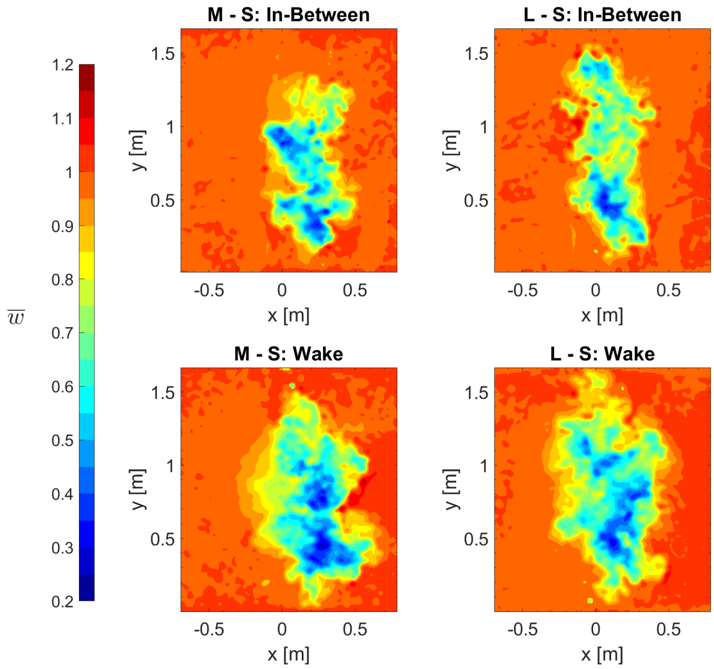

Figure 7.8: Comparison of instantaneous non-dimensional velocity upstream and downstream of the trailing cyclist at z = 0.5 m

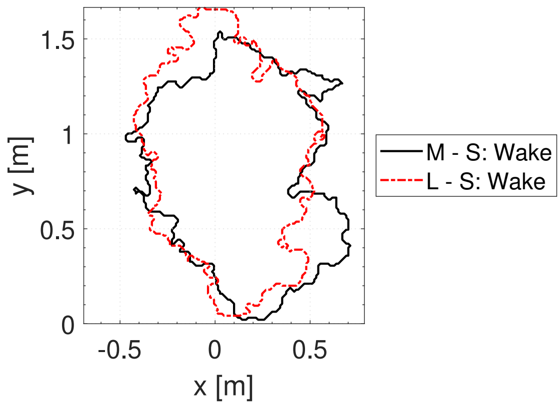

Figure 7.9: Comparison of isolines of instantaneous velocity in the wake of the trailing cyclist at z = 0.5 m

7.3. Drag Analysis

Velocity fields in drafting configurations are obtained at three locations with respect to the two cyclists in drafting i.e. upstream of both cyclists, in-between two cyclist and downstream of the both cyclists. Correspondingly, three drag areas are evaluated using different pairs of the above velocity fields, which are discussed below:

7.3.1. Leading Cyclist

Drag area of the leading cyclist is evaluated by applying the conservation of momentum enclosing the leading cyclist i.e. using velocity measurements upstream of the leading cyclist and in-between the two cyclists. The review of literature shows that the leading cyclist experiences a drag reduction of approximately 5% (Section 2.4.3). This reduction in drag area is determined as follows:

$$\mathrm{R_{lead}} = \frac{(C_D A)_{\mathrm{ind}} - (C_D A)_{\mathrm{lead}}}{(C_D A)_{\mathrm{ind}}} \times 100 \tag{7.1}$$

Where $(C_D A)_{\mathrm{ind}}$ is the individual drag area of the cyclist and $(C_D A)_{\mathrm{lead}}$ is the drag area of the leading cyclist in drafting formation. It can be seen that the reduction is positive when the drag area in drafting is smaller than the individual drag area and reduction is negative when drag area in drafting is higher than the individual case. Figure 7.10 shows the same graph as Figure 7.1, but the markers are coloured by the amount of drag reduction experienced by the leading cyclist. Here, drag area is not ensemble averaged over multiple cyclist passages as no two passages have overlapping drafting distances, and hence average drag area from each cyclist passage is shown.

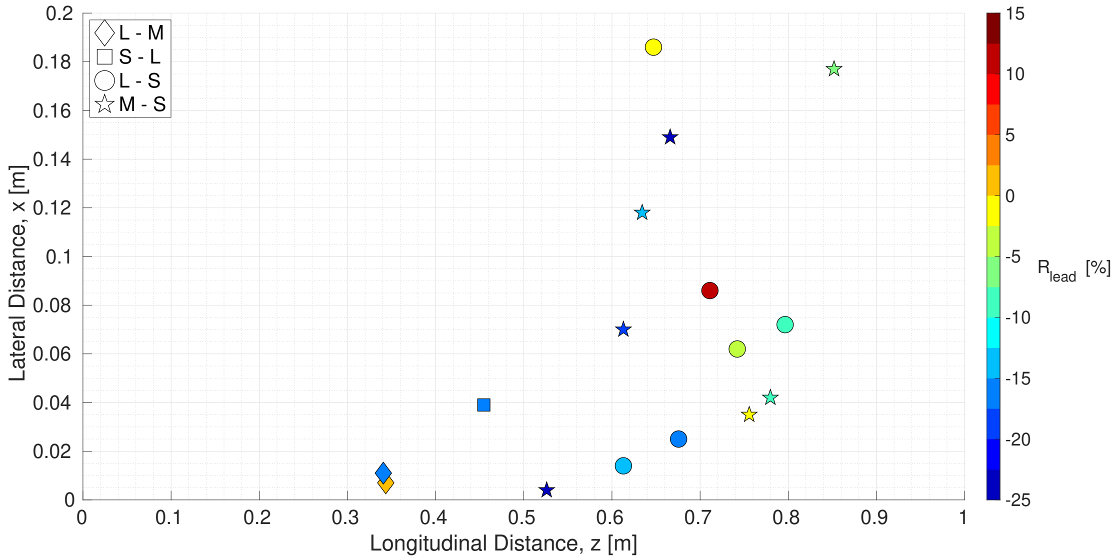

Figure 7.10: Drag reduction of leading cyclist

It is to be noted that instances when the trailing cyclist was too close to the leading cyclist restricted the optical access for the images captured in-between the cyclists, resulting in erroneous velocity fields (Figure 5.10) and hence these data sets were neglected and the number of scatter points shown above is fewer than that of Figure 7.1. As drag reduction of the leading cyclist is inversely proportional to both longitudinal and lateral drafting distances, it is expected that the highest reduction (red in colour) would occur at the lower left of the graph and the lowest reduction (blue in colour) would occur at the top right corner of the graph. However, it can be seen that most of the drag reduction is negative, i.e. increase in drag area is reported for the leading cyclist in drafting configuration, with only two data sets reporting decrease in drag area. Flow visualisation showed that both velocity and pressure deficit are higher in-between the two cyclists compared to an individual cyclist (Figures 7.2 and 7.4). This would translate to higher drag for the leading cyclist based on integral momentum analysis. As discussed previously in Section 2.4.3, the maximum drag reduction experienced by the leading cyclist was found to be 5% at minimum spacing between the cyclists (Barry et al., 2014; Blocken et al., 2013). This drag reduction was strongly dependent on longitudinal spacing between the cyclists, with the benefit reducing to less than 3% at 0.5 m spacing. Given that the measurement uncertainty associated with the Ring of Fire technique is of the order of 5%, this reduction in drag area for the leading cyclist cannot be measured with certainty using single data sets as shown in Figure 7.10. Nevertheless, increase in drag area by 25% can be observed which is well above the measurement uncertainty. Therefore, there seems to be some error in the calculation of the drag area of the leading cyclist as an increase in drag is not reported in any literature. CFD simulations by Blocken et al. (2013) showed that there is a nuanced interaction between the pressure fields of the leading and trailing cyclists, due to upstream propagation of the trailing cyclist. The 2D pressure reconstruction employed in the current experiments does not take into account these out-of-plane gradients (Section 3.4.1) and Van Oudheusden (2013) showed that stereoscopic-PIV measurements (2D-3C) are not sufficient for solving the pressure Poisson equation (Section 5.6) in the presence of 3D flow. Tomographic PIV is required to determine the gradients in the out-of-plane direction, which would provide a more accurate representation of the pressure field in-between the cyclists. Therefore, it seems that the assumption of quasi-2D flow made to solve the planar pressure fields is over-predicting the pressure deficit of the leading cyclist, resulting in increase in drag area evident from Figure 7.10.

7.3.2. Trailing Cyclist

Drag area of the trailing cyclist was measured using the velocity fields obtained in-between the two cyclist and the wake of the trailing cyclist. Similar to the leading cyclists, the drag reduction for the trailing cyclist is defined as follows:

$$\mathrm{R}_{\text{trail}} = \frac{(C_D A)_{\text{ind}} - (C_D A)_{\text{trail}}}{(C_D A)_{\text{ind}}} \times 100 \tag{7.2}$$

Numerous studies have been performed that have focused on the effect of drafting distance on the drag reduction for the trailing cyclist as mentioned in Section 2.4.1. Maximum of 49% drag reduction was reported at minimum drafting distance and this benefit decreased as longitudinal and lateral distances increased between the cyclists (Barry et al., 2014). Figure 7.11 shows the drag reduction for the trailing cyclist obtained from the current experiments for various drafting distances.

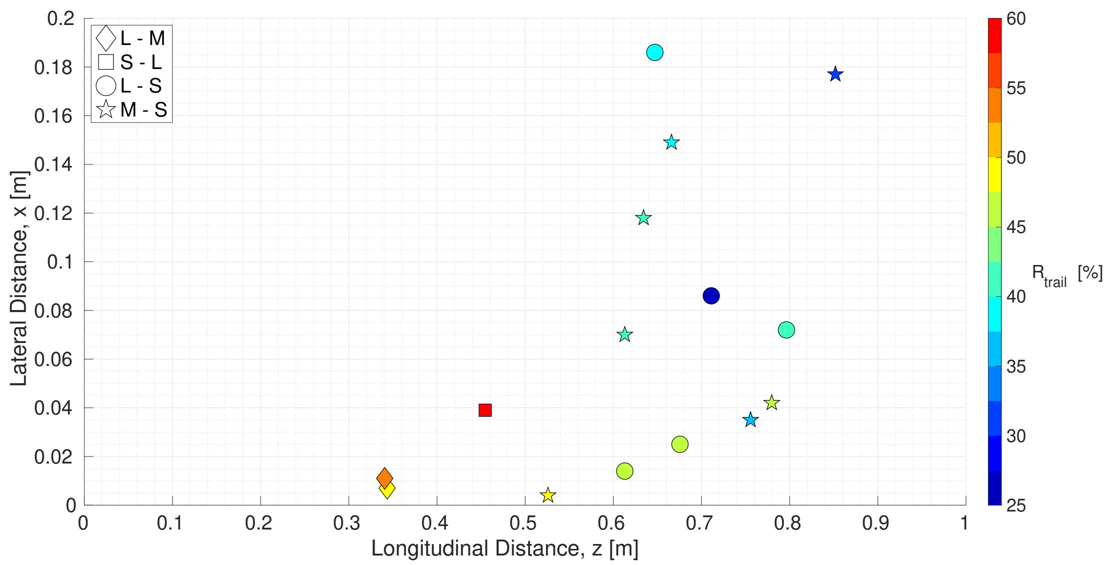

Figure 7.11: Drag reduction of trailing cyclist

Drag reductions between 27% and 60% are observed with a general inverse relationship between drag reduction and drafting distance, with high reductions near the lower left of the figure where both longitudinal and lateral distances are low and drag reductions are low when the overall drafting distance is higher. It is observed that the effect of lateral distance is much stronger than longitudinal distance. Figure 7.12 shows the effect of longitudinal and lateral distances on drag reduction of the trailing cyclist. The effect of longitudinal distance is investigated at zero lateral distance and the effect of lateral distance is investigated at z = 0.64 m. Comparison of the slopes shows that a decrease in longitudinal drafting distance of 10 cm translates to an increase in drag benefit by 1.3% while a similar decrease in lateral distance translates to 3.9% increase in drag benefit. This shows that lateral distance is approximately three times more important than longitudinal distance. The evolution of the wake with distance behind the cyclist was discussed in the previous chapter, where it was found that the wake expands with distance with the peak velocity deficits near the centre of the wake. As the lateral spacing between the cyclists increases, the trailing cyclists moves away from this low velocity and low pressure region and is exposed to high energy freestream. Consequently the amount of “shelter” received by the trailing cyclist decreases as the trailing cyclist moves away from the centre. Figure 7.13 compares the results of the current study with experiments and CFD simulations reported by Barry et al. (2014) and Blocken et al. (2018) respectively. The filled symbols and the linear fit correspond to the results from the current experiments for different longitudinal distances at x = 0 m. These two studies are chosen as the effect of longitudinal distance was studied with the cyclists' adopting the time trial position, similar to the current experiments. It can be seen that the results from the current experiments agree well with the wind tunnel tests by Barry et al. (2014), and while the regression line does not match exactly, the slope of the regression line seems to match quite well. The CFD simulations, on the other hand under-predicts the drag reduction for all longitudinal distances and is offset from both the wind tunnel and on-site measurements.

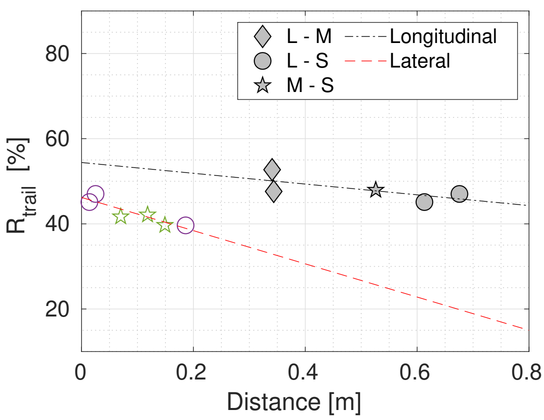

Figure 7.12: Effect of drafting distance on drag reduction of trailing cyclist. The filled symbols correspond to varying longitudinal distance at x = 0 m and the empty symbols correspond to varying lateral distance at z = 0.64 m

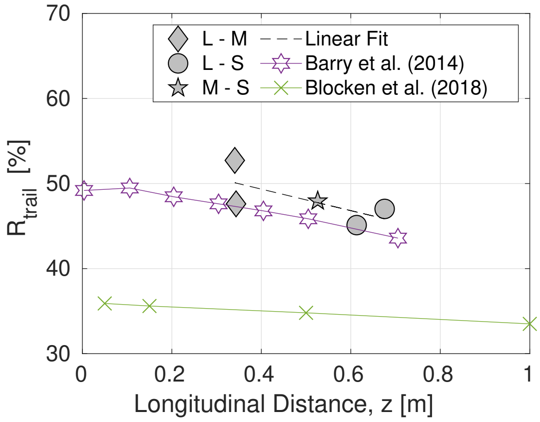

Figure 7.13: Comparison of drag reduction of trailing cyclist with literature. The filled symbols and the linear fit correspond to the current experiments for different longitudinal distances at x = 0 m

However, some irregularities are observed in drag reduction shown in Figure 7.11. The most dramatic outlier is the L - S data set at 0.7 m longitudinally and 0.09 m laterally which shows the least drag reduction at 27% while the neighbouring data points show higher drag reduction. This data set is further investigated and compared with the neighbouring L - S data set. All possible sources of error and differences between the two data sets were studied, including seeding, illumination, cyclist posture, wind variation, contouring procedure, pressure reconstruction, etc. The full list of possible sources of error is provided in Appendix D for reference. It was found that no obvious error was introduced in the two data sets, with the only difference being the crank angles of the leading and trailing cyclists. Scaled water tunnel tests of two drafting cyclists by Barry et al. (2016b) investigated this effect of difference in crank angle between the leading and trailing cyclists. The study found that the wake of the trailing cyclist is in fact influenced by the crank angles adopted by both cyclists. It can be seen in Figure 7.14 that the shape of the wake, location and strength of the vortex structures are different depending on the crank angle adopted by both cyclists. The study concluded that the wake of the trailing cyclist depends on the location and strength of the vortex structures in the wake of the leading cyclist (which depends on the crank angle of the leading cyclist) and also depends on the crank angle of the trailing cyclist. The structure of the leader wake ultimately influences the drag measurements of the trailing cyclist.

Therefore, in order to investigate whether this phenomenon, the instantaneous crank angle of the leading and trailing cyclists are compared in Figure 7.15, where Run #083 corresponds to the outlier. It can be seen that the difference in crank angle between the leading and trailing cyclists is close to 0° for Run #083, while the difference is closer to 180° for Run #041. Figure 7.16 compares instantaneous velocity fields from the two data sets, with the first and second row corresponding to upstream and downstream of the trailing cyclist respectively. The amount of low velocity upstream of the trailing cyclist is higher in Run #041 compared to Run #83. However, the opposite is observed in the wake of the trailing cyclist where there are relatively more regions of low velocity in Run #083. Further, it can be seen that the wake structure of the trailing cyclist is different in each case, with the wake being wider

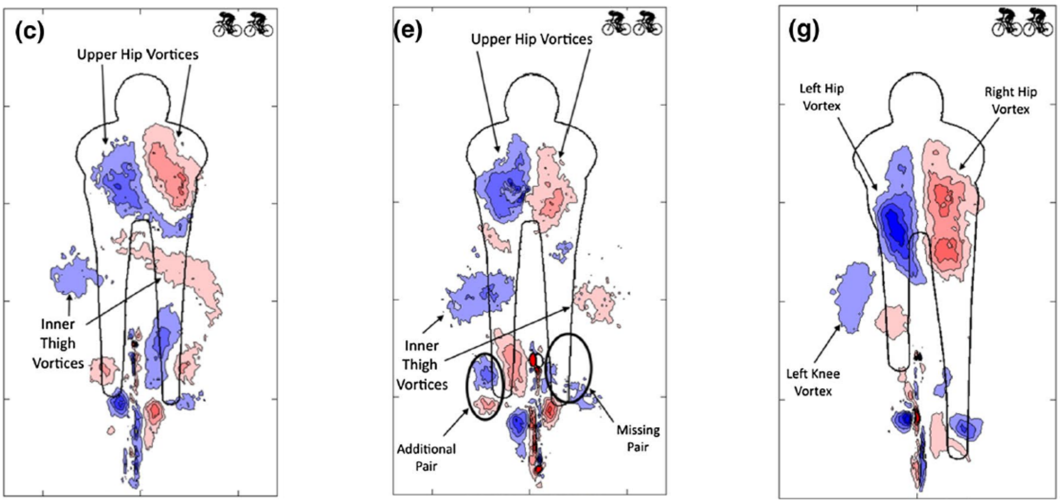

(a) Symmetric - Symmetric (b) Asymmetric - Symmetric (c) Symmetric - Asymmetric

Figure 7.14: Streamwise non-dimensional vorticity in the wake of the trailing cyclist for different configurations of crank angles (Barry et al., 2016b). Blue and red correspond to negative and positive vorticity respectively

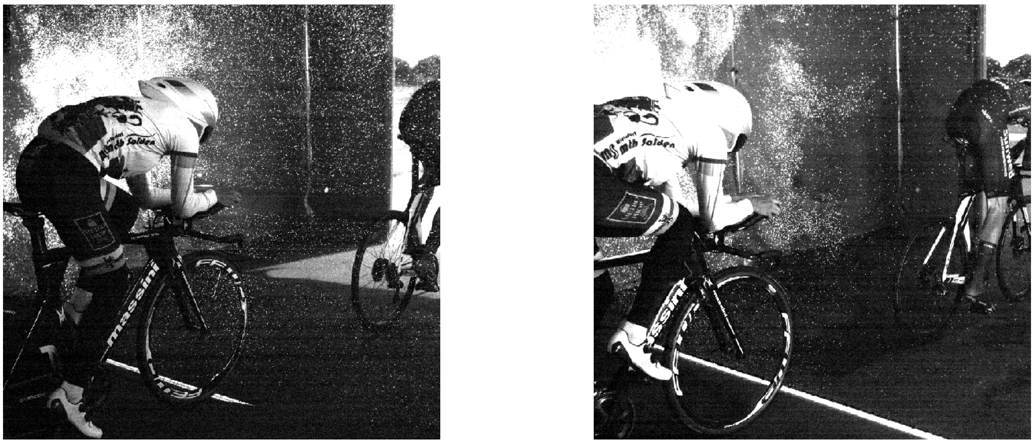

(a) Run #083 (b) Run #041

Figure 7.15: Comparison of instantaneous crank angle of the leading and trailing cyclists

and shorter for Run #083. Similarly, comparison of instantaneous pressure coefficient follows suit with relatively better pressure recovery by Run #041 compared to Run #083. The apparent "amplification" of low pressure regions in the wake of Run #083 is indicative of constructive interference when both the cyclists' crank motion is approximately "in-phase", while "destructive" interference is observed when the crank motion is "out-of-phase" by 180°. Considering that there are no other differences between the data sets, it can be seen that drafting cyclists involves complex interactions between the wake of the leading cyclist and the trailing cyclist, with a correlation between the strength of dominant flow structures and the phase difference in the crank motion of the two cyclists. However, it is important to note that this inference is made from instantaneous flow fields and may not be conclusive evidence. Hence, phase averaged measurements over multiple data sets with the same drafting distance will provide a much clearer picture on whether such an influence exists between phase difference and drag reduction. Moreover, phase averaged measurements should eliminate the outliers and irregularities observed in Figure 7.11.

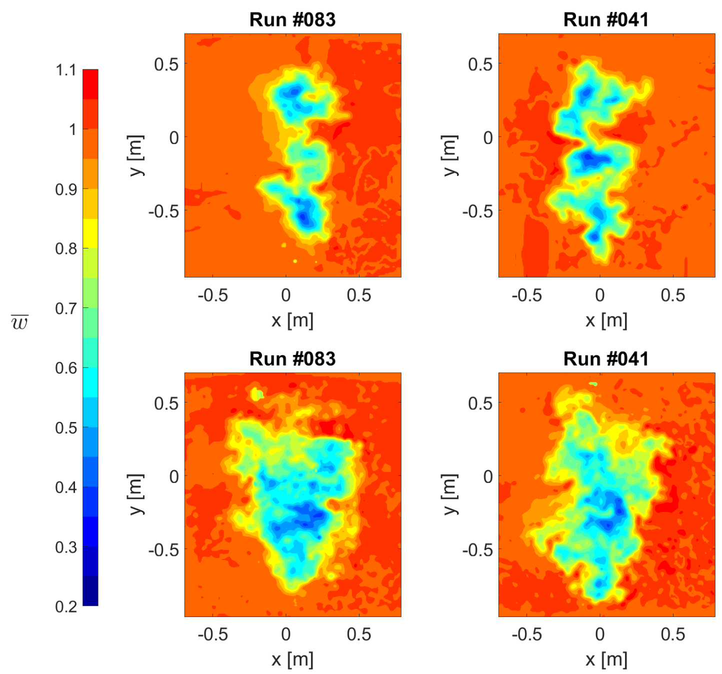

Figure 7.16: Comparison of instantaneous non-dimensional velocity. The first row correspond to the closet velocity field upstream of the trailing cyclist and the second row corresponds to the velocity in the wake of the trailing cyclist at z = 1 m

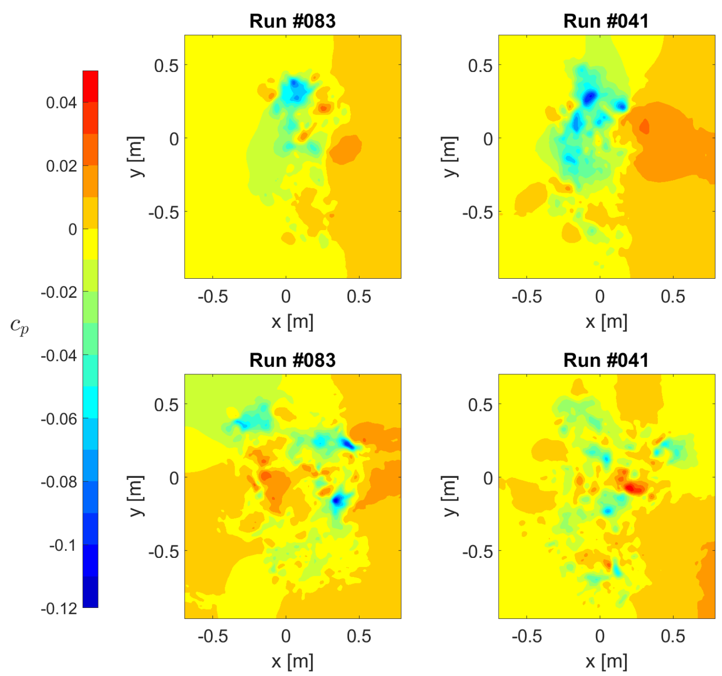

Figure 7.17: Comparison of instantaneous pressure coefficient. The first row correspond to the closet pressure field upstream of the trailing cyclist and the second row corresponds to the pressure field in the wake of the trailing cyclist at z = 1 m

7.3.3. Peloton

Drag area of the group considering both cyclists as a single entity was also evaluated using velocity measurements upstream and downstream of both cyclists. This drag area has a complex relationship with drafting distance and size of the cyclists, which is not so straightforward as the drag of the trailing cyclist (Table 7.3). It is expected that when longitudinal distance is low, the wake of the leading cyclist cannot recover to freestream and subsequently the wake of the trailing cyclist will have a much higher deficit compared to an individual cyclist. Conversely, when longitudinal spacing is high, the flow in-between the cyclist has "time" to recover some momentum and consequently the wake of the trailing cyclist will more closely resemble that of an individual cyclist. However, the size of the leading cyclist wake is much larger at higher longitudinal distances and consequently, the wake size of the trailing cyclist at large spacing will be higher as well.

Table 7.3: Effect of drafting distance on peloton wake

Case	Longitudinal Distance [m]	Lateral Distance [m]	Velocity Deficit	Wake Size
1	0	0	High	Low
2	2	0	Low	High
3	0	0.5	High	High

Lateral distance has a different effect as at high lateral spacing, the size of the peloton wake is much bigger than that of an individual cyclist and the velocity deficit from both the cyclists will contribute to the drag of the group. It can be seen that while the size of the wake is directly proportional to both longitudinal and lateral spacing, and it is expected that the velocity deficit is inversely proportional to longitudinal distance and directly proportional to lateral spacing. As this is from an ideal point of view, it is important to investigate this behaviour in a practical environment. The drag area of the peloton is compared with the sum of individual drag of the two cyclists in the group as follows:

$$\mathrm{R}_{\text{peloton}} = \frac{\left[(C_D A)_{1,\text{ind}} + (C_D A)_{2,\text{ind}}\right] - (C_D A)_{\text{peloton}}}{\left[(C_D A)_{1,\text{ind}} + (C_D A)_{2,\text{ind}}\right]} \times 100 \tag{7.3}$$

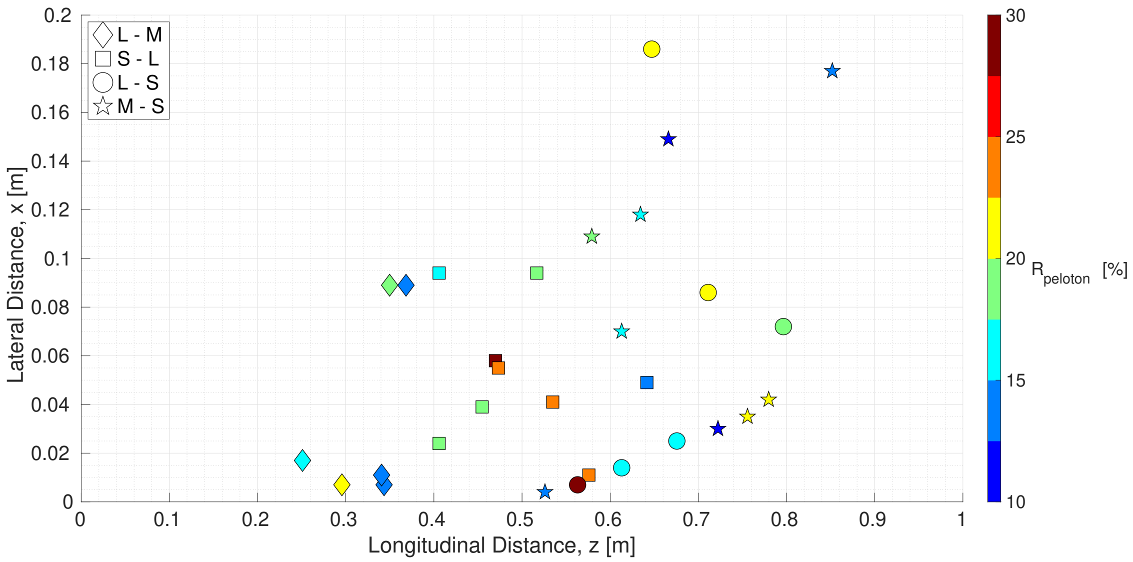

Figure 7.18: Drag reduction of peloton

Where $(C_D A)_{\text{1,ind}}$ and $(C_D A)_{\text{2,ind}}$ corresponds to the individual drag area of the leading and trailing cyclist respectively and $(C_D A)_{\text{peloton}}$ represents the drag area of the two cyclists as a group. This drag reduction was evaluated for all data sets and is shown in Figure 7.18. The “reduction” in peloton drag area was found to be between 10% and 39% with no clear trend between drafting distance and the drag reduction.

A number of anomalies can be observed with overlapping data points corresponding to different drag reductions such as the two S-L data points (shown by square markers) at 0.47 m longitudinally and 0.06 m laterally which have a difference in drag reduction by 6.5%. Investigations of the raw images, velocity and pressure fields revealed that the only difference between the two data sets is the phase difference in crank angle. It can be seen from Figure 7.19 that the phase difference between the leading and trailing cyclist for Run #079 is approximately 90°, while it is close to 180° for Run #081. Comparison of flow fields behind the trailing cyclist shows that the shape of the wake is different for the two cases with Run #081 showing a wider shape (Figure 7.20a) and the size of the wake is higher by 8%. Comparison of pressure coefficient in the wake shows that the low pressure regions are bigger and the peak c_p is lower in Run #081.

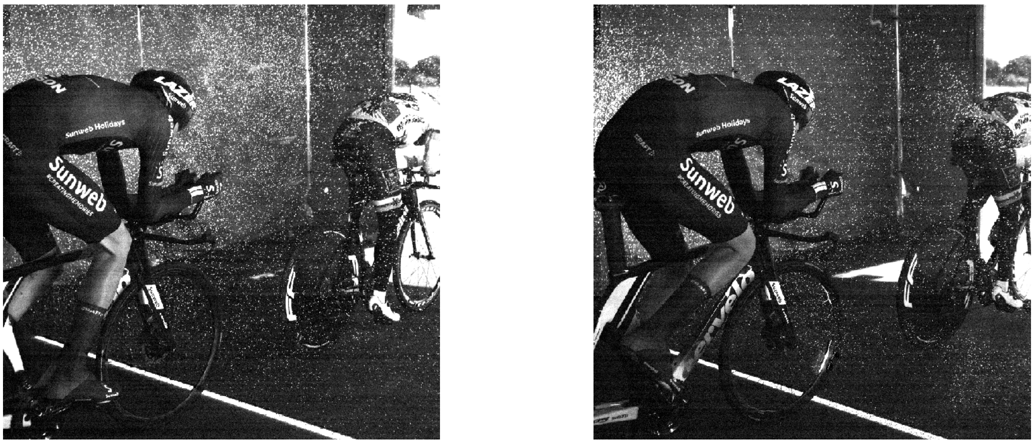

(a) Run #079 (b) Run #081

Figure 7.19: Comparison of instantaneous crank angle of the leading and trailing cyclists

Table 7.4 summarises the comparison between the two data sets with respect to drag area of the peloton and the phase difference between the leading and trailing cyclists. No other difference in terms of head posture and wind variation were found between the two data sets and again, there seems to be a correlation between the phase difference in crank angle and the drag area of the peloton. However, the correlation drawn in the previous section (L-S trailing cyclist drag from Run #041) was between an out-of-phase crank angle and “destructive” interference and recovery of low pressure regions, whereas now the same out-of-phase crank angle is observed with stronger low pressures regions in the wake. It is to be noted that the order of the cyclists is reversed with Run #041 corresponding to L-S configuration and Run #081 corresponding to S-L configuration. Therefore, it can be concluded that further detailed research is required to understand the complex interplay between cyclist wake, phase difference and drag area. Moreover, the non-existence of a trend in the drag reduction of peloton with drafting distance can be attributed to the lack of statistical convergence in drag area which did not account for all possible dynamics of the two cyclists.

Table 7.4: Comparison of drag area and phase difference

Data Set	$(C_D A)_{\text{peloton}}$ **[m^2]**	**R$_{\text{peloton}}$ [%]**	**Phase Difference**
Run #079	0.290	29.1	≈90°
Run #081	0.316	22.6	≈180°

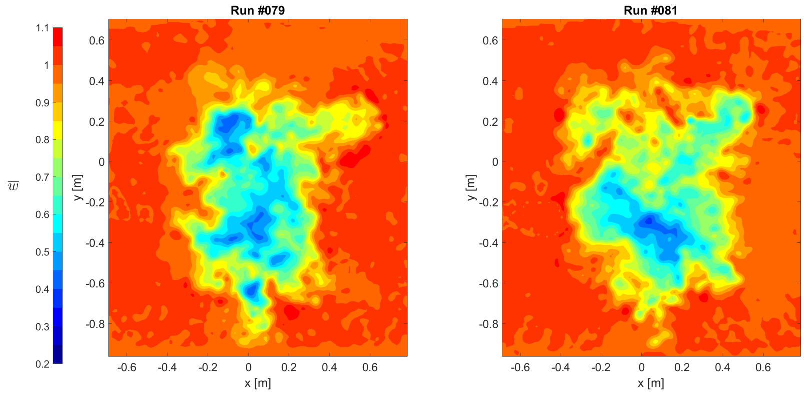

(a) Instantaneous non-dimensional velocity

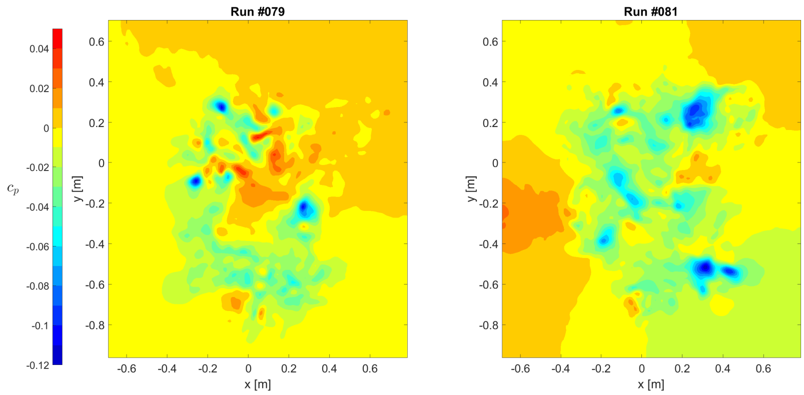

(b) Instantaneous pressure coefficient

Figure 7.20: Comparison of flow fields downstream of trailing cyclist at z = 0.8 m

8
Conclusions and Recommendations

8.1. Conclusions

Large-scale time-resolved stereoscopic PIV was conducted for on-site cyclists individually and in drafting formation using the Ring of Fire system. Helium-Filled Soap Bubbles (HFSB) were used as tracer particles with a maximum acquisition frequency of 1 kHz at cycling speeds of 13.3 m/s. All three components of the velocity field were obtained in a field-of-view of 2 m $\times$ 1.8 m. Three professional cyclists from Team Sunweb were part of the experiments and were classified based on their heights as Small, Medium and Large. Four configurations of two cyclists drafting were studied i.e. Large - Small, Small - Large, Large - Medium and Medium - Small, at the Tom Dumoulin Bike Park, Sittard, Netherlands. Drag area of the cyclists was determined by applying conservation of momentum over the measured control volume.

The experiments posed a feasibility challenge in terms of acquiring measurements in-between two drafting cyclists with an inter-wheel gap of 30 cm. The presence of the second/trailing cyclist would block the optical access of the measurement plane from the acquisition cameras. Based on calculations in MATLAB and experimental simulations, the camera location were chosen based on an optimum between stereo angle, required field of view, overlap between the camera field of views and minimal interference from the trailing cyclist. Using these camera locations, velocity fields were first measured for all three cyclists individually. These measurements agreed well with previous wind tunnel measurements (Crouch et al., 2014; Shah, 2017) as well as previous Ring of Fire experiments (de Martino Norante, 2018; Hirsch, 2018; Spoelstra, 2017). Moreover, the individual results show that the size of the cyclist (specifically height) is a qualitative indicator of relative aerodynamic performance between cyclists, provided cycling equipment and skill are reasonably common between them. It was found that the wake size and drag area are directly proportional to the height of the medium and large cyclist. Particularly, a difference of 3.7% in height between the medium and large cyclist translated to a 11.3% difference in ensemble averaged drag area. However, the small cyclist was found to be an exception to this rule as the cyclist used different cycling equipment (i.e. helmet, skin suit and bicycle) compared to the other two cyclists.

The ensemble averaged drag area for the three cyclists was found to be 0.2046 m^2, 0.1821 m^2 and 0.2038 m^2 for the small, medium and large cyclist respectively. It was found that the trade-off made between accuracy and consistency in terms of the wake contouring procedure resulted in the introduction of a systematic error, reducing the magnitude of drag area for all cyclists compared to wind tunnel measurements and previous Ring of Fire experiments. Statistical uncertainty of the mean drag area was found to be 5.6%, 2.3% and 2.4% for the small, medium and large cyclist respectively. The high statistical spread for the small cyclists was attributed to the combination of fewer usable data sets available for ensemble averaging, variation in wind and changes in helmet posture. The use of data reduction techniques, specifically the contouring of the upstream and wake flow fields was found to improve the uncertainty of the medium and large cyclist relative to previous outdoor Ring of Fire measurements by Spoelstra (2017). Further, it can be concluded that variation in wind between upstream and downstream measurements of the cyclists does affect drag calculations from the Ring of Fire system. Strong head wind increasing in strength from upstream to downstream of the cyclists was found to counteract drag measurements by reducing the size of the wake and overall velocity deficit, which resulted in a decrease of drag area with distance in the wake.

Results from the drafting configurations showed that the cyclists had difficulty in maintaining a constant drafting distance between different passages. On average, the medium cyclist was the closest to the required drafting distance while the small cyclist was more than twice the required distance. Upstream interference of the trailing cyclist resulted in lower velocities in-between the two cyclists compared to an individual wake, similar to the observations made by Barry et al. (2016b). However, pressure fields in-between the cyclists could not be accurately determined as the assumption of quasi-2D flow was found to be invalid and the out-of-plane gradients cannot be neglected in-between the cyclists. This inaccurate pressure reconstruction resulted in erroneous drag area estimations of the leading cyclist i.e. an increase in drag area of the leading cyclist was found while drafting.

The mechanism of drag reduction for the trailing cyclist was due to the in-flow conditions i.e. low velocity and low pressure upstream of the trailing cyclist, which reduced the relative deficit in momentum compared to an individual cyclist. Although this mechanism was reported by scaled water tunnel tests by Barry et al. (2016b) at a Reynolds number one order of magnitude lower than full-scale, the current experiments validate that mechanism for full-scale on-site cyclists. Drag reductions between 27% and 60% were observed for the trailing cyclist with an inverse relationship between drafting distance and drag reduction. Comparison of the influence of longitudinal drafting distance on drag reduction agreed well with the wind tunnel tests of Barry et al. (2014). The effect of lateral distance was found to be approximately three times stronger than longitudinal distance e.g. decrease of 10 cm in longitudinal drafting distance resulted in an increase in drag benefit by 1.3%, while a similar decrease on lateral distance resulted in an increase of 3.9% in drag benefit. Although, drag area of the two cyclist as a group (or peloton) was found to vary with drafting distance, a clear relationship was not found with either distances due to lack of statistical convergence which did not account for all possible dynamics of the two cyclists. Analysis of drafting flow fields indicated towards a possible influence of the phase difference in crank angle between the leading and trailing cyclists and the structure of the wake behind the trailing cyclist. Moreover, a complex interaction between the wake of the leading cyclist and the trailing cyclist was found. However, conclusive evidence was not found to back up this influence.

8.2. Recommendations

A few suggestions for future Ring of Fire measurements based on the shortcomings of the current implementation can be made. Improvements can be made in the experimental setup regarding the faulty door mechanism, low capacity of the air compressor, leakage of soap by the seeding rake, automatic acquisition using photo-detectors and including a transparent panel to prevent the escape of seeding bubbles through the cut-out for the laser sheet.

Further, the large sensor size of the PIV cameras was found to introduce peak locking errors, which can be alleviated using sensors of smaller sizes. Also, as the cameras were placed close to the measurement plane, the bright colours of the cyclist clothing and bicycle was found to introduce unphysical velocity data into the measurements, which can be prevented by using dark colours.

A laser pointer fixed to the trailing cyclist pointing at a distance ahead of the front wheel (i.e. indication of drafting distance) could help the cyclist maintain a constant drafting distance between different passages and prevent large variations in drafting distance.

With regard to data processing techniques, the wake contouring procedure can be further improved to include the part of the wake excluded in the current implementation, with a general and robust procedure. As variations in wind cannot be eliminated completely, a procedure to account for this is suggested where the difference in wind between upstream and wake velocity field is added to the upstream velocity field.

With regard to drafting aerodynamics, the results have shown that there is a complicated interplay between crank angles, drafting distance, cyclist size and equipment. Ensemble averaged and statistically converged measurements from the Ring of Fire will help understand the effect of cyclist size, but phase averaged measurement are required to investigate the effect of crank angle on drag reduction. Keeping track of the crank angles of two cyclists and also making sure the angular velocity of the crank remains constant is a challenging task. Hence, ensemble averaged static tests might be a first step towards understanding the effect of this phase difference in crank angle.

Bibliography

Lara Adrian, Ronald J Adrian, and Jerry Westerweel. *Particle image velocimetry*. Number 30. Cambridge University Press, 2011.

John David Anderson Jr. *Fundamentals of aerodynamics*. Tata McGraw-Hill Education, 2010.

Iliass Azijli, Andrea Sciacchitano, Daniele Ragni, Artur Palha, and Richard P Dwight. A posteriori uncertainty quantification of piv-based pressure data. *Experiments in Fluids*, 57(5):72, 2016.

Nathan Barry, John Sheridan, David Burton, and Nicholas AT Brown. The effect of spatial position on the aerodynamic interactions between cyclists. *Procedia Engineering*, 72:774–779, 2014.

Nathan Barry, David Burton, John Sheridan, Mark Thompson, and Nicholas AT Brown. Aerodynamic drag interactions between cyclists in a team pursuit. *Sports Engineering*, 18(2):93–103, 2015.

Nathan Barry, David Burton, John Sheridan, Mark Thompson, and Nicholas AT Brown. An analysis of the wake of pedalling cyclists in a tandem formation. *Procedia Engineering*, 147:7–12, 2016a.

Nathan Barry, David Burton, John Sheridan, Mark Thompson, and Nicholas AT Brown. Flow field interactions between two tandem cyclists. *Experiments in Fluids*, 57(12):181, 2016b.

Jr DR Bassett, Chester R Kyle, Louis Passfield, Jeffrey P Broker, and Edmund R Burke. Comparing cycling world hour records, 1967-1996: modeling with empirical data. *Medicine and Science in Sports and Exercise*, 31(11):1665–1676, 1999.

Marco Belloli, Stefano Giappino, Fabio Robustelli, and Claudio Somaschini. Drafting effect in cycling: Investigation by wind tunnel tests. *Procedia engineering*, 147:38–43, 2016.

Kim B Blair and Stephanie Sidelko. Aerodynamic performance of cycling time trial helmets (p76). In *The Engineering of Sport 7*, pages 371–377. Springer, 2009.

Bert Blocken, Thijs Defraeye, Erwin Koninckx, Peter Hespel, and Jan Carmeliet. Numerical study of the interference drag of two cyclists. In *Proceedings of the 13th International Conference on Wind Engineering*. Multi-Science Publishing Co Ltd, 2011.

Bert Blocken, Thijs Defraeye, Erwin Koninckx, Jan Carmeliet, and Peter Hespel. Cfd simulations of the aerodynamic drag of two drafting cyclists. *Computers & Fluids*, 71:435–445, 2013.

Bert Blocken, Yasin Toparlar, Thijs van Druenen, and Thomas Andrianne. Aerodynamic drag in cycling team time trials. *Journal of Wind Engineering and Industrial Aerodynamics*, 182:128–145, 2018.

Johannes Bosbach, Matthias Kühn, and Claus Wagner. Large scale particle image velocimetry with helium filled soap bubbles. *Experiments in fluids*, 46(3):539–547, 2009.

JEFFREY P Broker, CHESTER R Kyle, and EDMUND R Burke. Racing cyclist power requirements in the 4000-m individual and team pursuits. *Medicine and Science in Sports and Exercise*, 31(11): 1677–1685, 1999.

Vincent Chabroux, Caroline Barelle, and Daniel Favier. Aerodynamics of time trial bicycle helmets (p226). In *The Engineering of Sport 7*, pages 401–410. Springer, 2008.

Vincent Chabroux, Marcellin Nsi Mba, Patrick Sainton, and Daniel Favier. Wake characteristics of time trial helmets using piv-3c technique. In *15th Int. Symp. on Applications of Laser Techniques to Fluid Mechanics, Lisbon, Portugal*, volume 58, 2010.

Timothy N Crouch, David Burton, Mark C Thompson, Nicholas AT Brown, and John Sheridan. Dynamic leg-motion and its effect on the aerodynamic performance of cyclists. *Journal of Fluids and Structures*, 65:121–137, 2016.

Timothy N Crouch, David Burton, Zach A LaBry, and Kim B Blair. Riding against the wind: a review of competition cycling aerodynamics. *Sports Engineering*, 20(2):81–110, 2017.

Timothy Neville Crouch, D Burton, Nicholas Albert Thomas Brown, Mark Christopher Thompson, and John Sheridan. Flow topology in the wake of a cyclist and its effect on aerodynamic drag. *Journal of Fluid Mechanics*, 748:5–35, 2014.

Luigi de Martino Norante. Advances and assessment of the ring of fire concept for on-site cycling aerodynamics. 2018.

Thijs Defraeye, Bert Blocken, Erwin Koninckx, Peter Hespel, Pieter Verboven, Bart Nicolai, and Jan Carmeliet. Cyclist drag in team pursuit: influence of cyclist sequence, stature, and arm spacing. *Journal of biomechanical engineering*, 136(1):011005, 2014.

PE Di Prampero, G Cortili, P Mognoni, and F Saibene. Equation of motion of a cyclist. *Journal of Applied Physiology*, 47(1):201–206, 1979.

Andy G Edwards and William C Byrnes. Aerodynamic characteristics as determinants of the drafting effect in cycling. *Medicine and science in sports and exercise*, 39(1):170–176, 2007.

David Engler Faleiros, Marthijn Tuinstra, Andrea Sciacchitano, and Fulvio Scarano. Generation and control of helium-filled soap bubbles for piv. *Experiments in Fluids*, 60(3):40, 2019.

Billy Fitton, Oliver Caddy, and Digby Symons. The impact of relative athlete characteristics on the drag reductions caused by drafting when cycling in a velodrome. *Proceedings of the Institution of Mechanical Engineers, Part P: Journal of Sports Engineering and Technology*, 232(1):39–49, 2018.

Giuseppe Gibertini and Donato Grassi. Cycling aerodynamics. In *Sport aerodynamics*, pages 23–47. Springer, 2008.

Matthew Godo, David Corson, and Steve Legensky. An aerodynamic study of bicycle wheel performance using cfd. In *47th AIAA Aerospace Sciences Meeting Including The New Horizons Forum and Aerospace Exposition*, page 322, 2009.

Matthew Godo, David Corson, and Steve Legensky. A comparative aerodynamic study of commercial bicycle wheels using cfd. In *48th AIAA Aerospace Sciences Meeting Including the New Horizons Forum and Aerospace Exposition*, page 1431, 2010.

Frederic Grappe, Robin Candau, Alain Belli, and Jean Denis Rouillon. Aerodynamic drag in field cycling with special reference to the obree's position. *Ergonomics*, 40(12):1299–1311, 1997.

Martin D Griffith, Timothy Crouch, Mark C Thompson, David Burton, John Sheridan, and Nicholas AT Brown. Computational fluid dynamics study of the effect of leg position on cyclist aerodynamic drag. *Journal of Fluids Engineering*, 136(10):101105, 2014.

RD Hill. The design and development of the lotussport pursuit bicycle. *Proceedings of the Institution of Mechanical Engineers, Part D: Journal of Automobile Engineering*, 207(4):285–294, 1993.

Max Hirsch. Accuracy assessment of the ring of fire system for on-site aerodynamic drag measurements. 2018.

A Iniguez-de-la Torre and J Iniguez. Aerodynamics of a cycling team in a time trial: does the cyclist at the front benefit? *European Journal of Physics*, 30(6):1365, 2009.

Constantin Jux. Robotic volumetric particle tracking velocimetry by coaxial imaging and illumination. 2017.

TM Kawamura. Wind drag of bicycles. *Tokyo University, Tokyo*, 1953.

DF Kurtulus, F Scarano, and L David. Unsteady aerodynamic forces estimation on a square cylinder by tr-piv. *Experiments in Fluids*, 42(2):185–196, 2007.

Chester R Kyle. Reduction of wind resistance and power output of racing cyclists and runners travelling in groups. *Ergonomics*, 22(4):387–397, 1979.

Chester R Kyle and Edmund Burke. Improving the racing bicycle. *Mechanical engineering*, 106(9): 34–45, 1984.

CR Kyle. Wind tunnel tests of aero bicycles. *Cycling Science*, 3(3-4):57–61, 1991.

CR Kyle, LW Brownlie, E Harber, R MacDonald, and M Norstrom. The nike swift spin cycling project: reducing the aerodynamic drag of bicycle racing clothing by using zoned fabrics. *The engineering of sport*, 5(1):118–124, 2004.

RA Lukes, SB Chin, and SJ Haake. The understanding and development of cycling aerodynamics. *Sports engineering*, 8(2):59–74, 2005.

James C Martin, Douglas L Milliken, John E Cobb, Kevin L McFadden, and Andrew R Coggan. Validation of a mathematical model for road cycling power. *Journal of applied biomechanics*, 14(3): 276–291, 1998.

Ali Mohebbian and David E Rival. Assessment of the derivative-moment transformation method for unsteady-load estimation. *Experiments in fluids*, 53(2):319–330, 2012.

T Nonweiler. The air resistance of racing cyclists. Technical report, College of Aeronautics Cranfield, 1956.

T Nonweiler. The work production of man-studies on racing cyclists. In *JOURNAL OF PHYSIOLOGY-LONDON*, volume 141, pages P8–P9. CAMBRIDGE UNIV PRESS 40 WEST 20TH STREET, NEW YORK, NY 10011-4211, 1958.

Luca Oggiano, Len Brownlie, Olga Troynikov, Lars Morten Bardal, Camillan Sæter, and Lars Sætran. A review on skin suits and sport garment aerodynamics: guidelines and state of the art. *Procedia Engineering*, 60:91–98, 2013.

Tim Olds. The mathematics of breaking away and chasing in cycling. *European journal of applied physiology and occupational physiology*, 77(6):492–497, 1998.

Lewis Griffith Cresswell Evans Pugh. The relation of oxygen intake and speed in competition cycling and comparative observations on the bicycle ergometer. *The Journal of physiology*, 241(3):795–808, 1974.

Markus Raffel, Christian E Willert, Fulvio Scarano, Christian J Kähler, Steve T Wereley, and Jürgen Kompenhans. *Particle image velocimetry: a practical guide*. Springer, 2018.

David E Rival and Bas Van Oudheusden. Load-estimation techniques for unsteady incompressible flows. *Experiments in Fluids*, 58(3):20, 2017.

Fulvio Scarano, Sina Ghaemi, Giuseppe Carlo Alp Caridi, Johannes Bosbach, Uwe Dierksheide, and Andrea Sciacchitano. On the use of helium-filled soap bubbles for large-scale tomographic piv in wind tunnel experiments. *Experiments in Fluids*, 56(2):42, 2015.

Andrea Sciacchitano, Fulvio Scarano, and Bernhard Wieneke. Multi-frame pyramid correlation for time-resolved piv. *Experiments in fluids*, 53(4):1087–1105, 2012.

Andrea Sciacchitano, Giuseppe Carlo Alp Caridi, and Fulvio Scarano. A quantitative flow visualization technique for on-site sport aerodynamics optimization. *Procedia Engineering*, 112:412–417, 2015.

Yash Shah. Drag analysis of full scale cyclist model using large scale 4d-ptv: An accuracy assessment. 2017.

Alexander Spoelstra. Aerodynamics of transiting objects via large-scale piv-the ring of fire concept. 2017.

W Terra, A Sciacchitano, and F Scarano. Aerodynamic drag of transiting objects by large-scale tomographic-piv. In *Proceedings 18th International Symposium on applications of laser and imaging techniques to fluid dynamics*, pages 1135–1153, 2016a.

W Terra, A Sciacchitano, and F Scarano. Evaluation of aerodynamic drag of a full-scale cyclist model by large-scale tomographic-piv. In *International Workshop on Non-Intrusive Optical Flow Diagnostics*, 2016b.

GS Tew and AT Sayers. Aerodynamics of yawed racing cycle wheels. *Journal of Wind Engineering and Industrial Aerodynamics*, 82(1-3):209–222, 1999.

Cameron Tropea and Alexander L Yarin. *Springer handbook of experimental fluid mechanics*. Springer Science & Business Media, 2007.

BW Van Oudheusden. Piv-based pressure measurement. *Measurement Science and Technology*, 24 (3):032001, 2013.

Jerry Westerweel and Fulvio Scarano. Universal outlier detection for piv data. *Experiments in fluids*, 39(6):1096–1100, 2005.

B Wieneke. Stereo-piv using self-calibration on particle images. *Experiments in fluids*, 39(2):267–280, 2005.

Bernhard Wieneke[1] and Karsten Pfeiffer[1]. Adaptive piv with variable interrogation window size and shape. 2010.

Jie-Zhi Wu, Ze-Liang Pan, and Xi-Yun Lu. Unsteady fluid-dynamic force solely in terms of control-surface integral. *Physics of fluids*, 17(9):098102, 2005.

KBMQ Zaman and AKMF Hussain. Taylor hypothesis and large-scale coherent structures. *Journal of Fluid Mechanics*, 112:379–396, 1981.

MM Zdravkovich. Aerodynamics of bicycle wheel and frame. *Journal of Wind Engineering and Industrial Aerodynamics*, 40(1):55–70, 1992.

MM Zdravkovich, MW Ashcroft, SJ Chisholm, and N Hicks. Effect of cyclist's posture and vicinity of another cyclist on aerodynamic drag. *The engineering of sport*, 1:21–28, 1996.

A

Wake Contouring Procedure

The following MATLAB script was used to identify the central wake region of the cyclist using a cut-off velocity and determine a “logical” matrix with ‘1’s inside the wake and ‘0’s outside the wake. The script uses the MATLAB low-level contour plot computations to determine the contour matrix containing coordinate data for all contours of the specified level. The script then finds the largest contour inside the contour matrix and extracts the coordinate information, which is then used to construct the logical matrix. Further, this script identifies regions outside the wake having high velocity (due to reflections and glares) and replaces those values with a moving median interpolation with a window size of 200. Moving median was chosen as opposed to moving average, nearest neighbour or any polynomial interpolation as it performed relatively better in terms of the interpolated velocity values.

```
function [con_x,con_y,wake_logical,wake_u_filtered,wake_v_filtered,wake_w_filtered] =
    data_cleaning(X_grid,Y_grid,wake_u,wake_v,wake_w,l)
% data_cleaning Identifies central wake region and replaces regions
% outside the cyclist wake having high velocity using moving median interploation.
%
% Inputs: X_grid,Y_grid = X and Y coordinates in meshgrid format
%        wake_u,wake_v,wake_w = wake velocity components
%        l = cut-off velocity or contour level [m/s]
%
% Outputs: con_x,con_y = coordinates of the wake contour
%        wake_logical = matrix containing 1s inside and 0s outside the
%        wake
%        wake_u_filtered,wake_v_filtered,wake_w_filtered = wake velocity
%        components after removing erroneous data points
%
% The function first obtains coordinates of all contours possible for given
% cut-off velocity/contour level and then selects the largest ”island”. A
% matrix is constructed with all coordinates inside the contour as ’1’s and
% outside as ’0’s.
%
% Next, the functions identifies all regions outside the wake having high
% velocites and replaces them with a moving median interpolation.

% draw contour of specified velocity
C = contourc(X_grid(1,:),Y_grid(:,1),wake_w,[l l]);

% find largest island
[A,I] = max(C,[],2);

% x-coordinates of contour
con_x = C(1,I(2)+1:I(2)+A(2));

% y-coordinate of contour
con_y = C(2,I(2)+1:I(2)+A(2));

% find points inside contour (’in’ is a logical matrix i.e. 1 and 0)
[wake_logical,~] = inpolygon(X_grid,Y_grid,con_x,con_y);

```

```
wake_u(wake_w.*~wake_logical < 1) = NaN;
wake_v(wake_w.*~wake_logical < 1) = NaN;
wake_w(wake_w.*~wake_logical < 1) = NaN;

% Interpolate regions of NaN by a moving median over a window of size 200.
wake_u_filtered = fillmissing(wake_u,'movmedian',200);
wake_v_filtered = fillmissing(wake_v,'movmedian',200);
wake_w_filtered = fillmissing(wake_w,'movmedian',200);

end
```

B

Algorithm of Mass Conservation and Contour Projection

The algorithm used to determine the appropriate contour for the upstream velocity field is discussed here. The upstream contour is a scaled down version of the first wake velocity contour. The amount of scaling is dependent on the residual in mass flow rate between the upstream and downstream velocity fields. This problem is solved as a root-finding exercise of the form $R = f(c)$, where R is the residual is mass flow rate and c is the scaling factor. An appropriate scaling factor has to be determined such that the residual is zero. The root is found numerical using the iterative bisection method. This algorithm is written in MATLAB and the inputs to are as follows:

- i_{max}: Maximum number of iterations, chosen as 25. When the number of iterations exceed the specified maximum, the algorithm finds the residual that is closest to zero and the corresponding scaling factor is chosen as the root.
- tol: Tolerance for the residual in mass flow rate between upstream and downstream planes, chosen as 10^{-3}. When the magnitude of the residual falls below the specified tolerance, the iterations stop and the corresponding scaling factor is chosen as the root.
- $[a\ b]$: Interval inside which the appropriate scaling factor (c) exists, such that $R(c) < tol$. These "limits" are chosen by trial and error as [0.1 2]. These limits were found to work for all data sets and all configurations, individual and drafting.

Convergence of the algorithm is monitored by two parameters i.e. i_{max} and tol. On average, the average number of iterations taken to achieve convergence was found to be less than 15 and the average residual in mass flow rate was found to be of the order of 10^{-4}. Technically, the algorithm requires other inputs to compute the residual such as the contour matrix, mesh grid, wake velocity field, upstream velocity field, cyclist velocity, etc. This residual is computed according to Equation 5.5. The flow chart of the algorithm is shown in Figure B.1 .

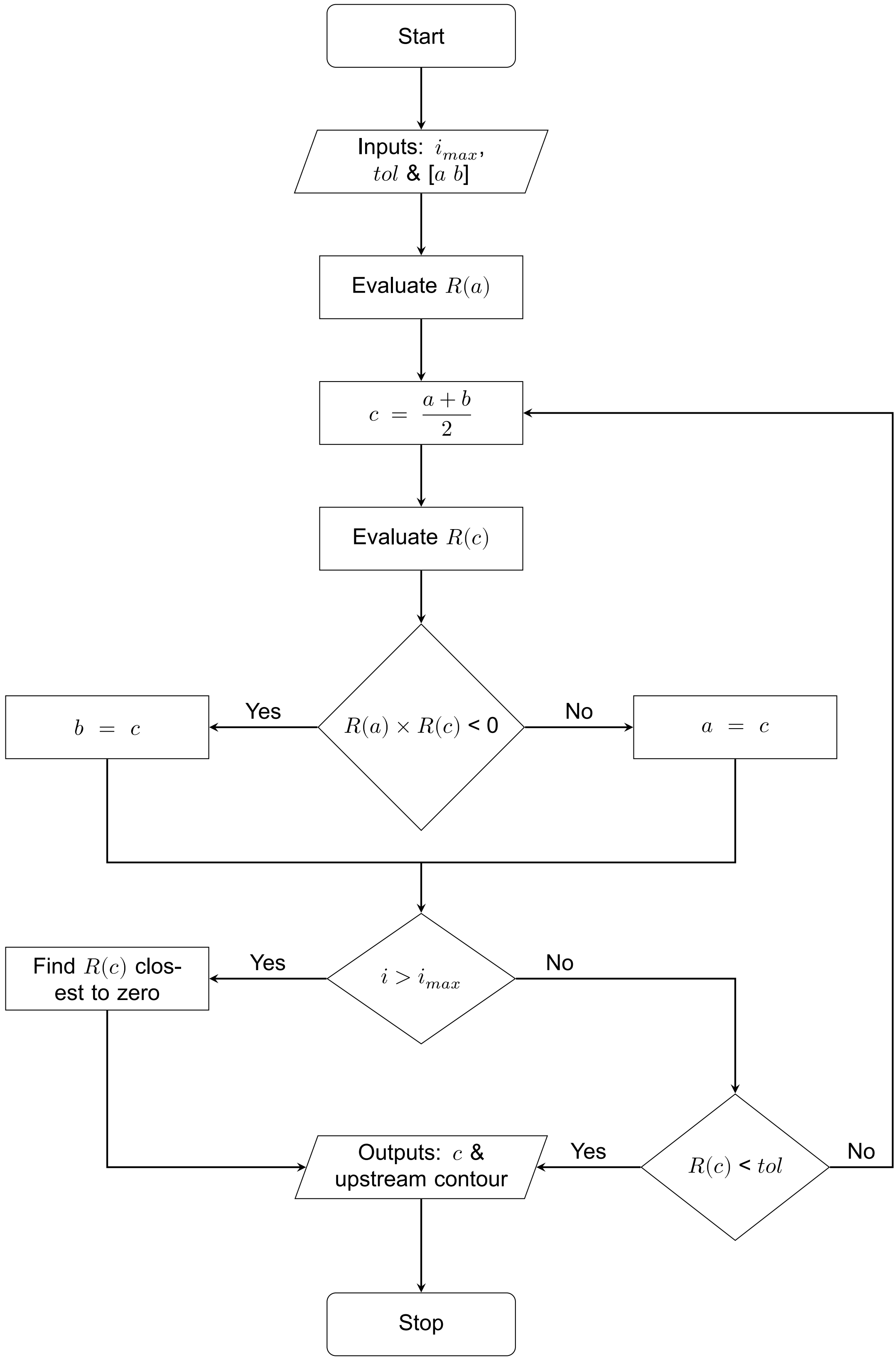

Figure B.1: Flow chart of the implemented root-finding bisection algorithm

C
Frontal Area

The frontal area of the cyclists was measured in order to determine the drag coefficient of the cyclists. The determination of frontal area will provide additional diagnostic information on whether changes in drag area between cyclists is due to difference in drag coefficient or difference in frontal area (or size of the cyclists). Videos of the cyclists passing next to the calibration plate was taken for multiple cyclist passages. The video was taken such that the optical axis of the camera was approximately aligned to the cyclist direction. Key-frames were extracted from the video to select the image where the cyclist is next to the calibration plate (Figure C.1). An Image manipulation software (GIMP) was used to draw a contour of the cyclist and the number of pixels inside the contour was determined. As the dimensions of the calibration plate were known, the image dimensions of the plate can be used to determine optical magnification. This optical dimensions was then used to calculate the frontal area of the cyclist.

Figure C.1: Determination of frontal area of cyclist

This procedure was repeated for multiple cyclist passages next to the calibration plate. However, it was found that most of the videos could not used to determine frontal area as in some cases the cyclist was not aligned along the axis of the camera (Figure C.2a), while in other cases, the video was too short in length, resulting in the cyclist not passing next to the calibration plate in the last key-frame of the video (Figure C.2b). Although frontal area was measured in the latter case, this value was smaller compared to other measurements.

Nevertheless, the measured frontal area for the three cyclists is shown in Table C.1. N denotes the number of data points available for averaging the measured frontal area. It can be seen that the measured frontal area follows the opposite trend compared to the classification of the cyclist based on their height, with the small cyclist having the largest front area and the large cyclist having the smallest frontal area. It is important to note that the procedure to determine frontal area introduces subjectivity in terms of determination of the contour of the cyclist and this can eliminated by averaging the frontal

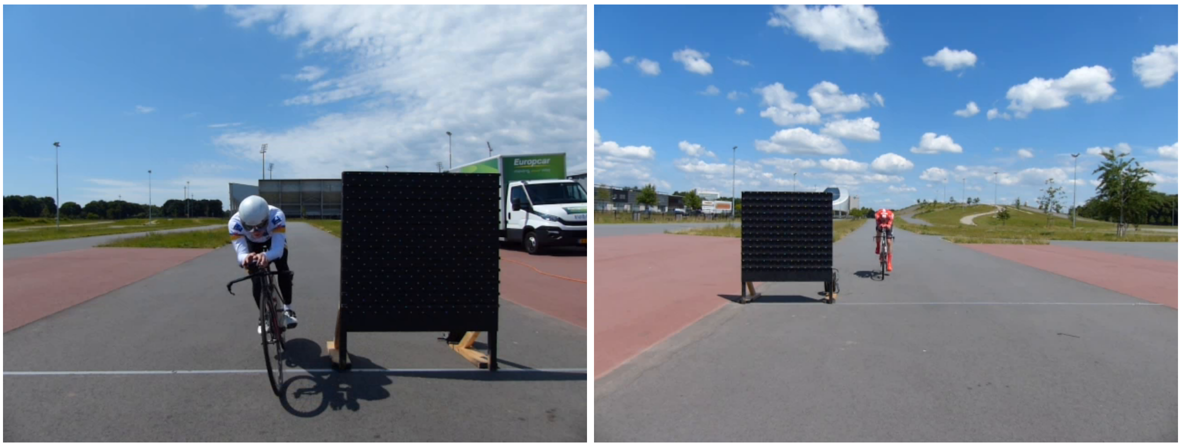

(a) Cyclist not aligned with camera axis (b) Cyclist not next to the calibration plate

Figure C.2: Errors in frontal area measurement

area over multiple data points. Given that these frontal area measurements are based on single data points (for the small and large cyclist), these values cannot be used as an accurate measure of the frontal area and therefore, was not used in the current thesis.

Table C.1: Frontal area measurements of the three cyclists

Cyclist	**Frontal Area [m^2]**	**N**
Small	0.360	1
Medium	0.337	3
Large	0.316	1

D

Sources of Error

A fair comparison between different instantaneous data sets requires that all parameters of testing are common. Especially to understand the anomalies in drag reduction of trailing cyclist and the peloton, the sources of error have to be determined. Therefore, Table D.1 was made to keep track of differences between data sets in terms of physical features such as cyclist postures and numerical parameters such as cut-off velocity and pressure reconstruction. However, it is to be noted that quantification and propagation of these errors into measured quantities such as drag area and drag reduction is not performed.

Table D.1: Sources of error

Raw images	**Cyclist**	**Raw velocity fields**	**Drag analysis**
Seeding	Posture	Reflections	Cut-off velocity
Illumination	Velocity	Optical blockage	Wake contour
Image pre-processing	Drafting distance	Wind variation	Filtering procedure
	Crank angle		Upstream contour
			Pressure reconstruction
			Momentum deficit
			Pressure deficit
			Drag area averaging